Global Hybrid Simulation of Kinetic Alfvén Waves Associated with Magnetotail Reconnection and Fast Flows

by

Lei Cheng

A dissertation submitted to the Graduate Faculty of
Auburn University
in partial fulfillment of the
requirements for the Degree of
Doctor of Philosophy

Auburn, Alabama
May 2, 2020

Keywords: KAWs, magnetotail reconnection, fast flows

Approved by

Yu Lin, Chair, Professor of Department of Physics
J. D. Perez, Professor of Department of Physics
David Maurer, Professor of Department of Physics
Luca Guazzotto, Associate Professor of Department of Physics
Junshan Lin, Associate Professor of Department of Mathematics and Statistics

Abstract

It is believed Alfvén waves, and particularly kinetic Alfvén waves (KAWs), play an important role in the coupling between the solar wind and the magnetosphere. Although KAWs have been observed in the magnetotail and ionosphere, their generation mechanisms and global transport properties are still unclear. A global process with interconnection among various regions of the magnetosphere, driven self-consistently by the solar wind, is poorly understood because of the limitations of local codes. We use the 3-D global hybrid code, i.e., Auburn Global Hybrid Code in 3-D (ANGIE3D) to reveal the global structure of KAWs from the magnetotail to the ionosphere for the first time.

Our results show that KAWs are generated in magnetic reconnection in the plasma sheet, located around fast flows, and carrying transverse electromagnetic perturbations, parallel Poynting fluxes, parallel currents, and parallel electric field. Overall, shear Alfvénic turbulent spectrum is found in the plasma sheet. The KAWs are shear Alfvén waves possessing short perpendicular wavelength with $k_\perp \rho_i \sim 1$, where $k_\perp$ is the perpendicular wave number and ρ_i the ion Larmor radius. The KAWs are identified by their dispersion relation and polarizations. The structures of these KAWs embedded in the plasma sheet are also revealed by placing a virtual satellite in the tail. In order to understand whether the Poynting fluxes carried by the shear Alfvén waves/KAWs in the plasma sheet can be carried directly along field lines to the ionosphere, we have tracked the wave propagation from the plasma sheet to the ionosphere. It is found that in front of the flow braking region, the structure and strength of the shear Alfvén waves are significantly altered due to interaction with the dipole-like field, mainly by the flow shear associated with the azimuthal convection. Also in front of the dipole-like field region, ion kinetic effects (Hall effects) lead to the generation of additional pairs of KAWs. As such, the generation and transport of the shear Alfvén waves/KAWs to the ionosphere are illustrated for the first time in a comprehensive manner on the global scale.

We also make a comparison between our simulation results with the observation results from THEMIS and DMSP. The wave structure during a substorm are investigated in the simulation. Our hybrid simulation results are consistent with THEMIS P3(D) observations. Kinetic Alfvén waves are observed by THEMIS in the plasma sheet, and the corresponding shear Alfvénic signatures are observed by DMSP. The shear Alfvén events observed by DMSP are found to be mapped to various locations in the plasma sheet from $x = -25\ R_E$ (consistent with magnetic reconnection region in our simulation) to $x = -9\ R_E$ (consistent with the flow-braking region in our simulation).

Besides, the ions are seen accelerated and trapped by KAWs associated with magnetic reconnection and flow braking. Ions are also accelerated when crossing the low-latitude boundary layer. Ion velocity distributions in front of the dipolarization are investigated. The parallel ion heating is likely as a result of the parallel electric field carried by KAWs and reflected KAWs at the inner boundary. The two beams merge due to the tailward ion beam encounters the dipolarization and is reflected earthward by the earthward propagating dipolarization. Eventually, parallel energy are transfered to perpendicular energy at the flow-braking region. ons acceleration are discussed.

Acknowledgments

The completion of this dissertation marks an end to my graduate studies in Auburn University. During the past years, I have received much help from many people.

Firstly, my deepest appreciation goes first and foremost to my supervisor Dr. Yu Lin. She introduced me into the area of space plasma. From her, I learned how to do research, how to make presentations and how to write a paper. She has provided me with valuable advice in choosing the thesis topic and organizing the content. Her guidance and help pave the way for my graduation.

Secondly, I want to thank other teachers and friends for helping me in graduate study and daily life. I would like to thank Dr. Wang for teaching me how to use hybrid code. I would like to thank Dr. Perez for discussions and paper modification. I thank Dewang Song and Dr. Zhenyu Wang for their help in graduate study and daily life after I arrived Auburn for the first time. I thank my friend, Lei Chen, and his wife, Xian Zhao for helping me in daily life. I thank Dr. Feng Shi and Dr. Zhifang Guo in helpful discussions. I also thank Dr. Ye Li and his wife, Qi Cui for answering my questions.

Besides, Thanks in particular to Dr. Perez, Dr. Maurer, Dr. Guazzotto and Dr. Junshan Lin for taking the time to review my thesis.

Last but not least, I would like to thank my wife and my parents who are always there to give me constant encouragement and support whenever I need. Their love is my perpetual treasure.

There are special thanks for Auburn. Here, I met my wife and fell in love.

Table of Contents

List of Figures

List of Tables

List of Abbreviations

2-D Two-Dimensional

3-D Three-Dimensional

AE Auroral Electrojet

AMPTE Active Magnetospheric Particle Tracer Explorers

ANGIE3D Auburn Global Hybrid Code in 3-D

BBFs Bursty Bulk Flows

DFs Dipolarization Fronts

DMSP Defense Meteorological Satellite Program

Dst Disturbance storm time

FACs Field-Aligned Currents

FFT Fast Fourier Transform

FTEs Flux Transfer Events

GSM Geocentric Solar Magnetospheric

HT de Hoffmann-Teller

IAW Inertial Alfvén Wave

IMF Interplanetary Magnetic Field

IRM Ion Release Module

ISEE International Sun-Earth Explorer

KAW Kinetic Alfvén Wave

MHD MagnetoHydroDynamics

MLAT Geomagnetic Latitude

MMS Magnetospheric Multiscale

PIC Particle-In-Cell

PSBL Plasma Sheet Boundary Layer

SCW Substorm Current Wedge

SYM/H Symmetric H-component

THEMIS Time History of Events and Macroscale Interactions During Substorms

Chapter 1

Introduction

The topic of this thesis is to study the generation, dynamics, and global structure of kinetic Alfvén waves (KAWs) from the magnetotail to the ionosphere associated with magnetic reconnection and fast flows. The method we use is Auburn Global Hybrid Code in 3-D (ANGIE3D). The purpose of this chapter is to give readers essential background knowledge. We will review the magnetosphere and magnetic reconnection in Section 1.1 and Section 1.2, respectively. The substorm and fast flows are introduced in Section 1.3. The last part of this chapter gives the introduction to KAWs in Section 1.4 followed by the motivation in Section 1.5.

1.1 An Introduction to the Earth's Magnetosphere

A magnetosphere is an area of space surrounding a planet dominated by the planet's magnetic field. The shape of the Earth's magnetosphere is a nose-like region as shown in Figure 1.1. The solar wind is a stream of charged particles consisting of protons, electrons and alpha particles released from the Sun. Interplanetary magnetic field (IMF) is a part of the Sun's magnetic field embedded in the solar wind. The IMF travels outward in a spiral pattern due to the rotation of the sun (see Figure 1.2) [99]. The x and y component of IMF are oriented parallel to the ecliptic. The third component (B_z) is perpendicular to the ecliptic and is created by waves and other disturbances in the solar wind.

Since the solar wind is both supersonic and super-Alfvénic, the bow shock forms at around a geocentric distance of $13R_E$ when it encounters the obstacle of the Earth's magnetic field to its flow. The magnetosheath is a zone formed by the shocked solar wind with a width of $2 - 4R_E$. Particles escaping from the magnetosphere are also found in this region. Within the magnetosheath, the magnetic field is turbulent and distorted. The particle density and magnetic

field strength vary much at different locations in the magnetosheath. The density typically decreases from the bow shock to the magnetopause. The magnetopause is a sharp boundary between a planet's magnetic field and solar wind. The magnetopause is located where the pressure of the dynamic planetary magnetic field and the dynamic pressure of the solar wind come into balance.

The Earth's magnetosphere is formed by the interaction of solar wind and the Earth's magnetic field. The dayside magnetosphere is compressed and extends out to a distance of approximately 10 Earth radii (R_E) while the nightside magnetosphere (magnetotail) is stretched up to at least a few hundreds of the Earth's radii.

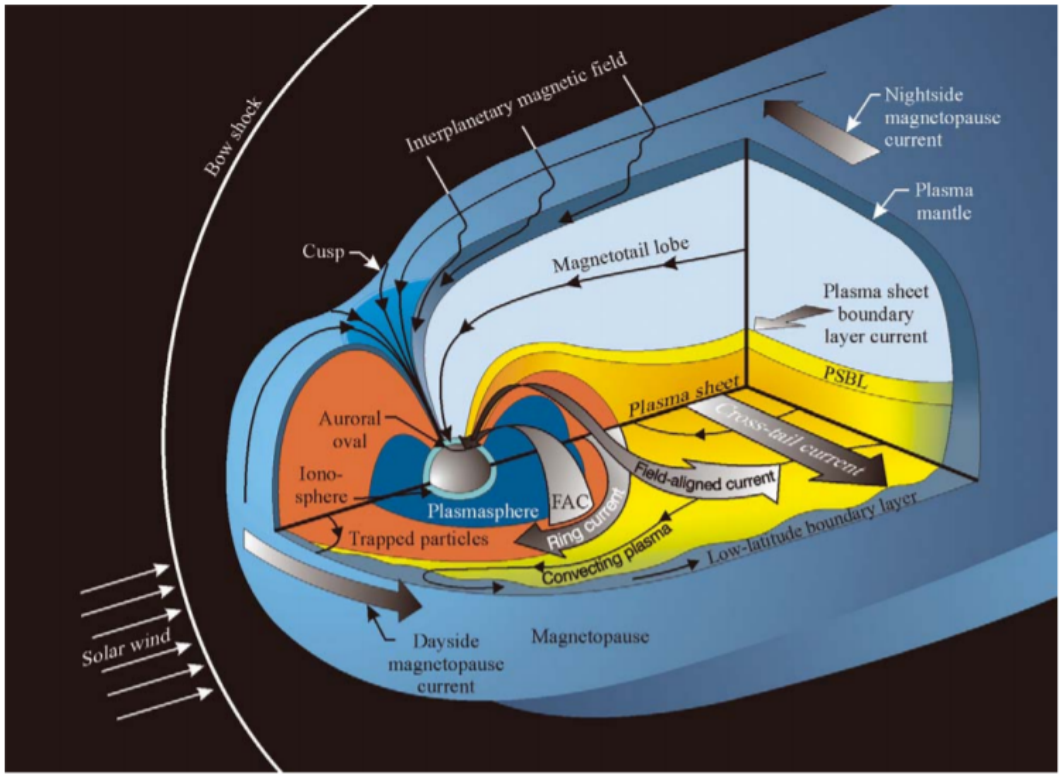

Figure 1.1: Schematic illustration of Earths magnetosphere, illustrating major distinct regions and electric current systems. Adapted from Pollock et al. [107].

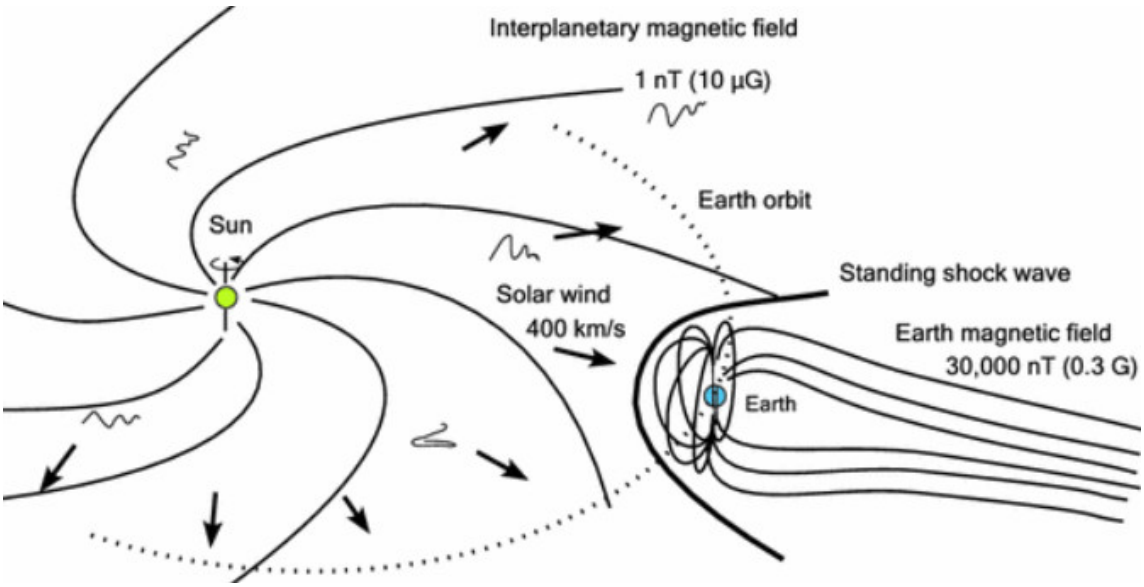

Figure 1.2: Schematic illustration of IMF. Adapted from Narita et al. [99].

1.1.1 Magnetotail

Magnetotail is the elongated region of the magnetosphere of a planet that extends in the direction away from the sun. It contains two lobes, referred to as the northern and southern tail lobes, plasma sheet boundary layer (PSBL) and plasma sheet. Particle number density (below a few hundreds of eV) and temperature (below $0.1/\mathrm{cm}^3$) are very low in lobes. Magnetic field lines in the northern tail lobe point towards the planet while those in the southern tail lobe point anti-sunward. The two lobes are separated by plasma sheet with a typical thickness of $3-7R_E$. The boundary between the plasma sheet and the lobes are called PSBL. Since magnetic field has opposite direction on the two side of the center of plasma sheet, plasma sheet can also be considered as current sheet(cross-tail current) [100]. Opposite to those in lobes, magnetic field is weaker while particle number density and temperature are higher in the plasma sheet. Typically, the particle number density is $0.1-1/\mathrm{cm}^3$ and temperature is a few keV. Plasma sheet and PSBL is the region where electromagnetic energy are stored.

1.1.2 Inner Magnetosphere

The inner magnetosphere is characterized by the dominance of dipolar Earth's magnetic field and closed drift paths of charged particles. The trapped particles result in the formation of

unique particle environment, namely the plasmasphere, the ring current, and the radiation belts. The plasmasphere is a torus of cold ($\sim 1eV$), dense ($10 - 10^3/\mathrm{cm}^3$) plasma trapped on field lines in the co-rotation region of the inner magnetosphere. Radiation belts comprise energetic charged particles trapped by the planets magnetic field (from keV to MeV). The three regions are overlapped. The incoming energy from the outer magnetosphere and the ionosphere in the forms of particles and electromagnetic fields makes the inner magnetosphere very dynamic.

As plasma convects from magnetotail towards Earth, gradient drift causes electrons to drift eastward while protons are drifted westward. The result is the formation of ring current. The ring current is one of the major current systems in the Earth's magnetosphere. It circles the Earth clockwise around the Earth (when viewed from the north) in the equatorial plane and is generated by the longitudinal drift of energetic ($10-200keV$) charged particles trapped on field lines between $L \sim 2$ and 7. The L value is the radial location, in R_E, of field line's intersection with magnetic equator. During a geomagnetic storm, the number of particles in the ring current and the value of current will increase dramatically. Thus, Dst (disturbance storm time) index , a measure of magnetic field induced at equator of Earth by ring current, is used to assess the severity of magnetic storms. For example, the storm reached maximum intensity and the Dst index had dropped to $-312nT$ on February 9 in Figure 1.3 [52].

1.1.3 Current System in the Magnetosphere

The transport of charge, mass, momentum, and energy is highly related to the current system in the magnetosphere. The study of current system is vital to understand the geomagnetic activity. The current system in the magnetosphere is very complex because of time-varying nature of geospaces. Currents are associated with the magnetic field topology through Amperes law. Earth's magnetosphere contains many regions with perturbed magnetic field as described in the introduction to the magnetosphere. Therefore, a lot of current system is generated in the magnetosphere. Figure 1.1 shows the main current system in the magnetosphere [107]. The typical current system includes Chapman-Ferraro magnetopause currents, cross-tail currents, ring currents and field-aligned currents (FAC).

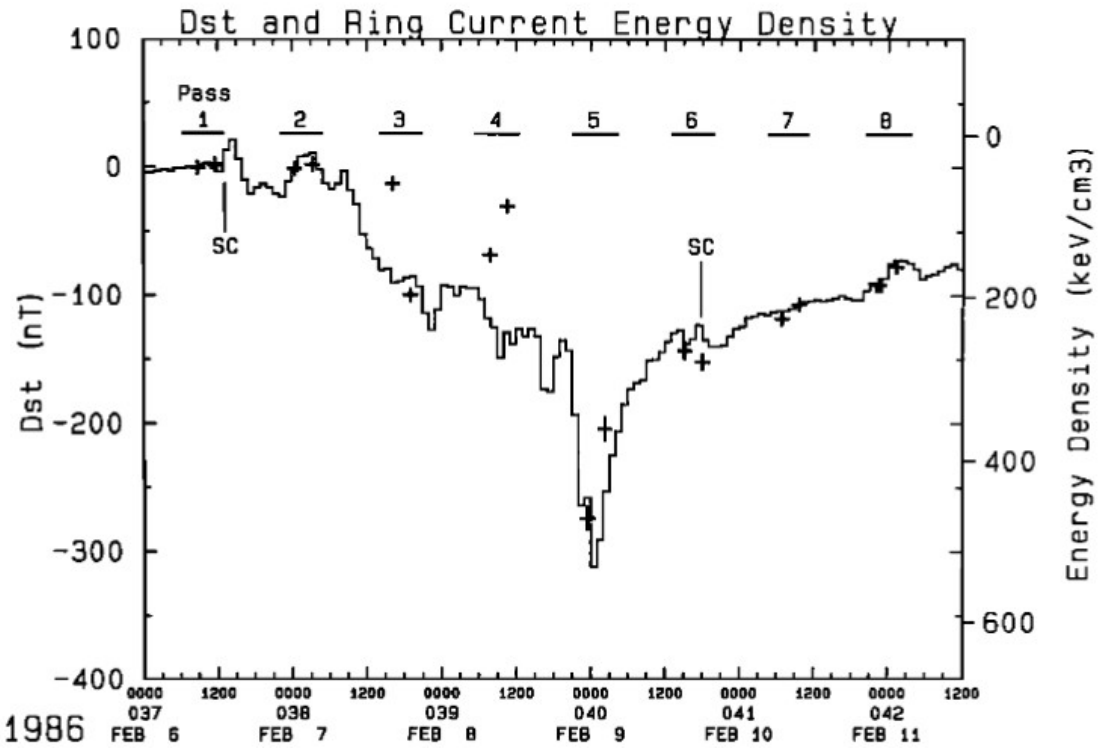

Figure 1.3: Preliminary hourly Dst value during the great geomagnetic storm of February 1986. Adopted from Hamilton et al. [52].

The Chapman-Ferraro magnetopause currents with a thickness of several hundred kilometers flow around the cusps (from dawn to dusk across the equatorial magnetopause and from dusk to dawn across the high-latitude magnetopause tailward of the cusp) as illustrated in Figure 1.4 [42]. The cause of the magnetopause currents is explained by the trajectories of magnetosheath ions and electrons and their interaction with the geomagnetic field [70]. The particles come back to the magnetosheath after only a half of gyration since the dipole magnetic field has a larger strength. Considering the different dirction of the gyration of ions and electrons, the current is formed in the magnetopause.

Cross-tail currents are formed because of the opposite direction of the magnetic fields in the two lobes. The currents are from dawn to dusk and are closed via the magnetopause currents. Magnetic reconnection or instabilities in the cross-tail current lead to the substorm.

The ions drift westward while electrons drift eastward in the inner magnetosphere. Thus, ring currents are formed flowing clockwise from the view of the north hemisphere.

Field-line currents, also called Birkeland currents, are divided into two parts i.e. Region 1 currents and Region 2 currents. Both of them are connected to the ionosphere and ultimately

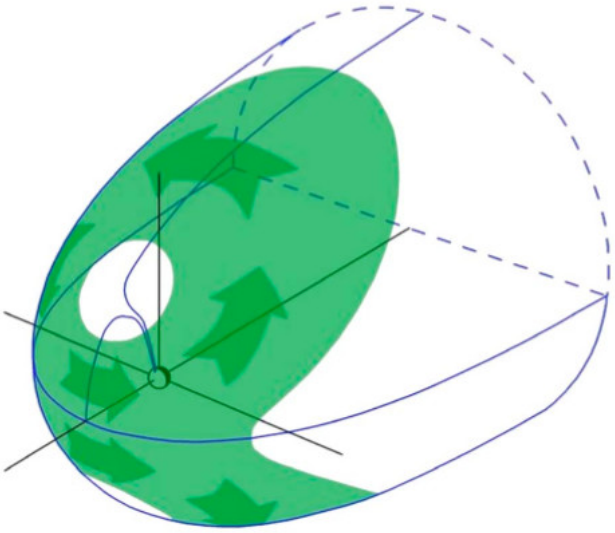

Figure 1.4: Schematic of The Chapman-Ferraro magnetopause currents. Adapted from Ganushkina et al. [42].

driven by reconnection on the dayside and the nightside. That's why they plan an important role in the coupling of the ionosphere and the magnetosphere. Figure 1.5 shows the two currents [28]. Region 1 currents and magnetopause and magnetotail currents form a closure while Region 2 currents and the partial ring current on the nightside of the Earth in the inner magnetosphere form another closure [27, 25, 28]. Region 1 currents flow in the ionosphere on the dawn side and flow out of the ionosphere on the dusk side as opposed to Region 2 current. The two currents are connected with each other via ionospheric Pedersen currents. The region 1 currents are thought to ow in part within the boundary between the open and closed field lines [25].

The currents shown above are the typical currents in the magnetosphere. Some different current system, for example, banana current [43], is also found in the magnetosphere.

1.2 An Introduction to Magnetic Reconnection

Magnetic reconnection is a fundamental mechanism of abrupt energy conversion from magnetic energy to plasma thermal and kinetic energy in space plasmas, and it is believed to be responsible for solar flare and brilliant aurora. Magnetic reconnection is observed at the magnetopause, magnetosheath and magnetotail in the magnetosphere. The idea of magnetic reconnection first arose in an attempt to understand the solar corona heating and the origin of the

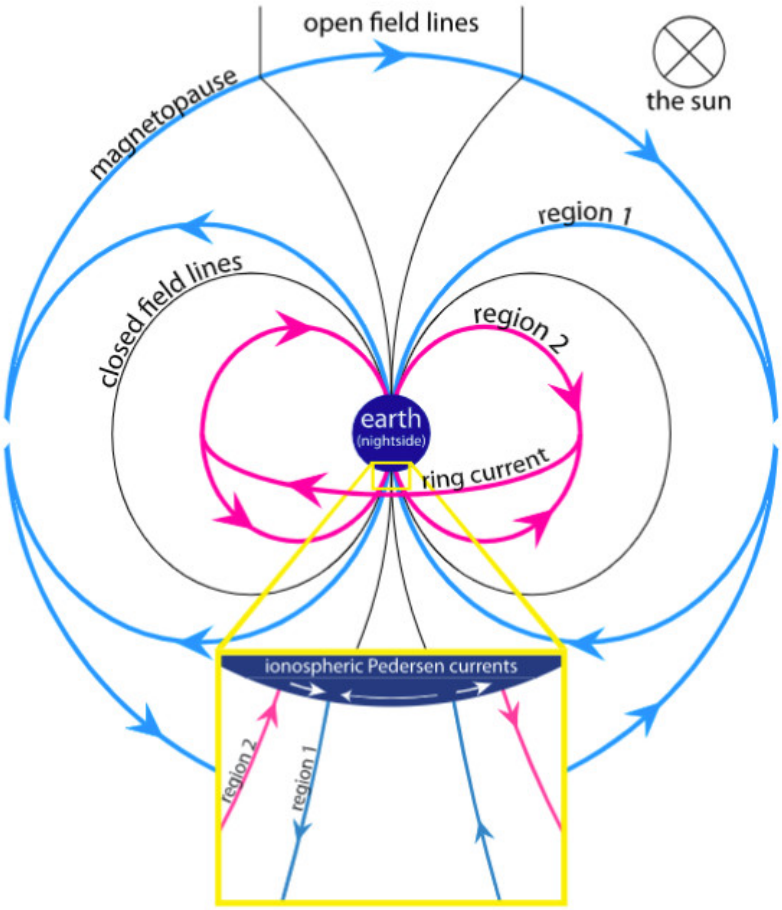

Figure 1.5: Schematic of field-line currents. Adapted from Coxon et al. [28].

enormous energy observed in solar flares [46]. One of the first applications of reconnection is in geomagnetic and magnetospheric plasma processes proposed by Dungey [38]. In plasma physics, charged particles are confined to circular orbits around magnetic field lines known as magnetic field lines ”frozen-in” to an infinitely conductive plasma. It is true in most cases. One result of this ”frozen-in” theory is that solar plasma are not allowed to penetrate the magnetosphere. However, at dayside magnetopause, the solar plasma do penetrate the magnetosphere based on observations. The answer to solve the problem is the magnetic reconnection which refers to the breaking and reconnecting of oppositely directed magnetic field lines in a plasma. In the process, a strong current is developed in the presence of which even a vanishingly small amount of resistivity in a small volume can become important, allowing plasma diffusion and, thus, magnetic reconnection to occur. In the view of energy, magnetic field energy is converted

to plasma thermal and kinetic energy (ions and electrons are heated and accelerated) [104, 58]. Three kinds of typical magnetic reconnection model are introduced below.

1.2.1 Slow Reconnection: Sweet–Parker Model

The first theoretical framework of magnetic reconnection, established by Peter Sweet and Eugene Parker [104] in 1956, is based on MHD theory. The Sweet–Parker model [146] is the simplest description of resistive magnetic reconnection: two oppositely directed magnetic fields B_{in} in a plasma with uniform density ρ and resistivity η in an inflow velocity V_{in} are carried toward the neutral line of the elongated current sheet of half-length L and half–width δ as sketched in Figure 1.6; The system is assumed to be in a steady state. The outflow velocity V_{out} is determined by the conservation of the mass:

$$V_{in}L = V_A\delta. \tag{1.1}$$

Conservation of energy (magnetic energy flux in equals kinetic energy flux out) gives

$$LV_{in}\left(\frac{B_{in}^2}{8\pi}\right) \sim \delta V_{out}\left(\frac{\rho V_{out}^2}{2}\right). \tag{1.2}$$

The outflow speed is the the upstream Alfvén speed given in Gaussian units by $V_{out} \sim V_A \equiv B_{in}/\sqrt{4\pi\rho}$ from Equation (1.1) and Equation (1.2). The electric field is given by the Ohm's law:

$$\mathbf{E} = -\frac{\mathbf{V}\times\mathbf{B}}{c} + \eta\mathbf{J}. \tag{1.3}$$

The resistive electric field is important only inside current sheet. Using the Ampere's law, the dimensionless reconnection rate finally is given by as

$$\frac{V_{in}}{V_A} \sim \frac{1}{S^{1/2}}, \tag{1.4}$$

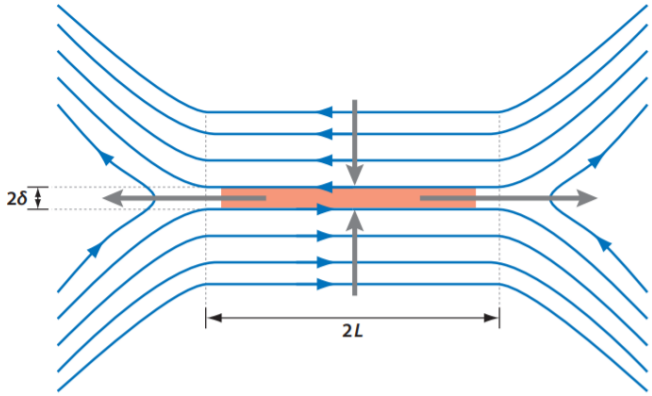

Figure 1.6: Sketch of magnetic field geometry in Sweet-Parker reconnection. Oppositely directed magnetic fields are brought together over a length $2L$ and reconnect in a diffusion layer of width 2σ. Adapted from Zweibel et al. [146].

where S is the Lundquist number defined as the ratio of a resistive diffusion time scale τ_{res} to an Alfvén wave crossing time scale τ_{Alf}. S is described as

$$S \equiv \frac{LV_A}{D_\eta} = \frac{\tau_{res}}{\tau_{Alf}}, \tag{1.5}$$

where $D_\eta \equiv \frac{\eta c^2}{4\pi}$ is magnetic diffusivity in units of $length^2 time^{-1}$. In astrophysics, the Lundquist number is typically somewhere between 10^9 and 10^{20}. Thus, the reconnection rate in Sweet–Parker model is very low. For example, the Sweet-Parker model predicts solar flares occur on time scales of months which is much slower than timescales of tens of seconds to tens of minutes in reality.

1.2.2 Fast Reconnection: Petschek Model

From Equation (1.4), Sweet-Parker reconnection is slow because of large diffusion layer L. By reducing L, Petschek model [105] is developed to explain magnetic reconnection that is fast

in the limit of low resistivity. Figure 1.7 shows the X-line geometry proposed by Petschek in 1964. The inflow and outflow are separated by slow mode shocks. Thus, the reconnection rate is increased by $\sqrt{L/L^*}$. The upper limit of reconnection rate is $\pi/(8\ln S)$, which is fast enough to support most support most phenomena in astrophysics. However, simulations of resistive MHD reconnection with uniform resistivity showed the development of elongated current sheets. Thus, stable resistive MHD reconnection needs an increased resistivity near X-point. Petschek model requires localized anomalous resistivity in resistive MHD simulation. Anomalous resistivity requires collisionless effects, which occur only on short length scales where MHD breaks down. Therefore, Petschek model is not a good one for fast reconnection in real space plasma.

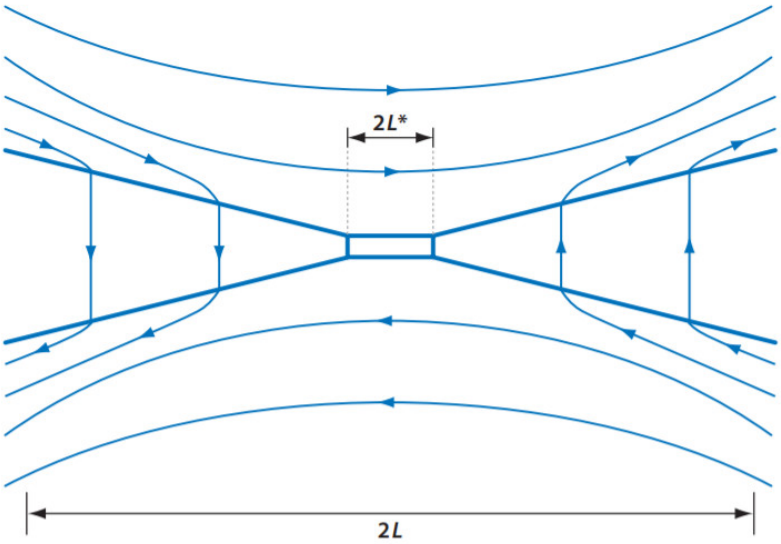

Figure 1.7: Magnetic field geometry for Petschek model. Adapted from Narita et al. [146].

1.2.3 Collisionless Reconnection

In the Sweet–Parker model and Petschek model, electric field in diffusion region is given by resistive electric field $\eta\mathbf{J}$ due to particle collision; Electric field out of diffusion region is balanced by convection term $-\frac{\mathbf{V}\times\mathbf{B}}{c}$. The reconnection rate for the two models is determined by η. However, the particle mean free path in real space plasma is usually very large and particles are considered as collisionless. Therefore, collisionless reconnection or Hall reconnection is used to explain the reconnection in real space. In collisionless reconnection, electrons and ions

are considered as different fluid since they move quite differently in the diffusion layer because of the mass difference between ions and electrons.

The generalized Ohm's law [133] is used in two-fluid assumption and given by

$$\mathbf{E} + \frac{\mathbf{V} \times \mathbf{B}}{c} = \eta \mathbf{J} + \frac{\mathbf{J} \times \mathbf{B}}{\mathrm{e} n_e c} - \frac{\nabla \cdot \mathbf{P}_\mathrm{e}}{n_e e c} + \frac{m_e}{n_e e^2} \frac{\mathrm{d}\mathbf{J}}{\mathrm{d}t}, \tag{1.6}$$

where the four terms on the right-hand side are resistive term, Hall term, electron pressure tensor term and electron inertia term. The first term is negligible in collisionless reconnection. On length scales shorter than the ion inertial length ($\frac{c}{\omega_{pi}}$) and larger than ion inertial length ($\frac{c}{\omega_{pe}}$) , ions decouple from electrons. The magnetic field line becomes frozen into the electron fluid rather than the bulk plasma flow. On these scales, Hall term is dominating. The electrons continue flowing inward and the field fine is reconnected within electron diffusion layer, which is much thinner than ions diffusion layer [15]. In the electron diffusion region, the inertia term and pressure tensor term are dominating. Figure 1.8 shows the schematic of collisionless reconnection. Since electrons flow and ions flow move in different path, strong Hall currents are generated. The Hall currents in turn induce out-of-plane quadrupolar Hall magnetic field as shown by the green color in Figure 1.8. Hall effects are thought as the key factor of fast reconnection in collisionless reconnection models [14]. Hall currents and quadrupolar magnetic field are often used as typical signatures of magnetic reconnection in the magnetotail [41, 95] and magnetopause [94, 131, 39].

1.2.4 Multiple X-line Reconnection

In 3-D space, multiple X-line reconnection [74] is proposed to explain Flux Transfer Events (FTEs) at the dayside magnetopause associated with twisted field lines (flux ropes). The multiple X-line reconnection is illustrated in Figure 1.9. At $t = t_1$, multiple X-lines are shown in the figure. After reconnection, the magnetic tension make reconnected field lines move. At $t = t_2$, reconnection occurs among the reconnected field lines again at the new multiple X-lines and two flux tubes (helical field lines) formed as shown in Figure 1.9b. As time proceeding, at $t = t_3$, new flux tubes keep forming wrapping the old ones. This process stops when the size is large enough and no reconnection occurs.

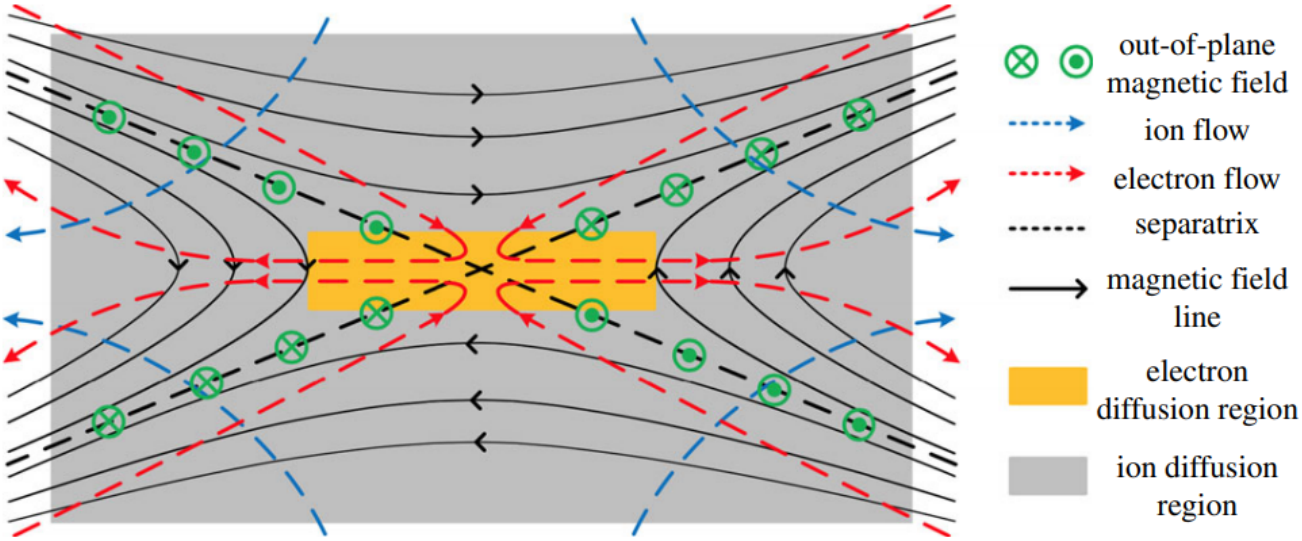

Figure 1.8: Schematic of collisionless reconnection. Adapted from Zweibel et al. [147].

1.3 Substorms

A substorm is a transient, complex phenomenon lasting for the order of one hour or less, during which energy is rapidly released in the magnetotail. Initially, the terms polar magnetic substorm and auroral substorm refer to polar magnetic disturbances and the sudden activation of aurora [1]. Later, the term magnetospheric substorm was introduced to represent magnetospheric disturbances accompanied by both polar magnetic and auroral substorms. A substorm typically has three phases, i.e. growth phase, expansion phase and recovery phase. When IMF turns southward, the growth phase starts. Interplanetary and geomagnetic field lines merge at the dayside magnetopause due to magnetic reconnection. The reconnected field lines are convected to the magnetotail and magnetic energy is accumulated in the tail [16, 56]. The growth phase typically lasts for about one hour.

The time of substorm onset and the beginning of the expansion phase is that when the tail is unstable and would like to release the energy. The expansion phase takes about 30-60 minutes. Many interesting phenomena occur in this phase. Bursty bulk flows (BBFs) [5], which are temporally and spatially localized high-speed streams of the plasma in the tail, are found to be an important dynamical consequence of magnetic reconnection, a process resulting in the changing of magnetic topology and release of magnetic energy. Magnetic flux ropes and

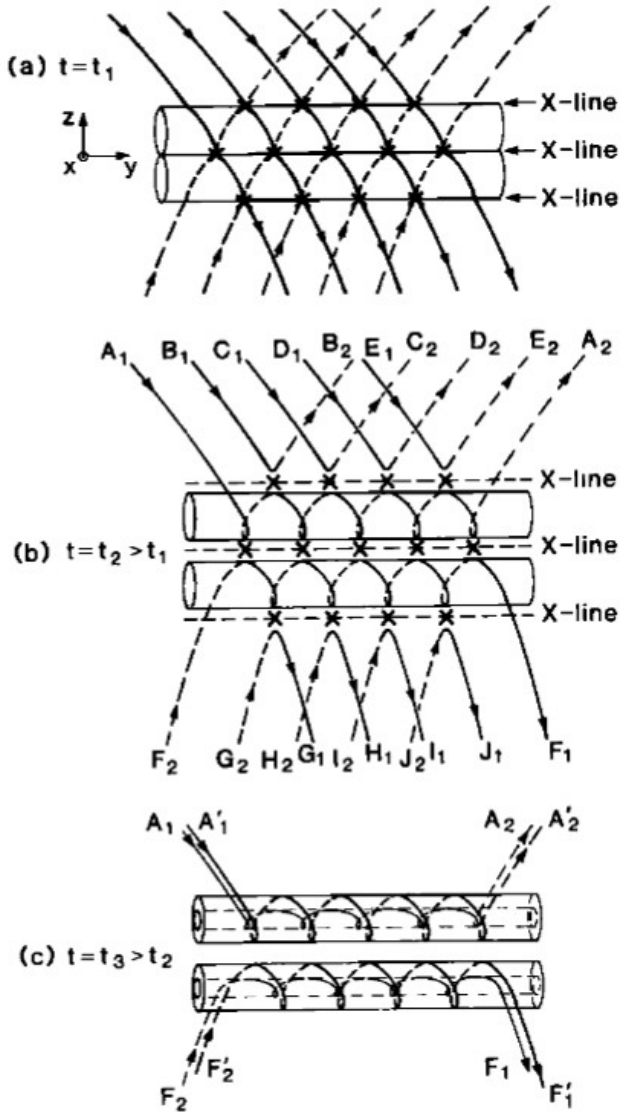

Figure 1.9: Schematic of multiple X-line reconnection. Adapted from Lee et al. [74].

dipolarization fronts, referring to the alteration of magnetic field configuration from stretched to more dipolarized form, are the most notable structures associated with BBFs. The cross-tail current is disrupted and diverted into the ionosphere through field-aligned currents by the substorm current wedge (SCW) [93]. Two models in are proposed to explain the onset time of substorms [8, 87]. Reconnection model suggests near-Earth magnetic reconnection between -20 and -30 Earth radii in the magnetotail is thought to trigger magnetospheric substorms onset followed by current disruption and auroral brightening. However, current disruption model suggests the initiation of the substorm expansion phase is triggered by the disruption of the thin near-Earth current sheet. The current disruption causes further thinning of current sheet

resulting in magnetic reconnection. Near-Earth magnetic reconnection in the magnetotail is thought to trigger magnetospheric substorms onset via the observation of THEMIS spacecrafts [8]. But Lui [87] does not agree with this conclusion. The underlying mechanism is still under controversy and more evidences are needed from future simulation and observation study.

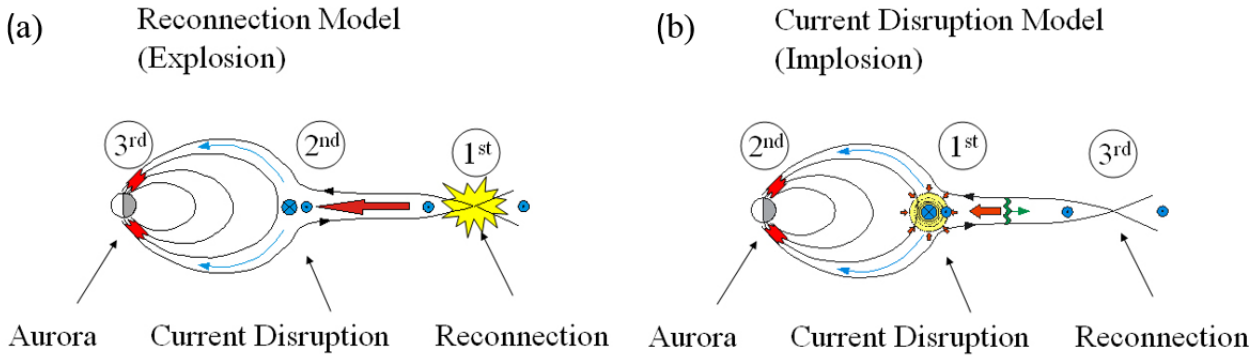

Figure 1.10: Schematic of (a) reconnection model and (b) current disrution model. Adapted from NASA/Goddard Space Flight Center Conceptual Image Lab.

The magnetosphere starts to recover after near-earth reconnection ceases. The recovery phase lasts about 1-2 hours. In over half the substorms, the expansion phase is triggered when the dayside reconnection stops because of the northward turning of IMF.

During substorms, the aurora changes in brightness and locations as shown in Figure 1.11. Brightening of aurora followed by westward traveling surge appear on a pre-existing auroral oval.

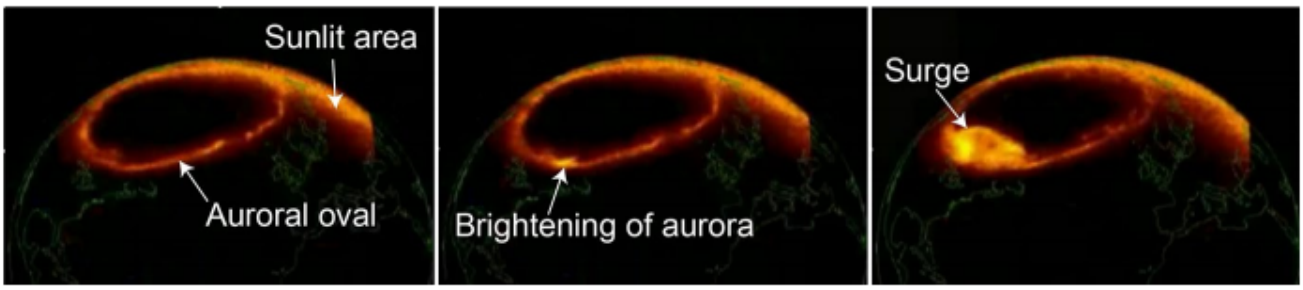

Figure 1.11: Development of an auroral substorm observed by the Polar satellite. Adapted from Ebihara et al. [40].

1.3.1 BBF

High-speed plasma flows in the magnetotail plasma sheet are first reported by Baumjohann(1990) [11]. The occurrence rates in the outer central plsma sheet,inner central plasma sheet and PSBL are shown in Figure 1.12. The occurrence rates of high-speed flows in these three regions decrease with increasing velocity. For speed lager than $800\mathrm{km/s}$, high-speed flows are mainly in the inner plasma sheet and PSBL. Using AMPTE/IRM data , Angelopoulos et al. (1992) [7] first defined the high-speed flows organized in 10-min time flow enhancement as BBFs. BBFs are generally caused by the magnetic reconnection in the near-Earth plasma sheet. The energy transport per unit area in the $y-z$ GSM direction is evaluated in the order of $5\times10^{9}\mathrm{ergs/R_E^2}$. He also concluded that $60\%-100\%$ of the transport of mass and energy are the contribution of BBFs in spite of BBFs lasting only $10\%-15\%$ of the observation time in the inner plasma sheet [5]. The spatial scale of BBFs is $\sim 1-3R_E$ by the observations of ISEE 1, ISEE2, THEMIS and CLUSTER spacecrafts [114, 6, 97].

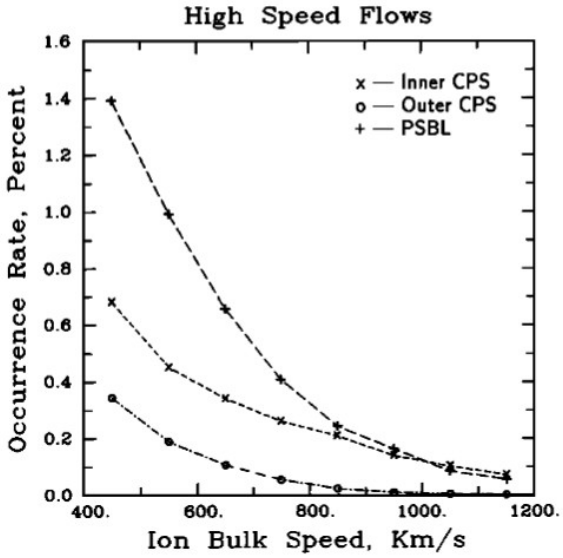

Figure 1.12: The occurrence rates in the outer plasma sheet,inner plasma sheet and PSBL. Adapted from Baumjohann et al. [11].

Eathward BBFs are more frequent as shown in Figure 1.13 with distance from the Earth [11, 5, 120]. Earthward BBFs are braked around $15R_E$ and stopped at dipole-like field and tail-like field transition region due to the dipolar magnetic wall [120] generated by pressure

gradient. The deceleration of the flows generates a dawnward inertia current. The inertia current and pileup of magnetic flux cause the tailward propagating dipolarization of magnetic field [101, 10, 50] generated at $x \sim -10R_E$. Moreover, the braking of earthward BBFs generates various instabilities and waves.

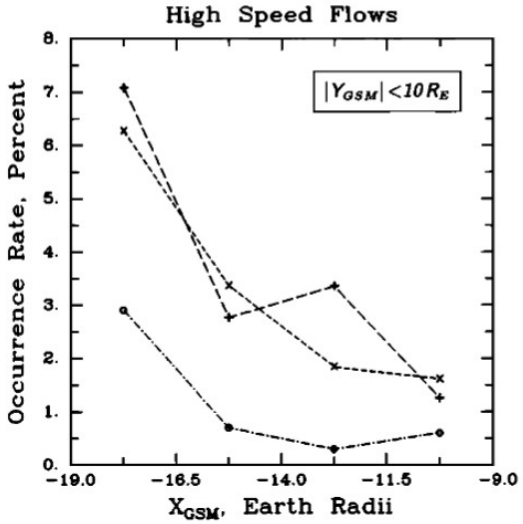

Figure 1.13: The occurrence rates in the outer plsma sheet,inner plasma sheet and PSBL. Adapted from Baumjohann et al. [11].

1.3.2 Dipolarization Fronts (DFs)

Dipolarization initially are often thought as signatures of magnetic flux pileup [55] or caused by a current-driven instability (current disruption) [88]. Duration is about tens of minutes. Dipolarization fronts (DFs), usually observed at the leading edge of BBFs, are a different concept which refers to the sharp magnetic boundaries characterized by a sudden increase of magnetic field B_z [96, 111] preceded by a small B_z dip structure in the plasma sheet. Also, particle number density decreases and energy increases during this process as shown in Figure 1.14. DFs are believed to play a very important role [61] in the transportation of mass and energy [98, 84], generation of field-aligned current (current disruption) [142, 83], excitation of waves [144, 69] and particle energization [111, 144].The DF structure has similar spatial scale [143] with that of BBFs. Considering the similarity of DFs and flux ropes (e.g. bipolar structure of B_x and B_z), DFs can be interpreted as earthward propagating flux ropes based on the multiple X-line

reconnection [111, 86] or Nightside Flux Transfer Events based on transient reconnection in the magnetotail [115, 112, 123].

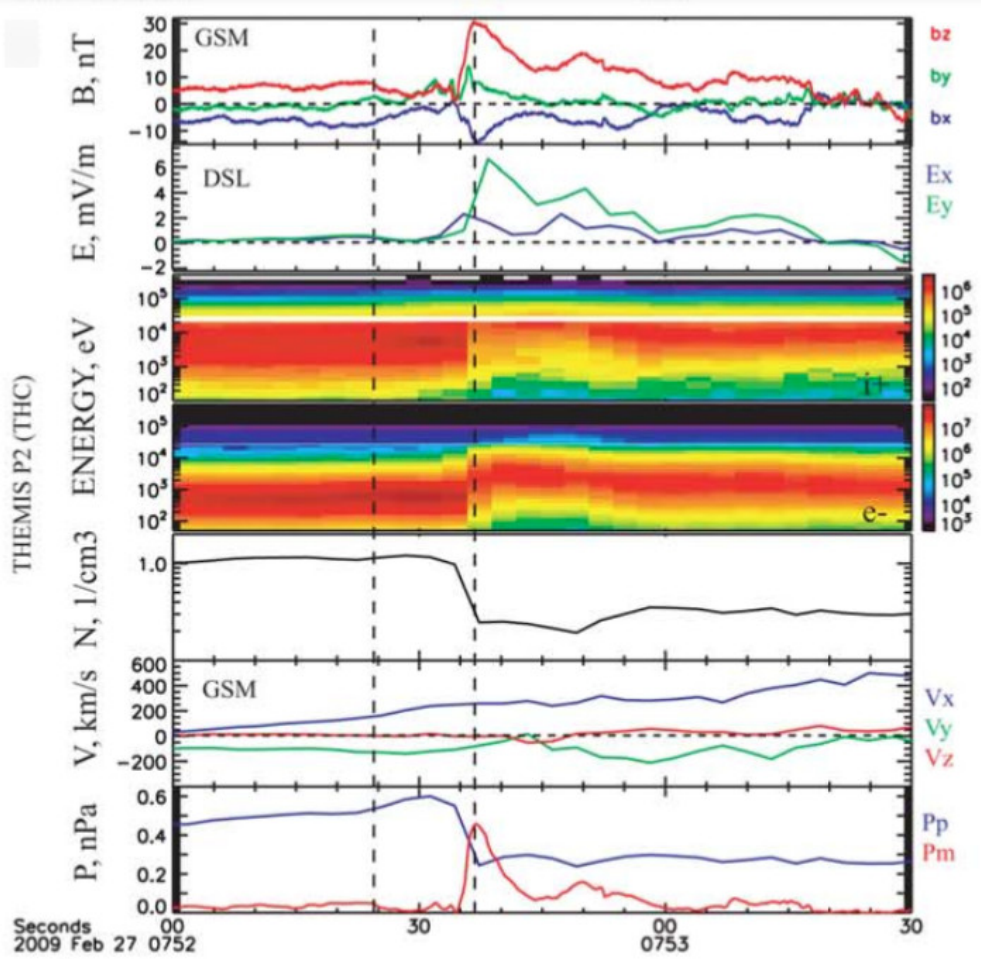

Figure 1.14: DF observed by THEMIS P2 located in the plasma sheet at $x \sim -15R_E$. Adapted from Runov et al. [111].

1.4 Alfvén Waves in the Magnetosphere

Ultra low frequency (ULF) plasma waves are frequently observed in various regions of the magnetosphere [62, 136]. ULF waves with different waveforms and frequency bands (a few mHz to a few Hz) are defined as Pc 1–5 or Pi 1–2 as shown in Figure 1.15. They play an important role in the energy transport over vast distances and magnetosphere-ionosphere coupling. Shear Alfvén waves are fundamental and ubiquitous ULF plasma waves [49, 3, 19] carrying transverse electromagnetic perturbations and thus field-aligned currents. While localized structures associated with the fast flows, e.g., dipolarization fronts, entropy bubbles, and flow vorticies, have also been suggested for the generation of field-aligned currents in the tail [66, 125], shear

	Label	Period range (s)
Continuous pulsations	Pc1	0.2–5
	Pc2	5–10
	Pc3	10–45
	Pc4	45–150
	Pc5	150–600
Impulsive pulsations	Pi1	1–40
	Pi2	40–150

Figure 1.15: Classification of ULF waves. Adapted from Walker et al. [62, 136].

Alfvénic perturbations are a coherent normal mode that can carry the field-aligned currents globally. When the perpendicular (to the magnetic field) wavelength is short and comparable to the ion gyroradius, parallel electric fields $E_\parallel$ can be developed, in the shear Alfvén waves, which facilitate particle heating, acceleration, and transport. Kinetic Alfvén waves (KAWs) are shear Alfvén waves with small perpendicular wavelength comparable to the ion gyroradius or the electron inertial length, i.e., $k_\perp \rho_i \sim 1$, where $k_\perp$ is the perpendicular wave number and ρ_i the ion Larmor radius. During substorms, shear Alfvénic fluctuations, including KAWs, are found in many observations [128, 37, 103, 140, 141, 67, 140, 68]. Figure 1.16 shows the locations where Alfvén waves are observed. KAWs have been found in the plasma sheet associated with fast flows [4, 21, 18], at the plasma sheet boundary layer (PSBL) [141], and in the inner magnetosphere [59, 20, 23]. It has been argued that the KAWs observed around the tail plasma sheet carry sufficient Poynting flux flowing along magnetic field lines toward the ionosphere to power low-altitude auroral acceleration [4].

1.4.1 Linear MHD Waves

Alfvén waves, fast and slow magnetosonic waves are three fundamental MHD wave modes in a plasma and play an important role in plasma heating and transport of energy in space plasma. Alfvén waves, also called shear or torsional Alfvén waves [45], are predicted by and

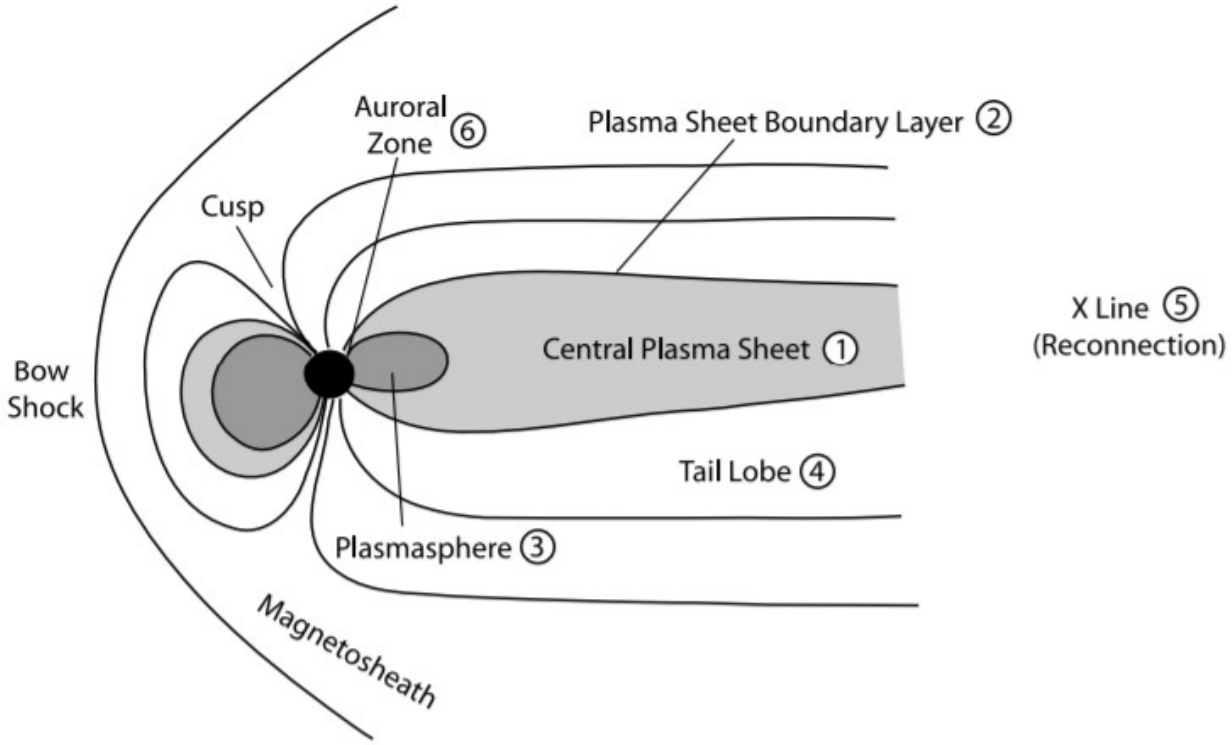

Figure 1.16: Alfvén waves observed in various locations marked by numbers. Adapted from Keiling et al. [68].

named after Hannes Alfvén. In a static, homogeneous plasma with constant density (ρ_0) and pressure (p_0) with a uniform background magnetic field B_0 in z direction. Using linearized MHD equation, the wave equation in matrix form is given by [51]

$$\begin{pmatrix} \omega^2 - k^2 V_A^2 - c_s^2 k_x^2 & 0 & -k_x k_z c_s^2 \\ 0 & (\omega^2 - k_z^2 V_A^2) & 0 \\ -k_x k_z c_s^2 & 0 & (\omega^2 - k_z^2 c_s^2) \end{pmatrix} \mathbf{v_1} = \mathbf{0}, \tag{1.7}$$

where ω is the ion gyrofrequency, k is wave number assumed to lie in the $x - z$ plane without loss of generality; V_A is Alfvén speed and c_s is sound speed. The non-trial solutions are given by

$$\omega = \pm k V_A \cos\theta \equiv \pm k_{||} V_A, \tag{1.8}$$

and

$$\left(\frac{\omega}{k}\right)^2 = \frac{V_A^2 + c_s^2 \pm \sqrt{\left(V_A^2 + c_s^2\right)^2 - 4 V_A^2 c_s^2 \cos^2\theta}}{2}, \tag{1.9}$$

where $k_{\|}$ is the wave number parallel to the background magnetic field and θ is the angle between wave vector and background magnetic field. Equation (1.8) is the dispersion relation for Alfvén waves. The wave is supported by magnetic field line tension in a plasma or conducting fluid [2]. The corresponding wave vector of Equation (1.7) is in the y direction. Thus, the perturbation of velocity is in the y direction. Therefore, Alfvén wave is a transverse wave since perturbations in both velocity and magnetic field are always perpendicular to the direction of wave propagation. The non-dispersive Alfvén wave is also incompressible. The two features are usually used to identify the Alfvén wave [119]. Equation (1.9) gives the dispersion relations of other two modes: fast $(+)$ and slow $(-)$ magnetosonic waves. Magnetosonic waves are longitudinal and compressible. In the slow wave, plasma pressure and magnetic pressure perturbations are out of phase. In the fast wave, these two perturbations are in phase. Both Alfvén waves and magnetosonic waves are present in our hybrid simulation [79]. Figure 1.17 shows the Friedrichs diagram of these three MHD waves in two conditions: $V_A > c_s$ and $V_A < c_s$.

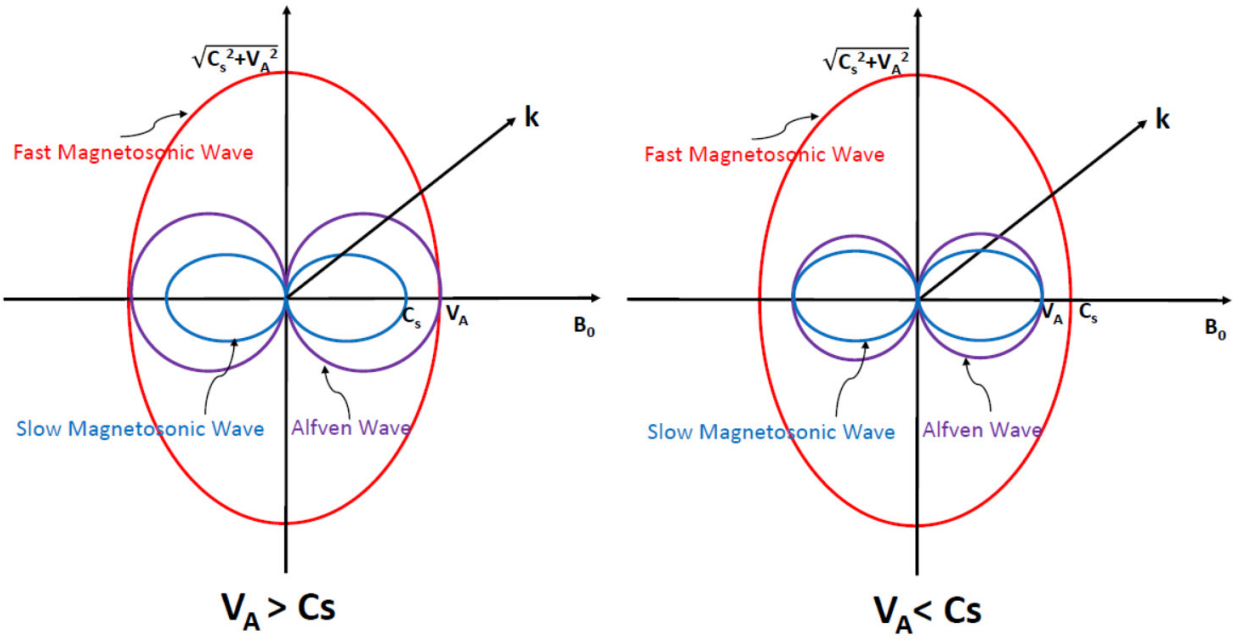

Figure 1.17: Friedrichs diagram of MHD waves, where is the wave vector, $\mathbf{B_0}$ is the background magnetic field, V_A is the Alfvén speed, and c_s is the sound speed.

1.4.2 Dispersive Alfvén Waves

Shear Alfvén waves in the kinetic regime differ from those in an MHD treatment because the short wavelength requires a significant parallel electric field to maintain charge neutrality because of ion density perturbations caused by the electron pressure gradient (when the electron plasma beta is larger than the electron to ion mass ratio) or electron inertia (when the electron plasma beta is less than the electron to ion mass ratio). When the electron thermal speed is higher than the Alfvén speed, the parallel electric field counteracts electron pressure (which would push the electrons away from the ion density perturbations) [53]. The dispersive Alfvén waves are called KAWs (Kinetic Alfvén Waves). When the electron thermal speed is lower than the Alfvén speed, the electric field must overcome the electron inertia (which prevents the electrons from responding rapidly to the ion density perturbations) [48]. This kind of Alfv'en waves are called IAWs (Inertial Alfvén Waves).

Hasegawa first suggested that the parallel electric fields associated with small-scale KAWs could efficiently accelerate particles on magnetic field lines [53]. KAWs were further suggested as a mechanism that gives rise to particle acceleration on auroral field lines [47] as well as transverse ion heating in that region [130]. Chaston et al.(2009) presented observations in the magnetotail from the Cluster spacecraft showing that KAWs radiate outwards from the X line with outward energy fluxes equivalent to that contained in the outstreaming ions [21]. Wave-particle energy exchange has been confirmed between KAWs and plasma particles in the PSBL by high-resolution Magnetospheric Multiscale (MMS) mission observations [44]. Thus, KAWs can be an important mechanism in plasma transport, plasma heating and particle acceleration [54, 22].

The basic properties of KAWs are described by their dispersion relation. While MHD Alfvén waves satisfy the relation $\omega = k_{\parallel} V_A$, the dispersion relation of KAWs can be written as

$$\omega^2 = k_{\parallel}^2 V_A^2 \left[1/\left(1 - \Gamma_0\left(k_{\perp}^2 \rho_i^2\right) e^{-k_{\perp}^2 \rho_i^2}\right) + T_e/T_i\right] k_{\perp}^2 \rho_i^2, \tag{1.10}$$

where Γ_0 is the full Bessel function, ρ_i is the ion gyroradius, and T_e and T_i are the electron and ion temperatures, respectively. Employing a Padé approximation $\Gamma_0(k_{\perp}^2 \rho_i^2) e^{-k_{\perp}^2 \rho_i^2} \approx 1/(1 +$

$k_\perp^2\rho_i^2$), the relation can be simplified to

$$\omega^2 = k_\parallel^2 V_A^2[1 + (1 + T_e/T_i)k_\perp^2\rho_i^2] = k_\parallel^2 V_A^2[1 + k_\perp^2(\rho_i^2 + \rho_s^2)], \tag{1.11}$$

where $\rho_s = (T_e/m_i)^{\frac{1}{2}}/\Omega_i$, with Ω_i being the ion cyclotron frequency [63]. Since shear Alfvén waves possess transverse polarizations in both the electric and magnetic fields, the polarization relation of KAWs can be expressed as

$$|\delta E_\perp/\delta B_\perp| = V_A\left(1 + k_\perp^2\rho_i^2\right)\left[1 + k_\perp^2(\rho_i^2 + \rho_s^2)\right]^{-1/2}, \tag{1.12}$$

where $\delta E_\perp$ is the perturbed electric field in the direction of $k_\perp$; $\delta B_\perp$ is the perturbed magnetic field, which is perpendicular to both the background magnetic field and $\delta E_\perp$. Figure 1.18 shows the polarization relation of KAWs generated in the magnetopause boundary layer because of mode conversion [22]. The parallel electric field of KAWs can be expressed as [90, 63, 68]

$$\left|\delta E_\parallel/\delta E_\perp\right| = k_\parallel k_\perp \rho_s^2/(1 + k_\perp^2\rho_i^2). \tag{1.13}$$

Shear Alfvén waves must also satisfy the Walén relation, which describes the relationship between fluctuations of velocity and magnetic field [135, 12, 60, 9]. In the general cases with ion temperature anisotropy, the Walén relation in the de Hoffmann-Teller (HT) frame, in which the convection electric field is zero, can be written as

$$\delta\mathbf{V} = \pm\xi^{\mathbf{1/2}}\delta\mathbf{V_A}, \tag{1.14}$$

where $\delta\mathbf{V}$ is the plasma velocity in the HT frame , $\delta\mathbf{V_A} = \delta\mathbf{B}/\sqrt{\mu_0\rho}$ is the fluctuation of magnetic field in the form of the Alfvén speed, $\xi = 1 - \mu_0\frac{P_\parallel - P_\perp}{B^2}$ is the thermal anisotropic parameter, and the $+(-)$ sign corresponds to $k_\parallel < 0$ (> 0). Nevertheless, the Walén relation is modified when including the particle kinetic effects. Based on the kinetic-fluid model [24, 31,

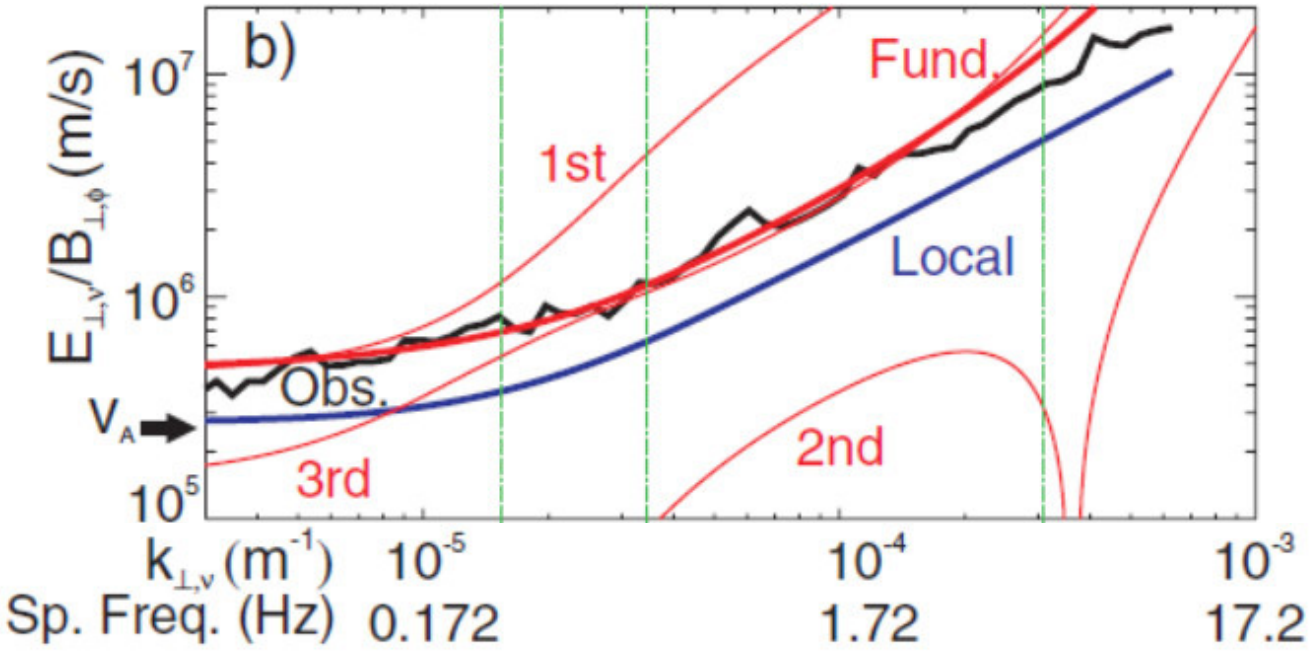

Figure 1.18: The wave spectrum of $\delta E_\perp/\delta B_\perp$ from observations (black), local wave dispersion (blue) and nonlocal solutions (red) for the fundamental through to third harmonic as a function of $k_\perp$ shows the polarization relation of KAWs generated in the magnetopause boundary layer because of mode conversion. The green line denotes the theoretical relation and the dots are from hybrid simulation. Adapted from Chaston et al. [22].

32], the Walén relation of KAWs (see A.1 for derivation) is given by

$$\delta \mathbf{V}_i \approx \pm \delta \mathbf{V}_A \left(\frac{1 + k_\perp^2 \lambda_e^2}{1 + \left(1 + \frac{T_e}{T_i}\right) k_\perp^2 \rho_i^2} \right)^{1/2} \left(\frac{1}{1 + 1.25 k_\perp^2 \rho_i^2} \right), \tag{1.15}$$

where λ_e is electron skin depth. Note that equation (1.15) is valid for either the inertial Alfvén wave or the kinetic Alfvén wave with ion acoustic (hot electron) and/or ion gyroradius effects. Dropping $k_\perp \lambda_e$ for KAWs in the outer magnetosphere, the Walén relation of KAWs in hybrid model can be simplified as

$$\delta \mathbf{V}_i \approx \pm \delta \mathbf{V}_A \left(\frac{1}{\sqrt{1 + \left(1 + \frac{T_e}{T_i}\right) k_\perp^2 \rho_i^2}} \right) \left(\frac{1}{1 + 1.25 k_\perp^2 \rho_i^2} \right). \tag{1.16}$$

1.5 Motivation and Outline of the Dissertation

Although KAWs have been observed in the magnetotail plasma sheet as seen by the transverse magnetic and electric field fluctuations, enhanced spectral energy densities and parallel Poynting flux in Figure 1.19 [21], their generation mechanisms and global transport properties are still unclear. Previous theories and local simulations have shown that in general KAWs can

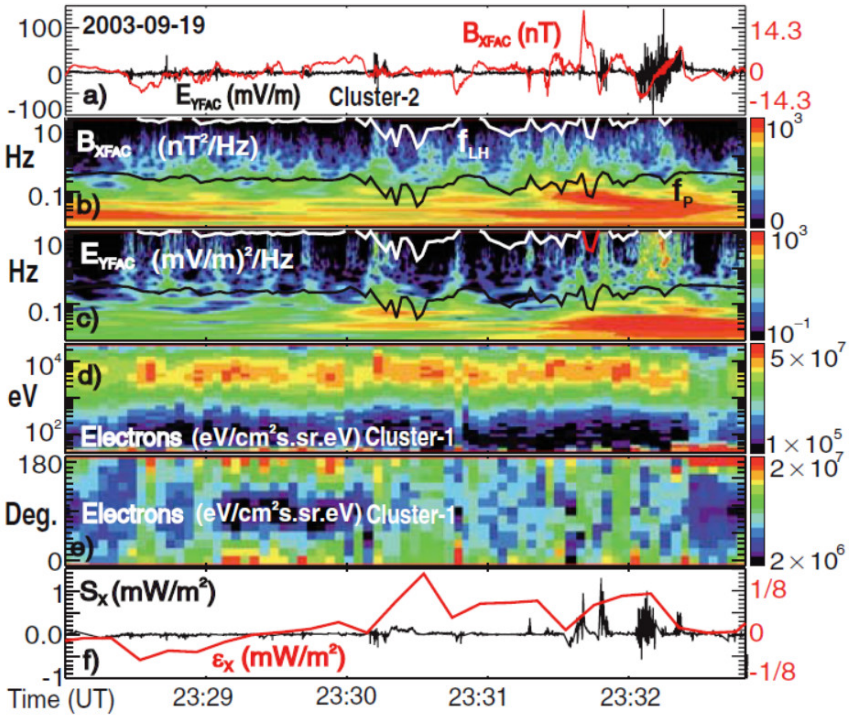

Figure 1.19: KAWs observed in the magnetotail plasma sheet by CLUSTER. (a) Transverse magnetic (B_{XFAC}) and electric field (E_{YFAC}) fluctuations observed on Cluster 2 in field-aligned coordinates (FAC). YFAC lies in the spacecraft spin plane orthogonal to the projection of $\mathbf{B_0}$ into this plane, and ZFAC is field-aligned. (b) B_{XFAC} dynamic spectrogram; the white line is the lower hybrid frequency (f_{LH}), and the black line the proton gyro frequency (f_p).(c) E_{YFAC} dynamic spectrogram; (d) electron energy spectrogram;(e) electron pitch angle spectrogram; (f) Poynting flux(S_X) and ion energy flux (ε_X) along X_{GSM}. Adapted from Chaston et al. [21].

be generated via the fundamental mechanisms such as magnetic reconnection [116, 75, 76], mode conversion [54, 63] and phase mixing [53, 132, 50]. Shay et al. (2011) [116] have shown the signature of KAWs generated by reconnection via a two-dimensional (2-D) particle-in-cell (PIC) code as shown in Figure 1.20. Liang et al. (2016, 2017) have presented a 3-D hybrid simulation in a Harris current sheet showing that KAWs are found throughout the transient plasma

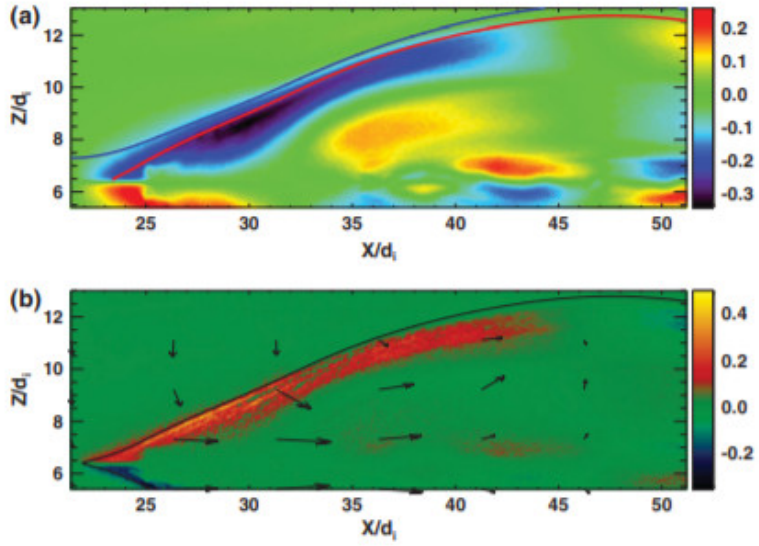

Figure 1.20: Contours of (a) B_y and (b) parallel Poynting flux show the signatures of KAWs generated by reconnection via a 2-D PIC simulation. Adapted from Shay et al. [116].

bulge region and propagate outward along field lines with a slightly super-Alfvénic velocity [75, 76]. Dai et al. (2017) suggested KAW eigenmode [29] as an explanation of Hall fields and currents in the process of magnetic reconnection [30] . Mode conversion from compressional waves to KAWs under various solar wind conditions at the dayside magnetopause has been studied using hybrid simulations [81, 80, 118, 117] as shown in Figure 1.21. The compressional waves on the magnetosheath side ($x < 42.5$) dominated by perturbations in B_x, E_y, and N are converted to KAWs at the magnetopause between $x \sim 47 - 60$. Kinetic Alfvén waves can also be generated by large-scale phase mixing of MHD shear Alfvén waves.

Since the magnetotail contains multiple plasma boundary layers embedded in and coupled with the global dynamics, multiple boundary layers exist in the highly nonuniform plasma and magnetic field. Questions remain. Will KAWs be generated at magnetic reconnection and those boundaries? What will happen when Alfvén waves interact with the boundaries during their propagation? How are these waves coupled to the ionosphere? The generation and evolution of KAWs in the global system are still far from being understood. To answer these questions, a global model is necessary because spatial and temporal scales of the generation and evolution of KAWs vary from particle kinetic scales to the global Alfvén convection scales, which is hard for local simulations and observations to deal with. A kinetic model is necessary because fluid (MHD) models can not deal with KAWs on particle kinetic scales. A three-dimensional

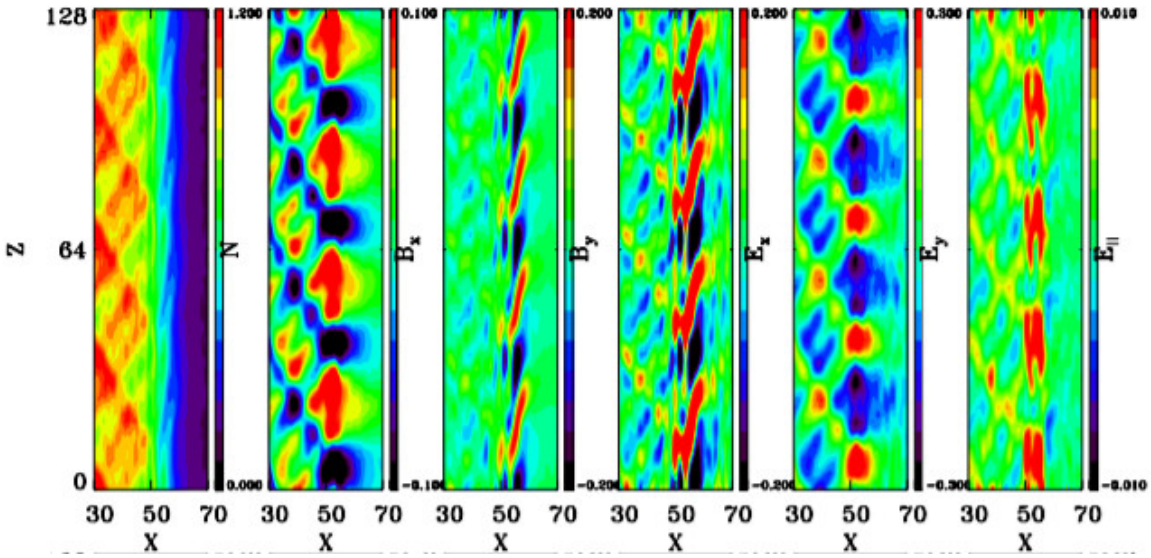

Figure 1.21: Contours of various quantities in the xz plane via a 3-D hybrid simulation showing mode conversion from compressional waves to KAWs. Adapted from Lin et al. [80].

(3-D) model is necessary because the 3-D, nonlinear physics is fundamentally important for understanding KAWs. On the global scale, spatial variations and wave vector $\mathbf{k}$ in the east-west direction are also important in the tail dynamics.

The objective of this thesis is to understand the fundamental mechanisms of generation of KAWs and their signatures and propagation associated with magnetotail fast flows in the self-consistent solar wind-magnetosphere interaction for cases under southward IMF, and correlate the simulation results with observations. The tool we use is the 3-D global hybrid model. The reason we use hybrid code is that particle-in-cell (PIC) models [33, 92, 116] treat electrons and ions as individual particles, and are used to address reconnection problem locally due to the limited computing resources. In MHD models, all plasma species are described as a single or multiple conducting fluid [137, 89, 108, 110], and thus the kinetic effects have been fully neglected. Hybrid models fall between them, in which ions are treated as fully kinetic particles and electrons as a conducting fluid. They are used to model phenomena on a spatial scale as low as ion inertial and ion gyroradius scales, and valid for low-frequency physics up to $\omega \sim \Omega_i$ [78, 102, 65, 79, 134]. Thus, the 3-D global hybrid model including both the dayside and nightside magnetosphere is a suitable tool to study the dynamics of KAWs from the magnetotail to the ionosphere.

The thesis is organized as follows. The simulation model is described in Chapter 2. We investigate the generation and evolution of KAWs in the magnetotail associated with magnetotail reconnection and fast flows by using a 3-D global hybrid code in Chapter 3. The role of flow-braking region in the generation and propagation of KAWs is studied. Ions acceleration in the magnetotail is also discussed. In Chapter 4, we will correlate the simulation results with observations from THEMIS and DMSP (Defense Meteorological Satellite Program) satellites and with solar wind parameters and geomagnetic activity indices from the OMNI data sets . Chapter 5 gives the summary and future study.

Chapter 2

3-D Global-Scale Hybrid Simulation Model

The topic of this thesis is the generation and evolution of KAWs on the spatial and temporal scales varying from particle kinetic scales to the global Alfvén convection scales. The suitable simulation model should be a 3-D global kinetic model. The simulation tool used in this thesis is the Auburn Global Hybrid Code in 3-D (ANGIE3D) [79, 82], a three dimensional global hybrid code including both the dayside and nightside magnetosphere based on a previous code that contains only the dayside magnetosphere [126, 78]. In this code, ions (protons) are treated as fully kinetic particles (macroparticles), while electrons are treated as a massless fluid. An introduction to ANGIE3D is given in this chapter. Hybrid simulation scheme is introduced in Section 2.1. The two-cell grids are set up in Section 2.2. Section 2.3 gives the detail of time-integration of particles and fields. The work flow of ANGIE3D is summarized in Section 2.4.

2.1 Hybrid Simulation Scheme

The simulation domain extends from $x = -60\ R_E$ on the nightside to $x = +20\ R_E$ on the dayside, $y = -30\ R_E$ to $+30\ R_E$ in the dawn-dusk direction, and $z = -30\ R_E$ to $+30\ R_E$ in the north-south direction in the GSM and Cartesian coordinate system. There are six outer boundaries. The fixed solar wind and interplanetary magnetic field (IMF) conditions are imposed at $x = +20\ R_E$, while the outflow boundary conditions (zero-gradient boundary condition in the normal direction) are used at the other five boundaries. The inner boundary is located at $r = 3.5\ R_E$, where a magnetospheric-ionospheric electrostatic coupling model is employed. The thickness of the ionosphere is quite tiny compared with the size of Earth. Ohm's law for

the ionosphere is written as

$$\mathbf{J} = \bar{\bar{\Sigma}} \cdot \mathbf{E} = \mathbf{\Sigma_{\parallel}} \mathbf{E_{\parallel}} + \mathbf{\Sigma_P} \mathbf{E_{\perp}} + \mathbf{\Sigma_H} \mathbf{B_d} \times \mathbf{E} / \mathbf{B_d}, \tag{2.1}$$

where $\bar{\bar{\Sigma}}$ is the conductance tensor with $\Sigma_{\parallel}$, Σ_P and Σ_H being parallel height-integrated conductivity, Pederson conductivity and Hall conductivity, respectively. $\mathbf{B}_d$ is the dipole magnetic field, and given by

$$\mathbf{B}_d = -B_{eq} \left(\sin I \mathbf{e}_r + \cos I \mathbf{e}_\theta \right), \tag{2.2}$$

and I is the inclination angle of a geomagnetic field line with respect to the horizontal ionosphere, and given by

$$\sin I = \frac{2 \cos \theta}{\left(1 + 3 \cos^2 \theta\right)^{1/2}}. \tag{2.3}$$

The ionosphere is regarded as a two-dimensional spherical current sheet, and only currents on a scale much larger than the thickness of ionosphere are studied. The current continuity equation under such assumptions requires [64]

$$\nabla \cdot \mathbf{J} = J_{\parallel} \sin I, \tag{2.4}$$

where $J_{\parallel}$ is the field-aligned current density. The Ohm's Law for the ionospheric current for a thin shell model is written as

$$\mathbf{J} = \bar{\bar{\mathbf{\Sigma}}} \cdot \mathbf{E} = - \begin{pmatrix} \Sigma_{\theta\theta} & \Sigma_{\theta\phi} \\ \Sigma_{\phi\theta} & \Sigma_{\phi\phi} \end{pmatrix} \cdot \nabla \phi = \begin{pmatrix} \frac{\Sigma_{\parallel} \Sigma_P}{\Sigma_{zz}} & -\frac{\Sigma_{\parallel} \Sigma_H \sin I}{\Sigma_{zz}} \\ \frac{\Sigma_{\parallel} \Sigma_H \sin I}{\Sigma_{zz}} & \Sigma_P + \frac{\Sigma_H^2 \cos^2 I}{\Sigma_{zz}} \end{pmatrix} \cdot \nabla \phi, \tag{2.5}$$

where $\Sigma_{zz} = \Sigma_{\parallel} \sin^2 I + \Sigma_P \cos^2 I$ and Φ is the electric potential. Thus, the ionospheric potential equation [109] is obtained as

$$\nabla \cdot (-\bar{\bar{\Sigma}} \cdot \nabla \Phi) = J_{\parallel} \sin I. \tag{2.6}$$

Considering the parallel conductance $\Sigma_{\parallel}$ is usually much greater than the perpendicular conductances, Σ is simplified as [91]

$$\bar{\bar{\Sigma}} = \begin{pmatrix} \frac{\Sigma_P}{\sin^2 I} & -\frac{\Sigma_H}{\sin I} \\ \frac{\Sigma_H}{\sin I} & \Sigma_P \end{pmatrix}. \tag{2.7}$$

Uniform Pederson conductivity $\Sigma_P = 5$ Siemens and Hall conductivity $\Sigma_H = 0$ Siemens are adopted in the simulation. The field-aligned currents, mapped along the geomagnetic field lines from the inner boundary into the ionosphere, are the input to the righthand of the ionospheric potential equation (2.6).

In the simulation units, the magnetic field B is scaled by the IMF B_0; the ion number density N by the solar wind density ion number N_0; the time t by the inverse of the solar wind ion gyrofrequency (Ω_{i0}^{-1}); the flow velocity V by the solar wind Alfvén speed V_{A0}; the temperature by V_{A0}^2; the length in units of the Earth's radius R_E. Thus, the equation for ion particle motion, in the simulation units, is written as

$$\frac{d\mathbf{v}_p}{dt} = \mathbf{E} + \mathbf{v}_p \times \mathbf{B} - \nu(\mathbf{V}_p - \mathbf{V}_e), \tag{2.8}$$

where $\mathbf{v}_p$ is the ion particle velocity, ν is an ad hoc current-dependent collision frequency with typical peak collision frequency $\sim$ 0.01–0.1 Ω_i [129] used to model the anomalous resistivity, and $\mathbf{V}_p$ and $\mathbf{V}_e$ are the bulk flow velocities of ions and electrons, respectively. A cold, incompressible ion fluid coexists with particle ions [126, 78] in the inner magnetosphere ($r < 6.5\ R_E$), considering this simulation revolves the ion kinetic physics in the outer magnetosphere. The number density of the cold ion fluid is assumed to be $N_f = (N_{eq}/r^3)[1 - \tanh(r - 6.5)]$, where N_{eq} = 1000 cm^{-3}. Cold ion fluid plays an important role in the induction of field-aligned currents and the transmission of Alfvén waves in the inner magnetosphere. Even though the number density of cold ion fluid is time invariant, the velocity does change with time. Considering ion number density of ion fluid is very large, the pressure tensor term is dropped. The momentum equation for cold ion fluid ($\mathbf{V}_f$) is given by

$$\frac{\mathrm{d}\mathbf{V}_f}{\mathrm{d}t} = \mathbf{E} + \mathbf{V}_f \times \mathbf{B} - \nu\left(\mathbf{V}_f - \mathbf{V}_e\right). \tag{2.9}$$

The electron flow speed is calculated from Ampere's law as

$$\mathbf{V}_e = \mathbf{V}_i - \frac{\nabla \times \mathbf{B}}{\alpha N}, \tag{2.10}$$

where $\mathbf{V}_i = (N_p/N)\mathbf{V}_p + (N_f/N)\mathbf{V}_f$ is the total ion bulk flow velocity, with $\mathbf{V}_f$ being the flow velocity of the cold ion flow; $\alpha = (\mu_0 e^2/m_i)$, μ_0 is the permeability of free space, e is the electron charge and m_i is the ion mass. The ion inertial length d_i is set as $d_i = 1/\sqrt{(\alpha N)}$.

The massless electron momentum equation is given as

$$\mathbf{E} = -\mathbf{V}_e \times \mathbf{B} - r\frac{d\mathbf{V}_e}{dt} - \nabla P_e/N - \nu(\mathbf{V}_e - \mathbf{V}_i), \tag{2.11}$$

where r is electron-to-ion mass ratio, P_e is the thermal pressure of the electrons, and $N = N_p + N_f$ is the total ion number density with N_p and N_f being the number densities of discrete ions and cold ion fluid, respectively. Note that $\nabla p_e = T_e \nabla N$ since the electron fluid is assumed to be isothermal, i.e., with a constant temperature T_e. The magnetic field is advanced in time by Faraday's law,

$$\frac{\partial \mathbf{B}}{\partial t} = -\nabla \times \mathbf{E}. \tag{2.12}$$

2.2 Spatial Grids

In order to discretize Maxwell's equations using central-difference approximations with second-order accuracy, different field components are stored for different grid locations and 3-D Yee lattice is adopted in ANGIE3D. The three components of $\mathbf{E}$ are stored on the edges of the cubes at the grid points (i, j, k) while the three components of $\mathbf{B}$ are stored on the edges of the cubes at the half grid points $(i + 1/2, j + 1/2, k + 1/2)$ [126]. The two cells are defined and called E-cell and B-cell, respectively. The two kinds of grid points for E-cell and B-cell are called E-center and B-center, respectively. The E-cell for the $n - th$, $l - th$ and $m - th$ point away from the point (i, j, k) in x, y and z direction is at $(i + n, j + l, k + m)$; The B-center for the

$n-th$, $l-th$ and $m-th$ point away from the point $(i+1/2, j+1/2, k+1/2)$ in x, y and z direction is at $(i+n+1/2, j+l+1/2, k+m+1/2)$. The three components of E are stored at $(i+n+1/2, j+l, k+m)$ for E_x, $(i+n, j+l+1/2, k+m)$ for E_y and $(i+n, j+l, k+m+1/2)$ for E_z. The three components of B are stored at $(i+n, j+l+1/2, k+m+1/2)$ for B_x, $(i+n+1/2, j+l, k+m+1/2)$ for B_y and $(i+n+1/2, j+l+1/2, k+m)$ for B_z. The quantities at E-cell can not be used directly for B-cell and vice versa. It must be interpolated. The density is located at the E-center. The electric current density is defined at the edge of the E-cell.

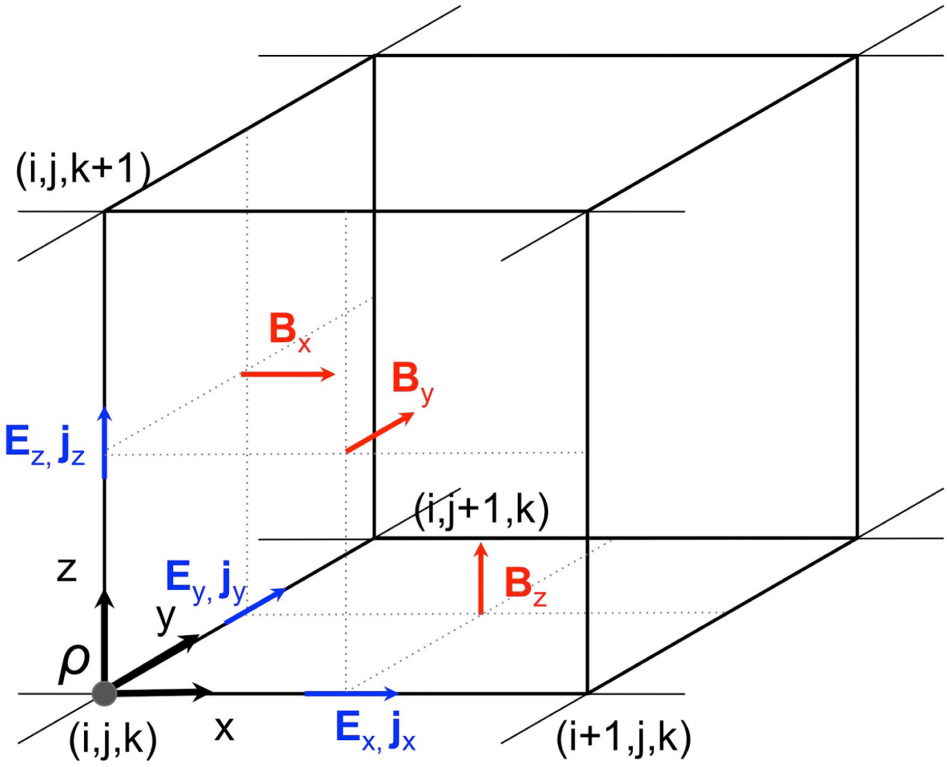

Figure 2.1: Schematic of 3-D Yee lattice. Adapted from Pohl et al. [106].

2.3 Time-Integration of Particles and Fields

Equation (2.8) is simplified by combining equations (2.11) and (2.10) as

$$\frac{d\mathbf{v}_p}{dt} = \mathbf{E}_p + \mathbf{v}_p \times \mathbf{B}, \tag{2.13}$$

where $\mathbf{E}_p$ is given by

$$\mathbf{E}_p = \left(\frac{\nabla \times \mathbf{B}}{\alpha N} - \mathbf{V}_i \right) \times \mathbf{B} + \nu \frac{N_f}{N} \left(\mathbf{V}_f - \mathbf{V}_p \right). \tag{2.14}$$

The equation (2.9) is then written as

$$\frac{\partial \mathbf{V}_f}{\partial t} = -\mathbf{V}_f \cdot \nabla \mathbf{V}_f + \mathbf{E}_f + \frac{N_p}{N} \mathbf{V}_f \times \mathbf{B} - \nu \frac{N_p}{N} \mathbf{V}_f, \tag{2.15}$$

where $\mathbf{E}_f$ is given by

$$\mathbf{E}_f = \left(\frac{\nabla \times \mathbf{B}}{\alpha N} - \frac{N_p}{N} \mathbf{V}_p \right) \times \mathbf{B} + \nu \frac{N_p}{N} \mathbf{V}_p. \tag{2.16}$$

Given that the term $\mathbf{V_f} \cdot \nabla \mathbf{V_f}$ is small, the total derivative on l.h.s of the equation (2.9) can be replaced by the partial derivative $\frac{\partial \mathbf{V}_f}{\partial t}$.

Finally, we can rewrite Faraday's law using electron momentum equation and Ampere's law as

$$\frac{\partial \mathbf{B}}{\partial t} = -\nabla \times \left[\left(\frac{\nabla \times \mathbf{B}}{\alpha N} - \mathbf{V}_i \right) \times \mathbf{B} \right] - \nabla \times \left(\nu \frac{\nabla \times \mathbf{B}}{\alpha N} \right). \tag{2.17}$$

The first term $\frac{\nabla \times \mathbf{B}}{\alpha N}$ on the r.h.s. represents the whistler mode in the limit that the propagation frequency is much lower than the gyro-frequency. The last term on the r.h.s. is the diffusion term which is used to smooth out noisy fluctuations of the magnetic field. Equation (2.17) can be modified by introducing the electron inertia as

$$\frac{\partial}{\partial t} \left[\mathbf{B} + r \nabla \times \left(\frac{\nabla \times \mathbf{B}}{\alpha N} - \mathbf{V}_i \right) \right] = r \nabla \times (\mathbf{V}_e \cdot \nabla \mathbf{V}_e) - \nabla \times \left[\left(\frac{\nabla \times \mathbf{B}}{\alpha N} - \mathbf{V}_i \right) \times \mathbf{B} \right] - \nabla \times \left(\nu \frac{\nabla \times \mathbf{B}}{\alpha N} \right). \tag{2.18}$$

The electron inertia term is very small of the order of the electron-to-ion mass ratio. Its main function is to incur electron polarization drift in the equation. Equation (2.18) is then rewritten as

$$\frac{\partial}{\partial t} \mathbf{B}' = -\nabla \times \mathbf{E}', \tag{2.19}$$

where

$$\mathbf{B}' = \mathbf{B} + r\nabla \times \left(\frac{\nabla \times \mathbf{B}}{\alpha N} - \mathbf{V}_i \right) \tag{2.20}$$

and

$$\mathbf{E}' = r\mathbf{V}_e \times (\nabla \times \mathbf{V}_e) + \left(\frac{\nabla \times \mathbf{B}}{\alpha N} - \mathbf{V}_i \right) \times \mathbf{B} \times \left(v \frac{\nabla \times \mathbf{B}}{\alpha N} \right). \tag{2.21}$$

$\mathbf{E_p}$, $\mathbf{E_f}$, $\mathbf{B}'$ and $\mathbf{E}'$ are the intermediate variants for computational convenience. Note that the magnetic field in our simulation is split into two terms as

$$\mathbf{B} = \mathbf{B}_0 + \mathbf{B}_1, \tag{2.22}$$

where $\mathbf{B_0}$ is the dipole magnetic field plus mirror dipole magnetic field in the initial condition and $\mathbf{B_1}$ is the time-variant fluctuation of $\mathbf{B_0}$. That is because $\mathbf{B_0}$ is curl-free and extremely large in the inner magnetosphere. To reduce the numerical error from the calculation of $\nabla \times \mathbf{B}$, only $\mathbf{B_1}$ is updated in the simulation while $\mathbf{B_0}$ keeps the same value.

The Courant-Friedrichs-Lewy condition ($\frac{|v|\Delta t}{\Delta x} \leq 1$) [26] should be satisfied for convergence when solving certain partial differential equations, where v is V_A for MHD and sound speed for Hydrodynamics. Courant-Friedrichs-Lewy condition requires the time step is small enough. However, massive particles integration need a lot of calculation. Thus, two-time-step integration technique is adopted to integrate the particles and field. The particles are advanced with a time step Δt while the velocity and magnetic field are advanced with a smaller time step δt. Typically, we use $\delta t = \frac{1}{10}\Delta t$.

2.3.1 Particle Push

The leapfrog method with second-order accuracy is employed to advance particles. In the leapfrog method, velocity and positions of particles are known offset from each other by half a time step. Ions are considered located at full-integer time steps while ion velocity is located at half-integer time steps [13]. For particle integration, we are solving

$$\frac{\mathbf{v}_p^{n+1/2} - \mathbf{v_p}^{n-1/2}}{\Delta t} = \mathbf{E}_p^n + \frac{\mathbf{v_p}^{n+1/2} + \mathbf{v_p}^{n-1/2}}{2} \times \mathbf{B}^n. \tag{2.23}$$

An elegant method to solve this equation is Boris method proposed by Jay P. Boris in 1970. Equation (2.23) is rewritten as

$$\mathbf{v}^{+} = \mathbf{v}^{-} + \frac{\Delta t}{2}\left(\mathbf{v}^{+} + \mathbf{v}^{-}\right) \times \mathbf{B}^{n} \tag{2.24}$$

by defining pre-rotation $\mathbf{v}^{-}$ and post-rotation velocity $\mathbf{v}^{+}$ as

$$\begin{cases} \mathbf{v}^{-} = {\mathbf{v}_\mathbf{p}}^{n-1/2} + \frac{\Delta t}{2}\mathbf{E}_p^n, \\ \mathbf{v}^{+} = {\mathbf{v}_\mathbf{p}}^{n+1/2} - \frac{\Delta t}{2}\mathbf{E}_p^n. \end{cases} \tag{2.25}$$

Equation (2.24) is about pure rotation from Lorenz force. The relation of $\mathbf{v}^{-}$ and $\mathbf{v}^{+}$ is given as

$$\mathbf{v}^{+} = \mathbf{v}^{-} + 2\frac{\mathbf{v}^{-} + \mathbf{v}^{-} \times \mathbf{t}}{1 + t^2} \times \mathbf{t}, \tag{2.26}$$

where $\mathbf{t} = -\hat{\mathbf{b}} \tan\frac{\theta}{2} = \frac{\Delta t}{2}\mathbf{B}^n$ with θ being the rotation angle from $\mathbf{v}^{-}$ to $\mathbf{v}^{+}$.

2.3.2 Ion Flow Velocity and Magnetic Field Push

For ion flow velocity, the velocity push via Boris method at sub-loop time step s is given by

$$\begin{cases} \mathbf{V}_f^{-} = \mathbf{V}_f^{s-1/2} + \frac{\delta t}{2}\mathbf{E}_f, \\ \mathbf{V}_f^{+} = \mathbf{V}_f^{-} + \frac{N_p \delta t}{2N}\left(\mathbf{V}_f^{+} + \mathbf{V}_f^{-}\right) \times \mathbf{B} - \nu\frac{N_p \delta t}{2N}\left(\mathbf{V}_f^{+} + \mathbf{V}_f^{-}\right), \\ \mathbf{V}_f^{s+1/2} = \mathbf{V}_f^{+} + \frac{\delta t}{2}\mathbf{E}_f. \end{cases} \tag{2.27}$$

The relationship between $\mathbf{V}_f^{-}$ and $\mathbf{V}_f^{+}$ is similar to equation (2.26). Equation (2.19) is discretized via fourth-order Rouge-Kutta method as

$$\begin{cases} \mathbf{B}'^{1} = \mathbf{B}'^{s} - \frac{\delta t}{2}\nabla \times \mathbf{E}'^{s}, \\ \mathbf{B}'^{2} = \mathbf{B}'^{s} - \frac{\delta t}{2}\nabla \times \mathbf{E}'^{1}, \\ \mathbf{B}'^{3} = \mathbf{B}'^{s} - \delta t\nabla \times \mathbf{E}'^{2}, \\ \mathbf{B}'^{s+1} = \mathbf{B}'^{s} - \frac{\delta t}{6}\nabla \times (\mathbf{E}'^{s} + 2\mathbf{E}'^{1} + 2\mathbf{E}'^{2} + \mathbf{E}'^{3}). \end{cases} \tag{2.28}$$

2.4 Summary

The flow chart of our hybrid code is summarized in Figure 2.2.

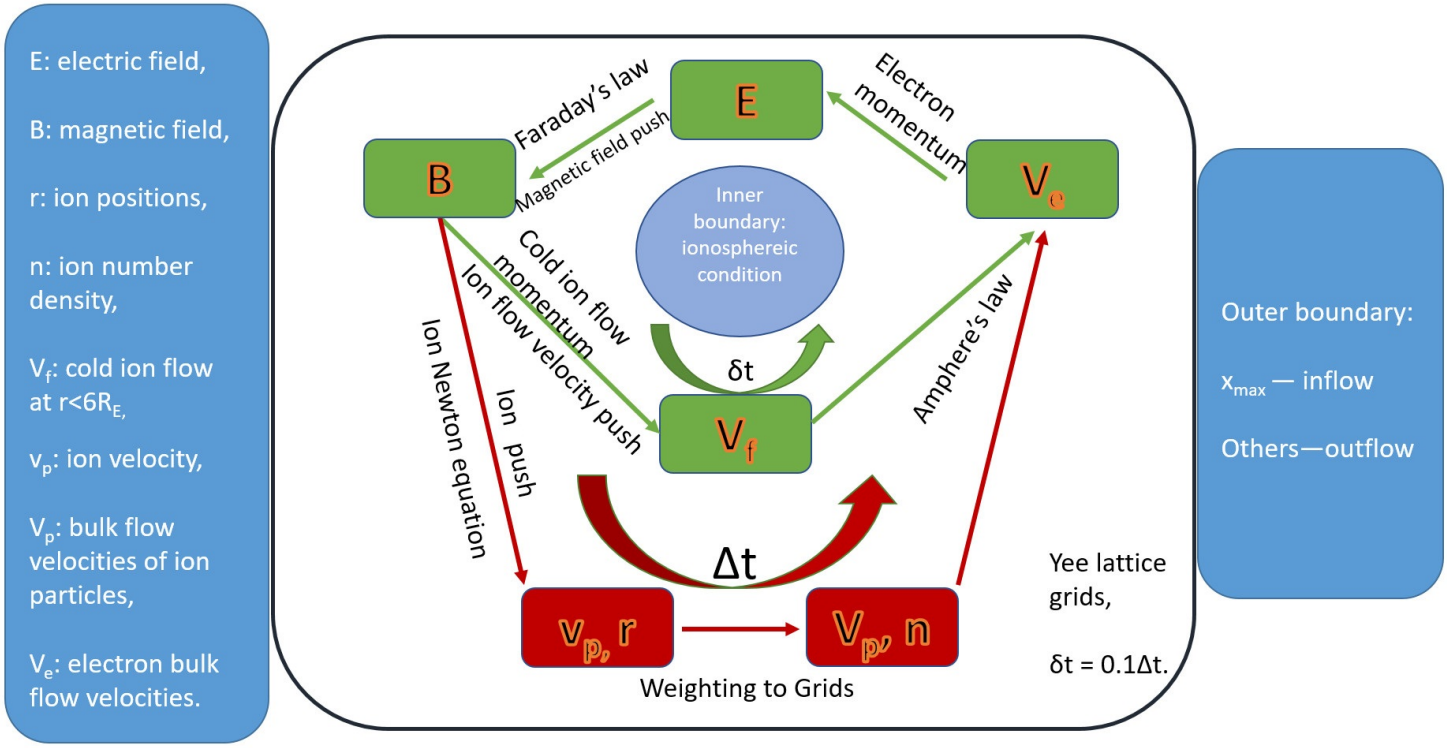

Figure 2.2: Flow chart of hybrid code.

Chapter 3

KAWs from Magnetotail to the Ionosphere in Global Hybrid Simulation

Although KAWs have been observed in the magnetotail plasma sheet, their generation mechanisms and global transport properties are still unclear. We try to answer the following questions in this chapter. Will KAWs be generated at magnetic reconnection and those boundaries? What will happen when Alfvén waves interact with the boundaries during their propagation? How are these waves coupled to the ionosphere? As mentioned in Chapter 1, KAWs play an important role in particle heating and acceleration. Thus, ion acceleration and ion heating are also studied in this chapter.

We use the 3-D global hybrid code, i.e., Auburn Global Hybrid Code in 3-D (ANGIE3D) to reveal the generation, dynamics, and global structure of of KAWs from the magnetotail to the ionosphere for the first time. The case presented with a purely southward IMF is introduced in Section 3.1. The global view of the simulation results including the evolution of fast flows and flux ropes is given in Section 3.2. Section 3.3 presents the identification and dynamics of highly 3-D KAWs generated by the near-Earth magnetotail reconnection. KAWs are also generated at the inner edge of flow-braking region in front of the dipole-like field due to the ion inertial effects as shown in Section 3.4. The total Alfvénic wave energy on the nightside from the magnetotail to the ionosphere is estimated in Section 3.5. The Poynting flux pattern in the ionosphere reveals the importance of KAWs in the brightening of aurora. The ions acceleration owing to KAWs and other mechanisms is studied in Section 3.6. Section 3.7 gives the unusual ion drift motion by tracing ions at the flow-braking region near substorm current wedge. The results of this chapter are summarized in Section 3.8.

3.1 Introduction

In the case presented, a purely southward IMF is chosen, with the field strength $B_0 = 10$ nT and ion number density $N_0 = 6\ \mathrm{cm}^{-3}$, corresponding to a solar wind ion gyrofrequency $\Omega_0 = 0.958\ \mathrm{s}^{-1}$. The solar wind ion inertial length $d_{i0} = c/\omega_{pi0}$ is set as $0.1\ R_E$, where ω_{pi0} is the plasma frequency of solar wind and c is the light speed. Nonuniform cell grids are used, with a grid size of $(\Delta x, \Delta y, \Delta z) = (0.15, 0.15, 0.15)\ R_E$ in the near-Earth regions with $-25\ R_E \leq x \leq 12\ R_E$, $-12\ R_E \leq y \leq 12\ R_E$, and $-10\ R_E \leq z \leq 10\ R_E$ and a lower resolution in other regions. The cell dimensions are set as $n_x \times n_y \times n_z = 337 \times 241 \times 217$. The configuration of the grid is shown in Figure 3.1. A total of 2×10^9 particles are used. A typical particle time step interval is $\Delta t = 0.05\ \Omega_0^{-1}$. Note that the hybrid model is valid for low-frequency ion kinetic physics with $\omega \sim \Omega_i$ and $k\rho_i \sim 1$ [79]. Given that the peak ion number density in the plasma sheet is on the order of 0.33 N_0 and $d_i = \sqrt{\frac{N_0}{N_i}} d_{i0}$, the lowest ion inertial length in the magnetotail is around $0.17\ R_E$ in the simulation. Therefore, the grid size, $(\Delta x, \Delta y, \Delta z) = (0.15, 0.15, 0.15)\ R_E$ is small enough to resolve the ion kinetic physics .

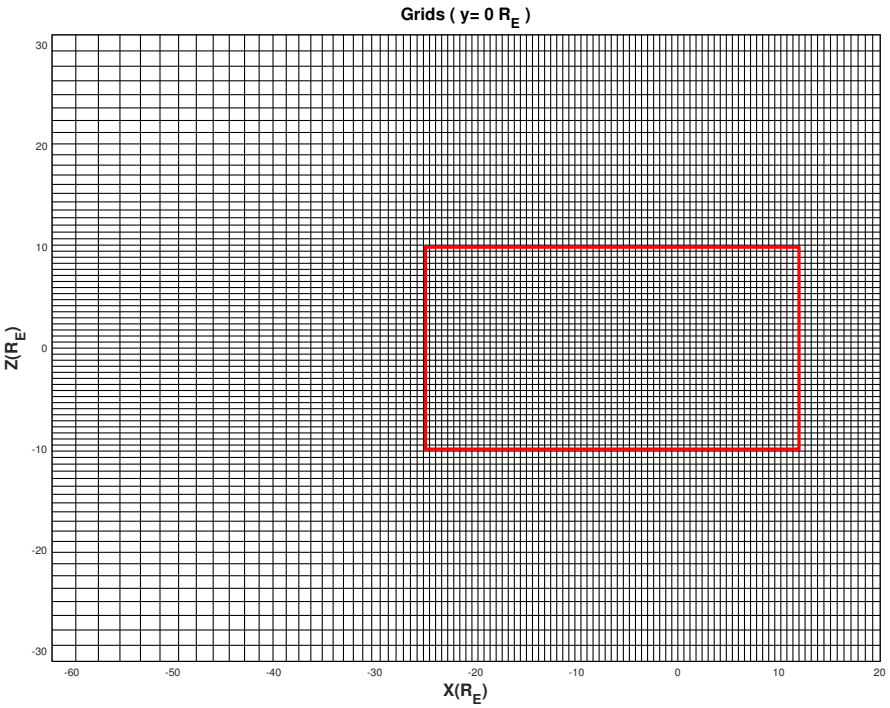

Figure 3.1: Configuration of the nonuniform grid used in the simulation. The red rectangle denotes the uniform region with grid size: $(\Delta x, \Delta y, \Delta z) = (0.15, 0.15, 0.15)\ R_E$.

Table 3.1: Units of parameters

L	t	B	N	E	J	T	V	S
$\mathrm{R_E}$	s	nT	$\mathrm{cm^{-3}}$	$\mathrm{V/m}$	$\mathrm{nA/m^2}$	eV	km/s	$\mathrm{W/m^2}$

It is necessary to scale the kinetic effects in order to compare with typical values in the magnetosphere [126, 78, 79], since an artificial solar wind ion inertial length is adopted given the finite computing resources. The timescale presented in the simulation is increased by a factor of 6.76 in order to compare with typical values in the magnetosphere. The factor is chosen because the artificial solar wind ion inertial length ($0.1\ R_E$) used in the simulation is 6.76 times as large as the realistic one ($0.0148\ R_E$) for a typical solar wind density of 6 $\mathrm{cm^{-3}}$. Thus, the convection speed is faster in the simulation since the positions of the bow shock and magnetopause are assumed to be realistic.

In the presentation that follows as shown in Table 3.1, the spatial length (L) is in units of $\mathrm{R_E}$ and the time (t) in units of seconds (s). The magnetic field (B) is in units of nT and the temperature (T) in units of eV. The electric field (E) is in units of $\mathrm{V/m}$ and the current density (J) in units of $\mu\mathrm{A/m^2}$. The velocity (V) is in $\mathrm{km/s}$ and the Poynting flux (S) in units of $\mathrm{W/m^2}$. The ion number density (N) is in units of $\mathrm{cm^{-3}}$ as scaled to the realistic ion inertial length.

3.2 Global View

The results of the simulation described in this chapter have the following input parameters: IMF components $B_{x0} = B_{y0} = 0$, and $B_{z0} = -10$ nT, Alfvén Mach number $M_A = 7.87$, ion density $N_0 = 6\ \mathrm{cm^{-3}}$, convection speed $V_0 = 700\ \mathrm{km/s}$, ion temperature $T_{i0} = 10$ eV, and electron-to-ion temperature ratio $T_{e0}/T_{i0} = 2$ in the solar wind. Runs with various Mach numbers are also conducted, and the generation of fast flows and Alfvén waves are found to be similar for $M_A = 4 - 8$, although their strengths vary. The electron-to-ion temperature ratio in the solar wind is set to 2 so that the ratio in the plasma sheet is realistic. This is necessary because electrons are assumed to be isothermal for simplicity in this simulation and thus not to be heated in the magnetosheath as under the realistic condition.

Figure 3.2 shows a time sequence of global views of the magnetic field and ion density in the GSM equator along with typical magnetic field lines. The sequence begins approximately 4 minutes after the magnetotail forms in the simulation and spans a period of approximately 3 minutes. The black cones show the ion bulk flow velocity. Open field lines are marked as blue lines while closed field lines are marked as orange lines. The red lines are dipole magnetic field lines and the black lines are reconnected magnetic field lines due to the dayside magnetic reconnection at the magnetopause. The initial condition of magnetic field was set as a dipole magnetic field plus mirror dipole magnetic field for $x < 15\ R_E$ at $t = 0$ s and the uniform solar wind and IMF occupy the region of $x > 15\ R_E$. Initially, the ion particle density is $0.05N_0$ in the region of dipole magnetic field. As time proceeds, the magnetosphere forms self-consistently while the solar wind continuously enters the domain and interacts with the dipole magnetic field. The standoff distances of the magnetopause and bow shock are around $8\ R_E$ and $12\ R_E$, respectively, as shown in Figure 3.2a. Magnetic reconnection occurs at the dayside magnetopause around $x = 8\ R_E$ along X lines through the subsolar point and another in the nightside plasma sheet which extends from $x = -35\ R_E$ to $x = -15\ R_E$. Flux ropes, i.e., twisted magnetic field lines, as a signature of magnetic reconnection are shown both at the dayside magnetopause and in the tail plasma sheet. They are marked in Figure 3.2a as the black field lines at the magnetopause around $x = 8\ R_E$ and as the violet field lines in the magnetotail plasma sheet around $x = -25\ R_E$. Significant variations of magnetic field strength and ion number density at the equator in both the magnetotail and magnetosheath are shown in the left and right-hand columns respectively as indicated by the color bars at the bottom of the figure.

The near-tail X line initially developed at $x \approx -25\ R_E$. In Figure 3.2a, two typical flux ropes marked as 'A' (closed field lines on both sides) and 'B' (one side is open and the other side is closed) are generated by magnetic reconnection at $t = 2391$ s. As shown in the expanded views pointed to by the white arrows, flux rope 'A' has both ends of the field line extending sunward (earthward), while flux rope 'B' has one end going sunward and the other end extending tailward. At this time flux rope 'A' near $x = -22.0\ R_E$, $y = -6.0\ R_E$ is moving with earthward fast flows at a speed of a few hundred kilometers per second generated by reconnection, while flux rope 'B' near $x = -27.0\ R_E$, $y = 7.5\ R_E$ is moving tailward.

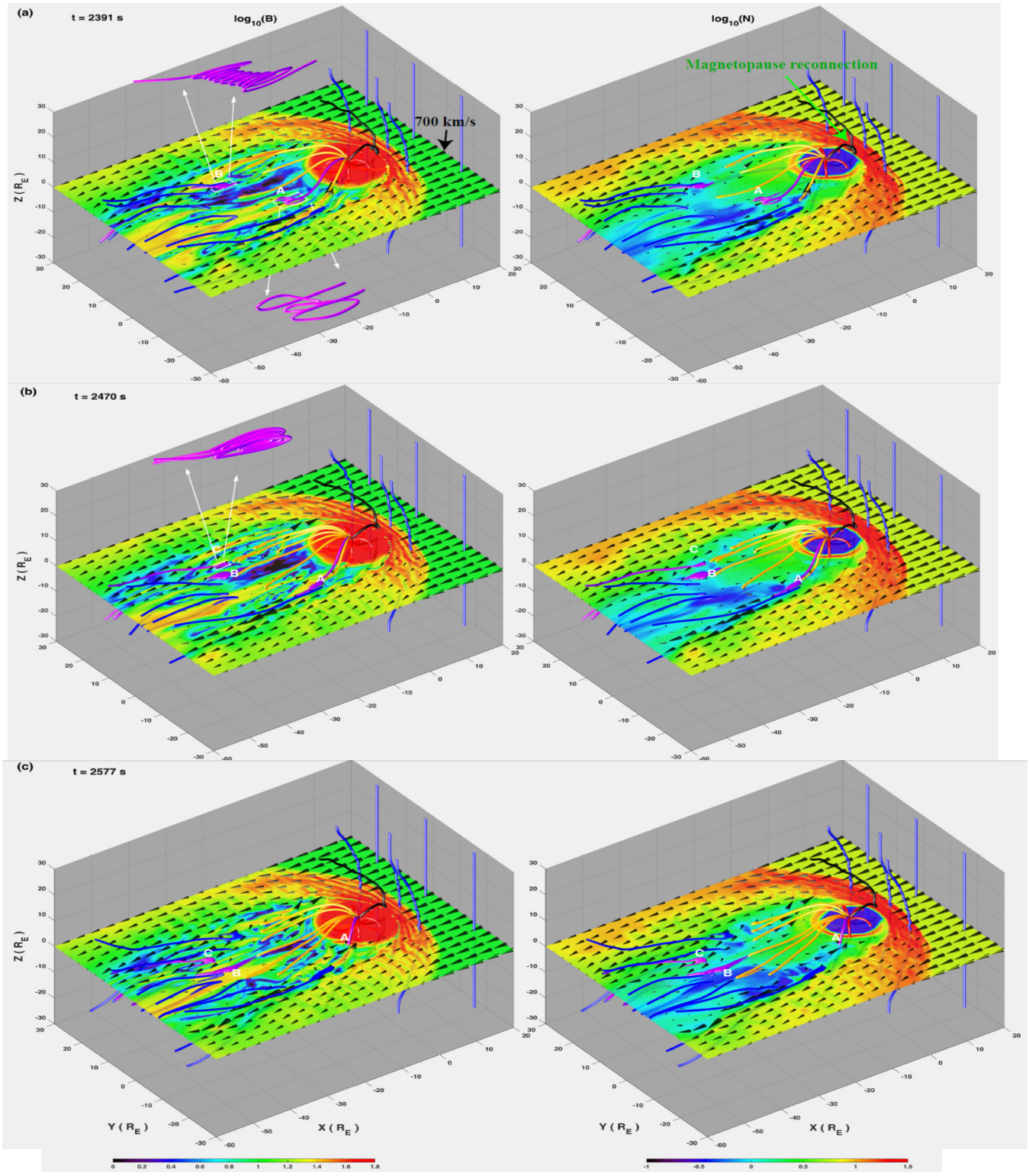

Figure 3.2: Time variation of contours of B (left column) and N (right column) at the equatorial plane with typical magnetic field lines showing the dayside and night side magnetosphere, with multiple flux ropes in the plasma sheet. The black cones denote ion bulk flow velocity.

The two flux ropes also drifted dawnward as shown in Figure 3.2b as the result of $\mathbf{E} \times \mathbf{B}$ drift associated with Hall electric field [79, 85], which cannot be described by MHD models.

A little more than 1 minute later, flux rope 'A' has drifted sunward and dawnward to $x = -14.5\ R_E$, $y = -9.0\ R_E$, and flux rope 'B' has drifted antisunward (tailward) and dawnward to $x = -31.0\ R_E$, $y = 4.0\ R_E$. A new flux rope with both ends of the field line extending antisunward, marked as 'C' is generated at $t = 2470$ s. About one and a half minutes later, as shown in Figure 3.2c, flux rope 'B' has continued its eastward drift and moved from the dusk side to the dawn side. By this time, flux rope 'A' has arrived at the dipole-like field region, where it releases its helicity and merges with the dipole-like magnetic field lines. Once it is deeper in the magnetosphere, it is expected to drift to the dusk side due to the magnetic gradient and curvature drift [79].

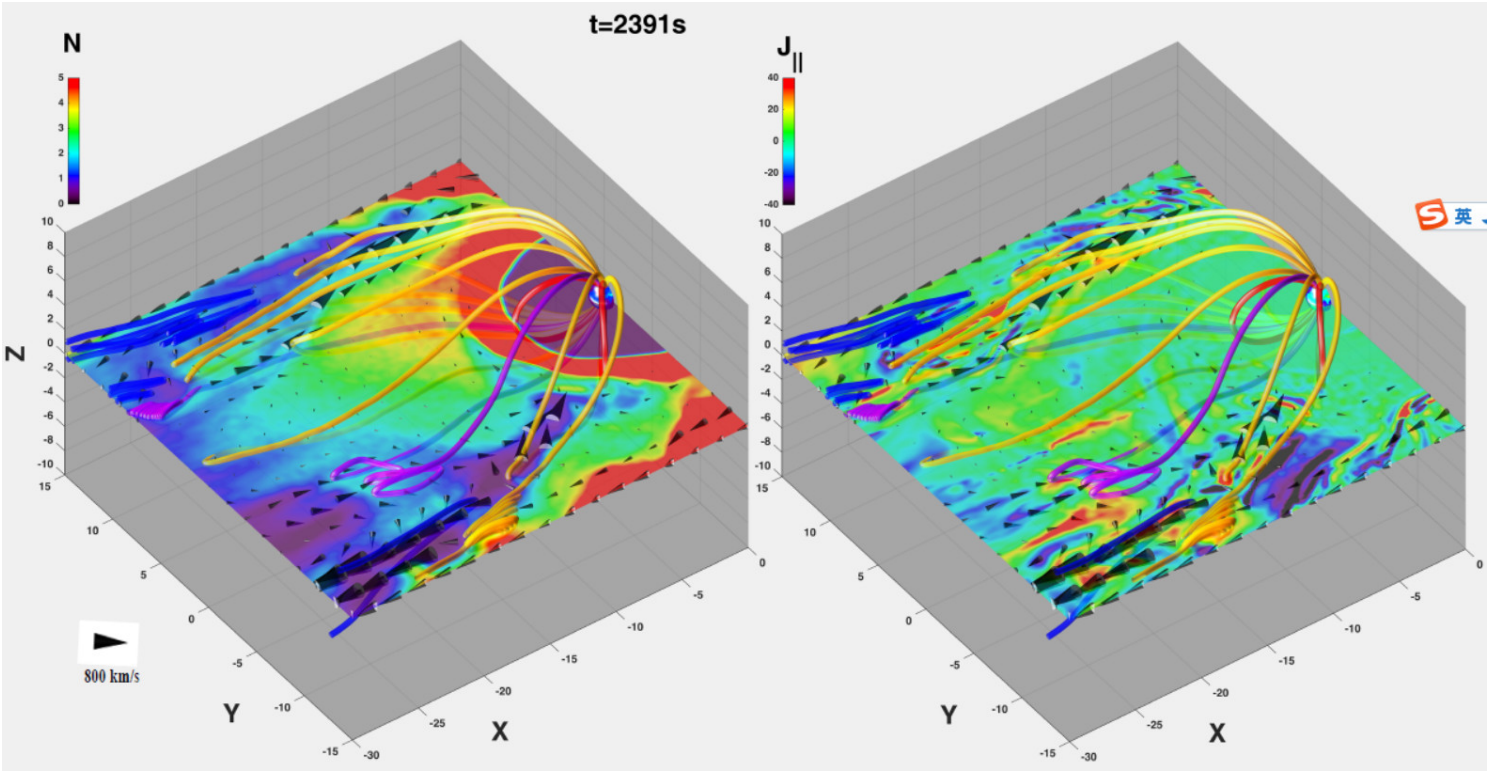

Figure 3.3: Contours of N and $J_{\|}$ at the equatorial plane with typical magnetic field lines and fast flows at $t = 2469$ s. The black cones denote ion bulk flow velocity.

In order to resolve the small structures in the near-Earth magnetotail, Figure 3.3 provides zoom-in contours of the ion number density (N) and parallel current density ($J_{\|}$) in the equatorial plane from $x = 0\ R_E$ to $x = -30\ R_E$ at the same time as in Figure 3.2a. Earthward fast flows (i.e., bursty bulk flows) and tailward fast flow channels with speeds of $300\ \mathrm{km/s} - 1000\ \mathrm{km/s}$ marked as large black cones are found from $x = -30\ R_E$ to

$x = -10\ R_E$, sunward and antisunward of the near-tail X line around $x = -25\ R_E$, respectively. Enhanced ion density is present inside the flux ropes, which move with the fast flows earthward and tailward. On the earthward side, at the flow braking region at $r \sim 10\ R_E$ in front of the strong dipole-like field, the earthward fast flows slow down and convect bidirectionally to the dayside magnetosphere.

During a substorm, many waves are generated by reconnection, including shear Alfvén waves [122, 77, 57, 21]. In our simulation, near the X line on both the dawn and dusk side around $x = -20\ R_E$, many small structures of ion number density and parallel current density are shown in the equatorial plane. These kinds of structures are developed on an Alfvén time scale. Since Alfvén waves are a possible carrier of field-aligned currents, we will examine the shear Alfvénic characteristics around the reconnection regions. Note that if these are Alfvén waves, then they are likely to be kinetic Alfvén waves because typical MHD Alfvén waves do not have ion density perturbations. This will be confirmed in Section 3.3. We will show more information is revealed when the structures of field-aligned current are viewed in the xz plane. Since the xz planes in general show the geometry of the DC magnetic field, the propagation of Alfvén waves can be traced globally from the tail to ionosphere at different local times.

3.3 KAWs in the Magnetotail

Figure 3.4 shows the time evolution of an X line and contours of parallel current density ($J_\parallel$), parallel electric field ($E_\parallel$), transverse magnetic field (B_y), and parallel Poynting flux ($S_\parallel$) in the xz plane at $y = 8.0\ R_E$, where reconnection occurs on the dusk side in Figure 3.3. This time evolution begins about one and one-half minutes before the times shown in Figure 2a and ends about one minute before the times shown in Figure 3.2c. At $t = 2291$ s, near-Earth magnetic reconnection is found with an X line evident from the configuration of the magnetic field lines at $x = -29\ R_E$ in Figure 3.4a. A little more than one and a half minutes later, the X line moves a little earthward, located at $x = -27\ R_E$ at $t = 2391$ s. Subsequently the X line moves a little tailward to $x = -28\ R_E$ at $t = 2448$ s, and further to $x = -21\ R_E$ at $t = 2527$ s. The pink circles show the time evolution of the same wave structure generated by reconnection and its propagation to the Earth along magnetic field lines in the plasma sheet

boundary layer. The consistent correlation of B_y in Figure 3.4b, $J_\parallel$ in Figure 3.4c, $E_\parallel$ in Figure 3.4d, and $S_\parallel$ in Figure 3.4e shows these waves have properties of KAWs. The waves have a large perpendicular wave number in the perpendicular direction (roughly z-direction). The highly field-aligned extension of these structures indicate $k_\parallel \ll k_\perp$. The finite parallel Poynting flux inside the pink circle above the equator has the opposite sign compared with that below the equator in Figure 3.4e. Considering the direction of the local magnetic field lines, the wave structure propagates towards the ionosphere both above and below the equatorial plane. The consistent sign indicates that wave power is absorbed as the wave propagates towards the ionosphere. At the initial time in this sequence, i.e., $t = 2291$ s, the wave front at $z = 0.15\ R_E$ is near $x = -25\ R_E$. About $100\ s$ later, the wavefront at $z = 0.15\ R_E$ arrives at $x = -17\ R_E$. Approximately one minute later, at $t = 2448$ s, the earthward KAWs arrive in the dipole-like field region and then propagate toward the northern and southern ionosphere along the field lines. This is shown by the enhancement of the values of $J_\parallel$, $E_\parallel$ and B_y at $t = 2527$ s. Note that the background B_y component is much smaller than the transverse perturbation of magnetic field while $x < -12\ R_E$. So the propagation of KAW structure is nearly in the plane $y = 8.0\ R_E$. In $x > -12\ R_E$, the background B_y component cannot be ignored, and the propagation of KAW structure is no longer only in the plane $y = 8.0\ R_E$. Meantime, a new wave structure arises around $x = -22\ R_E$ at $t = 2527$ s. The above time scale for the wave propagation is consistent with the Alfvén wave speed, which will be illustrated below.

Figure 3.5 shows the propagation of KAWs from the magnetotail to the ionosphere in 3-D view, where the red patch, the white patch and the blue patch mark the same KAW structure at different times. At $t = 2362$ s, the highly 3-D structure of KAWs characterized by isosurface of $J_\parallel$ marked as the red patch is generated near X lines on the dusk side. The structure propagates to the Earth along the magnetic field line and arrives at the dipole-like field region. As time evolves, the structure merges with the Region-1 current on the duskside and propagates to the ionosphere at $t = 2572$ s.

In order to further confirm that these waves are KAWs, Figure 3.6 examines the shear Alfvén polarization relation and Walén relation along the blue line segment (at $x = -15\ R_E$) marked in the B_y contours in Figure 3.4 for $t = 2391$ s and $y = 8.0\ R_E$. Figure 3.6a shows

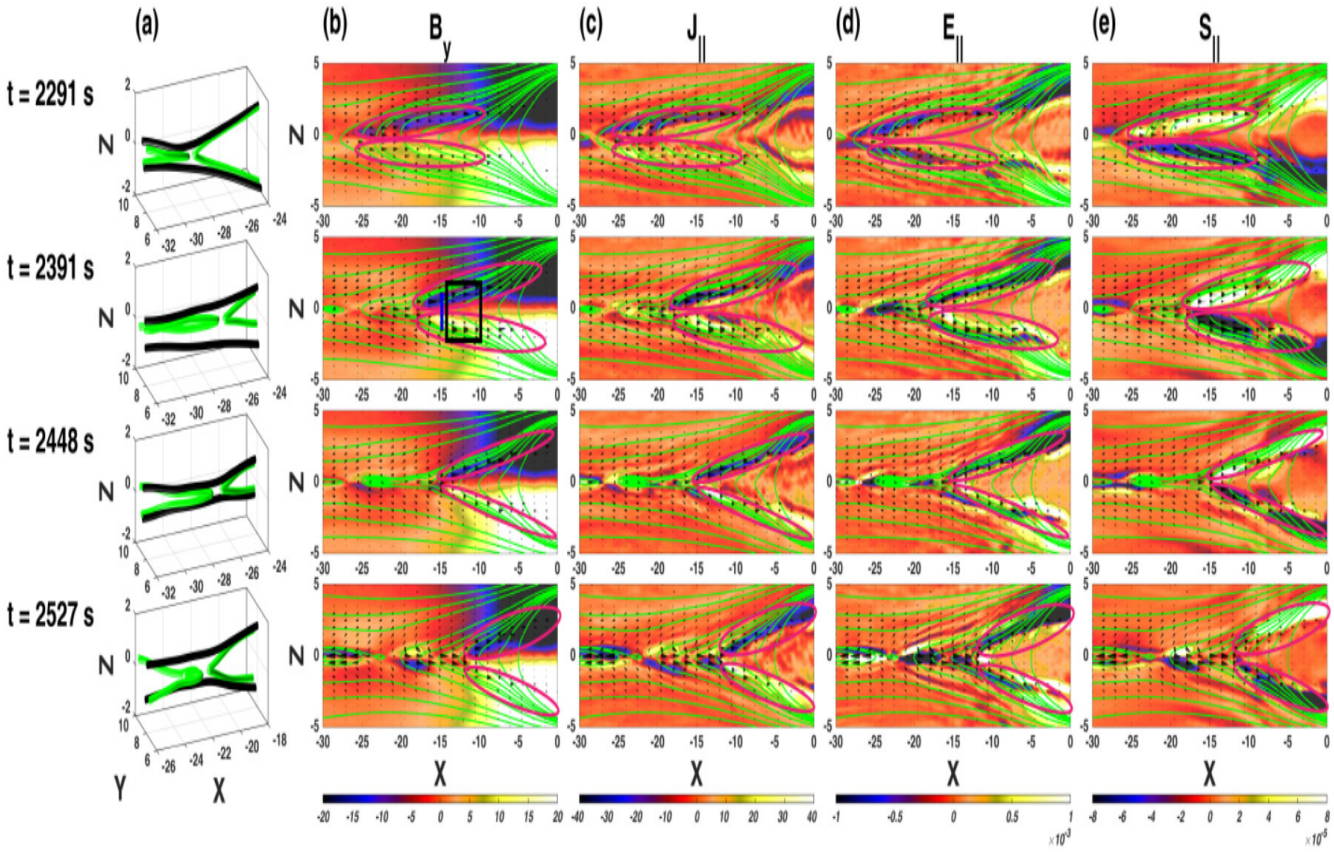

Figure 3.4: (a) Magnetic field line configuration and contours of (b) transverse magnetic field (B_y), (c) parallel current density ($J_\parallel$), (d) parallel electric field ($E_\parallel$) and (e) parallel Poynting flux ($S_\parallel$) at $t = 2291$ s, $t = 2391$ s, $t = 2448$ s and $t = 2527$ s with typical magnetic field fines and ion flow velocity (black arrows) in the plane $y = 8.0\ R_E$.

the spectrum of $J_\parallel$ in k_x-k_z space, from $x = -15.0\ R_E$ to $-10.0\ R_E$ and from $z = -2.0\ R_E$ to $2.0\ R_E$ at $y = 8.0\ R_E$ marked as the black rectangle in Figure 3.4b. $\mathbf{k}'$ is defined as $\mathbf{k}/2\pi$. Since the background magnetic field is almost in the x direction, with $B \sim B_x$, and the wave number is mainly in the z direction, with $k \sim k_z$ ($k_\perp \gg k_\parallel$) as shown in Figure 3.6a, the electric field polarization $\delta E_\perp$ and magnetic field polarization $\delta B_\perp$ associated with KAWs are predominantly B_y and E_z, respectively. In Figure 3.6a, k'_z is $0.2 - 0.6/R_E$ and $k_z = 2\pi k'_z \sim 1.3 - 3.8\ \mathrm{rad/R_E}$. The local ion gyroradius is found to be $\rho_i \sim 0.2\ R_E - 0.4\ R_E$. The perpendicular wave number is thus $k_\perp \rho_i \sim k_z \rho_i \sim 0.4 - 1.1$ in these waves. Figure 3.6b and 3.6c show polarization relation and Walén relation, respectively. The shear Alfvénic transverse components $\delta E_\perp$ and $\delta B_\perp$ in Figure 3.6b are well correlated, with $\delta E_\perp = -1.17 \delta B_\perp V_{Ay}$ in $z > 0$ and $\delta E_\perp = 1.09 \delta B_\perp V_{Ay}$ in $z < 0$. The ratio of $\delta E_\perp / \delta B_\perp$ has different signs in $z > 0$ and $z < 0$ due to the relative direction of $k_\parallel$. Based on equation (1.12), the theoretically

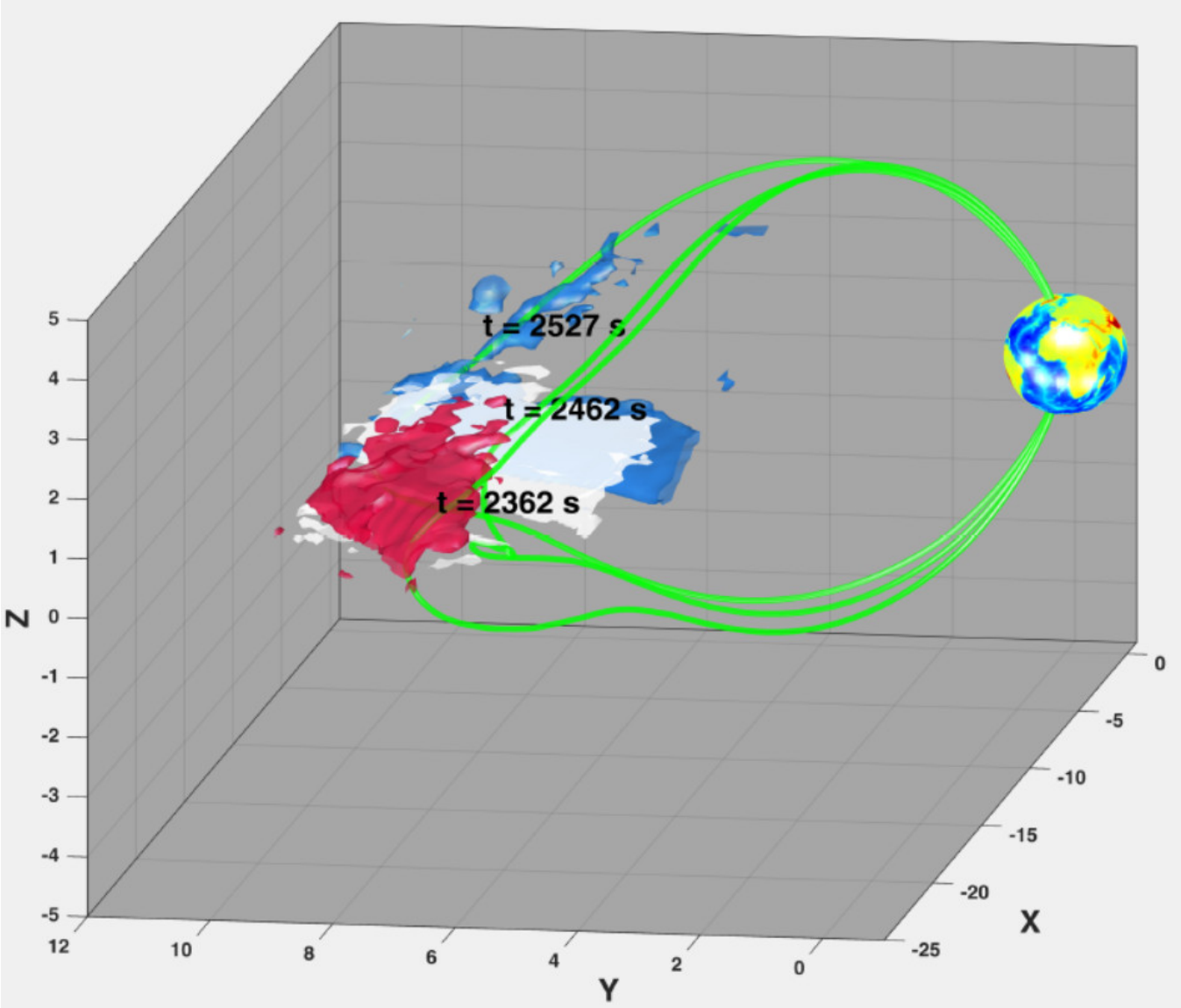

Figure 3.5: Isosurface plots of $J_{\parallel} = -25$ at $t = 2362$ s (red patch), $t = 2462$ s (white patch) and $t = 2572$ s (blue patch) with typical magnetic field lines (green lines) showing the evolution of the same KAW structure generated around $x = -23\ R_E$.

predicted ratio between the perturbation of magnetic field and electric field is $|\delta E_{\perp}/\delta B_{\perp}| \simeq 1.07V_A - 1.44V_A$. The simulation result is consistent with the theoretical polarization relation (see equation (1.12)) of KAWs propagating along (opposite) to the magnetic field on the north (south) side of the plasma sheet, similar to the satellite observations [36, 124] with a super-Alfvénic velocity. Furthermore, it is seen from Figure 3.6c that $\delta V_{iy} = -0.74\delta V_{Ay}$ in $z > 0$ and $\delta V_{iy} = 0.62\delta V_{Ay}$ in $z < 0$. Note that $\frac{T_e}{T_i} \ll 1$. Based on the Walén relation, equation (1.16), the theoretically predicted relation between the perturbation of velocity and magnetic field is $\delta V_{iy} \approx 0.27 - 0.77\delta V_{Ay}$. Therefore, the fit line in Figure 3.6c based on the simulation data is

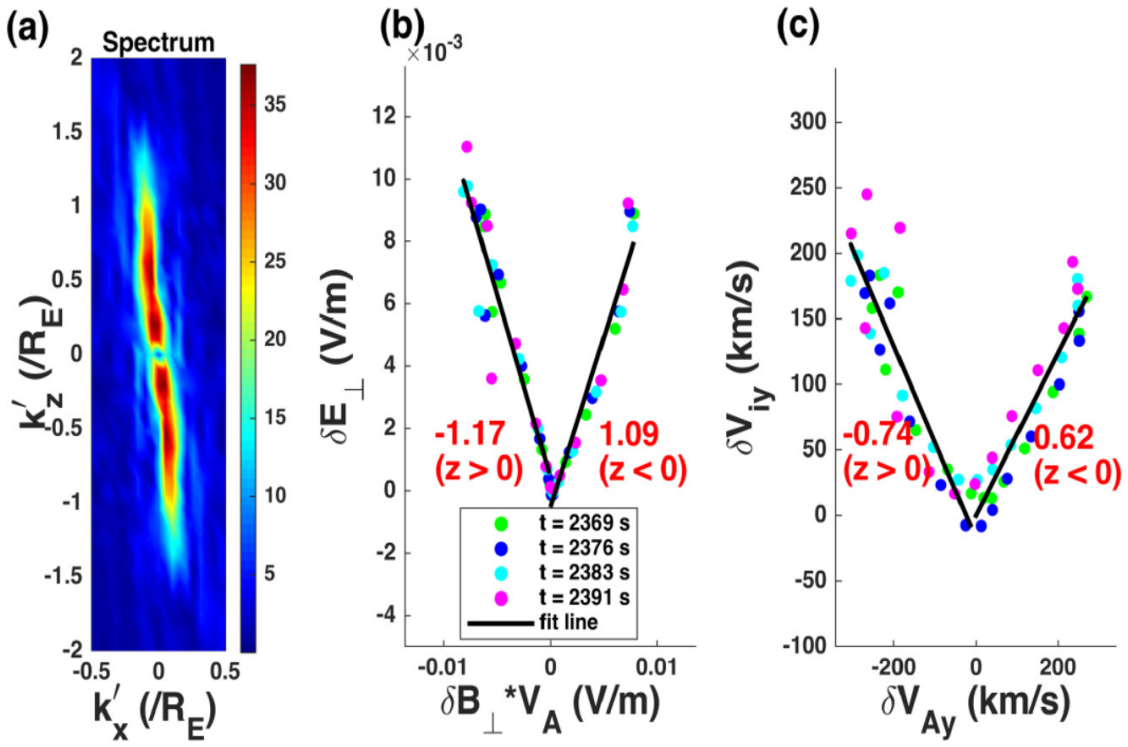

Figure 3.6: (a) Polarization relation and (b) Walén relation: The corresponding $\delta E_\perp$ vs $\delta B_\perp$ and δV_{iy} vs δV_{Ay} both from $t = 2369$ s to $t = 2391$ s along the blue line segment marked in the contour of B_y in the plane $y = 8.0\ R_E$ in Figure 3.4b, where $\delta V_{Ay} = \delta B_y/\sqrt{\mu_0 \rho}$. The solid black lines show the fitted values based on the simulation data. (c) Spectrum of $J_\parallel$ in k_x-k_z space, from $x = -15.0\ R_E$ to $-10.0\ R_E$ and from $z = -2.0\ R_E$ to $2.0\ R_E$ at $y = 8.0\ R_E$ marked as the black rectangle in Figure 3.4b.

also consistent with the theory. In a word, the polarization relation and Walén relation, together with the existence of finite $J_\parallel$ and$E_\parallel$ (Figure 3.4), are consistent with KAWs with $k_\parallel \ll k_\perp$ and $k_\perp \rho_i \sim 1$.

Figure 3.7 shows transverse electric field power spectral density $\delta E_\perp^2(\omega)$, where $\delta E_\perp^2(\omega) = \frac{1}{TL_xL_y} \int\int \delta E_\perp^2(\omega, k_x, k_y) \mathrm{d}k_x \mathrm{d}k_y$ with $\delta E_\perp(\omega, k_x, k_y)$ being the 3-D FFT of $\delta E_\perp(x, y, t)$, from $x = -40.0\ R_E$ to $-10.0\ R_E$ and from $y = -10.0\ R_E$ to $10.0\ R_E$ at $z = 0.45\ R_E$ from $t = 2362$ s to $t = 3094$ s, where T is the time interval, L_x and L_y are the length in x and y direction, respectively. A spectral break in the vicinity of $\omega \sim \Omega_i$ indicates the onset of dissipation, the energy sink at cross-scale coupling in the turbulence spectrum. At the dissipation region ($\omega > \Omega_i$), magnetic energy is coupled to thermal motions of ions. Such a turbulent spectrum is consistent with various satellite observations [73, 17].

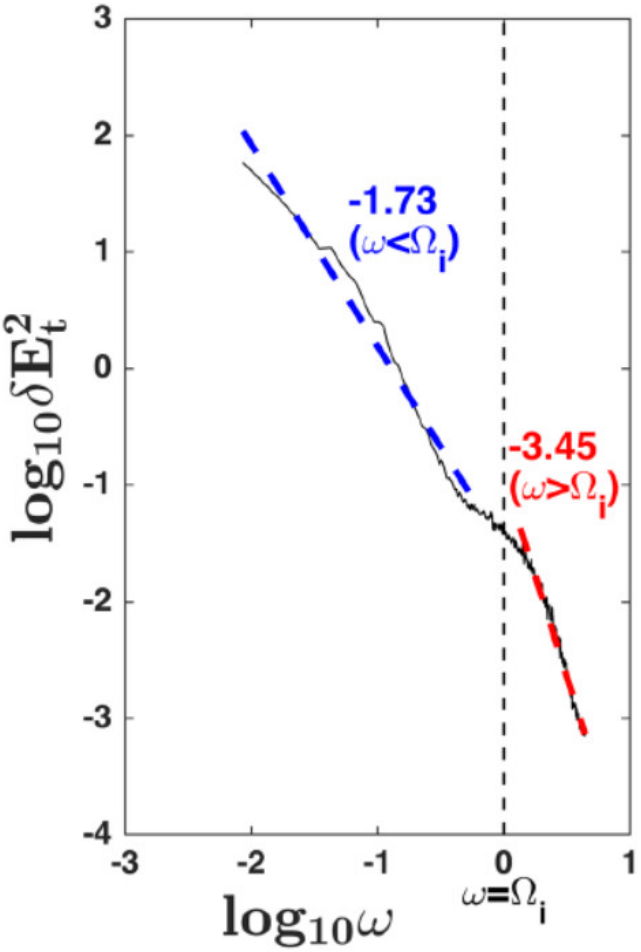

Figure 3.7: Spectrum of transverse electric energy density from t = 2362 s to t =3094 s. The blue dash line and red dash line are the fit power laws in inertial range ($f^{-5/3}$) and dissipation range ($f^{-10/3}$), respectively.

Virtual satellite observations of various parameters at a fixed position $(x, y, z) = (-15, 8, 0.6)\ R_E$ above the equator are shown in Figure 3.8. The gray patch marks the time interval when a KAW structure passes from $t = 2290$ s to 2505 s. Before $t = 2290$ s, the value of magnetic field (B) and ion number density (N) are about 15 nT and 2.0 $/\mathrm{cm}^3$ in Figure 3.8a, denoting the virtual satellite is in the plasma sheet. From $t = 2290$ s to 2505 s, the magnetic field increases and ion density decreases, indicating this position is located in the PSBL between the plasma sheet and the northern tail lobe. After $t = 2505$ s. the satellite is located in the lobe with a very low ion number density and a very high Alfvén speed V_A. In the PSBL from $t = 2290$ s to 2505 s, the magnetic field perturbation is in B_x and B_y in Figure 3.8b, while the electric field perturbation is predominantly in E_z in Figure 3.8c. The perturbation of ion flow velocity (V_{iy} and V_{ix}) in Figure 3.8d is in the same order and negative sign with δV_{Ay}, satisfying the Walén

relation of field-aligned-propagating KAWs. Meantime, field-aligned electric field ($E_\parallel$) and current density ($J_\parallel$) are well correlated in Figure 3.8e. All these features show that KAWs pass by this position in the plasma sheet boundary layer from $t = 2290$ s to 2505 s in the PSBL. KAWs have been observed by Stawarz et al. (2017) [124] based on an MMS event at $9\mathrm{R_E}$ in the plasma sheet, which may be associated with the BBF braking region and/or the magnetic reconnection separatrix. Similar to the MMS observation, the perturbation in magnetic field is a few tens of nT and that in the flow speed is a few hundreds of $\mathrm{km/s}$ in our simulation results shown in Figure 3.8. The perturbation of electric field in our simulation is around $10\mathrm{mV/m}$, which is one order smaller than that in the observation event, in which the local Alfvén speed is about one order larger than that in our simulation. Note that $E_\parallel/E_\perp$ in our simulation is larger than that predicted by linear theory [75]. There is an obvious increase of parallel ion temperature and relatively smaller increase of perpendicular ion temperature in Figure 3.8f. Note that the increase of ion temperature may not all come from ion heating. The temperature anisotropy with $T_\parallel > T_\perp$ is consistent with the result described by Liang et al. (2017) [76]. Liang et al. (2017) [76] presented the parallel and perpendicular heating of the accelerated ions beam by KAWs occurred simultaneously with $T_\perp > T_\parallel$ in the earlier stage, while the overall temperature anisotropy with $T_\parallel > T_\perp$ develop in the later stage due to the increase of the fraction of the accelerated ions and the interaction between the accelerated beam and the core population.

Figure 3.9 shows the time sequence of δB_y as a function of x from $t = 2362$ s to $t = 2577$ s along $z = 0.75\ R_E$ at $y = 7.5\ R_E$. The wave propagation speed of the KAWs can be measured by tracking the propagation of the wave front as indicated by the red line. The phase speed of KAWs is nearly along the magnetic field, which is nearly along the x direction, and their group velocity is along the magnetic field. The phase speed is estimated from the slope of the red line as $343\ \mathrm{km/s}$ in the simulation frame. Note that the background convection speed is very small and can be ignored, and the ion flow is nearly perpendicular to the background magnetic field. Thus, the phase speed of the wave is larger than the local Alfvén speed of $\sim 290\ \mathrm{km/s}$, consistent with the feature of KAWs with $k_\perp \rho_i \sim 0.6$.

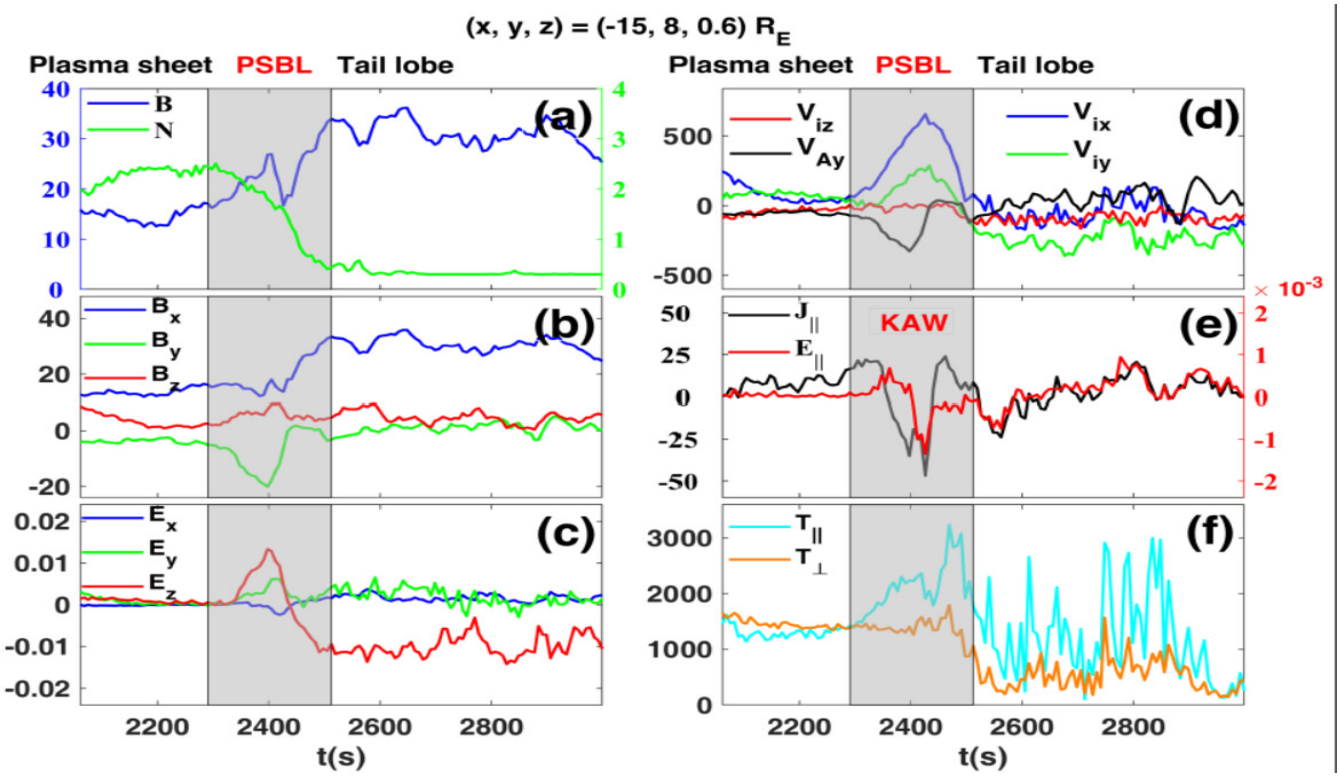

Figure 3.8: Time variation of (a) magnetic field, ion density, (b) x, y, z components of magnetic filed, (c) x, y, z components of electric filed, (d) ion flow velocity, (e) field-aligned electric field and current density, (f) parallel and perpendicular temperature from $t = 2061$ s s to $t = 3000$ s at the position$(x, y, z) = (-15, 8, 0.6)\ R_E$. The gray patch marks the time interval when a KAW passes from $t = 2290$ s to $t = 2512$ s .

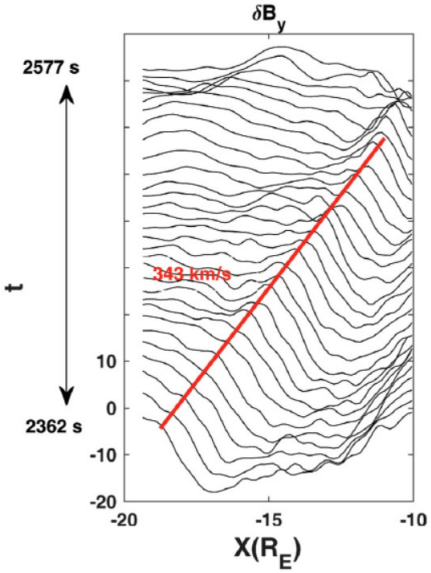

Figure 3.9: The time sequence of the spatial cuts of of δB_y from $t = 2362$ s to $t = 2577$ s along $z = 0.75\ R_E$ at $y = 7.5\ R_E$ from $x = -19\ R_E$ to $-10\ R_E$.

3.4 KAWs in the Flow-braking Region

As the shear Alfvén waves generated in the tail plasma sheet encounter the strong dipole-like field in the flow braking region, their wave power is found to be altered. Take flux ropes (also

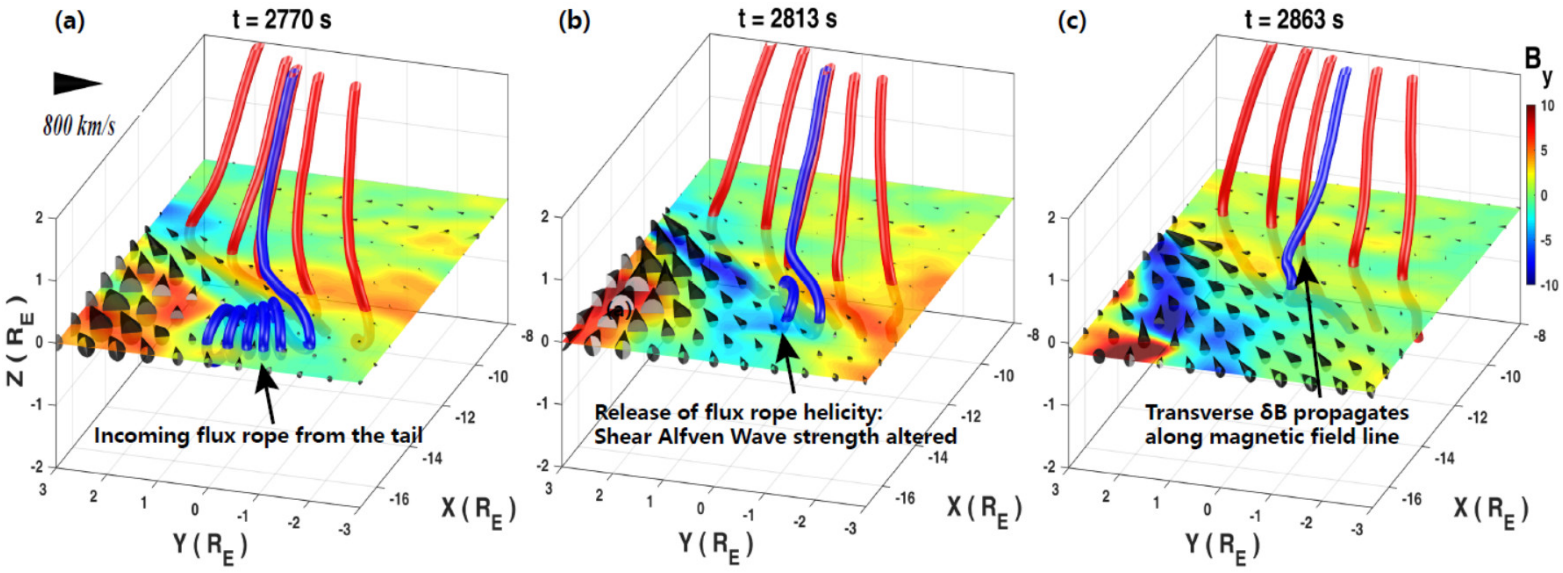

Figure 3.10: Contours of B_y at (a) $t = 2770$ s , (b) $t = 2813$ s in the plane $z = 0\ R_E$ and (c) $t = 2863$ s in the plane $z = -0.3\ R_E$ (the center of plasma sheet is not always in the equatorial plane) with typical magnetic field lines.

carrying shear Alfvénic magnetic field perturbations) as an example. At $t = 2770$ s, the flux rope from the magnetotail as shown in blue in Figure 3.10a arrives at $x = -15\ R_E$, carried by a fast flow. Due to the flow braking, sheared flow is present in the azimuthal direction, as marked as black cones (see Figure 3.10a) which causes perturbations in the dawn-dusk component of the magnetic field. While shear flow alone can generate shear Alfvén waves [35, 34, 138], in our case the flow shear is found to alter the incoming flux rope helicity at the flow shear interface. At the dipole-like field region around the equator at $t = 2813$ s, the flux rope around $x = -12\ R_E$ releases its helicity (see Figure 3.10b). This process alters the strength of shear Alfvén waves which can be distinguished by the change of B_y structure. Finally, the helicity of the flux rope is fully released at $t = 2863$ s, and the perturbation of transverse magnetic field propagates away from the equatorial plane along magnetic field lines (see Figure 3.10c).

In addition, ion inertial effects are found to lead to the generation of additional KAWs at the boundary between the tail-like and dipole-like field, as illustrated in Figure 3.11. Besides the KAW structure highlighted by black rectangles (shown for the midnight-meridian plane and the plane $z = 0.5\ R_E$) in Figure 3.11a propagating from the magnetotail, new KAWs marked as white rectangles in Figure 3.11a are generated at the inner edge of the flow braking region in front of the dipole-like field. This is due to ion inertial effects. Figure 3.11b and Figure 3.11c

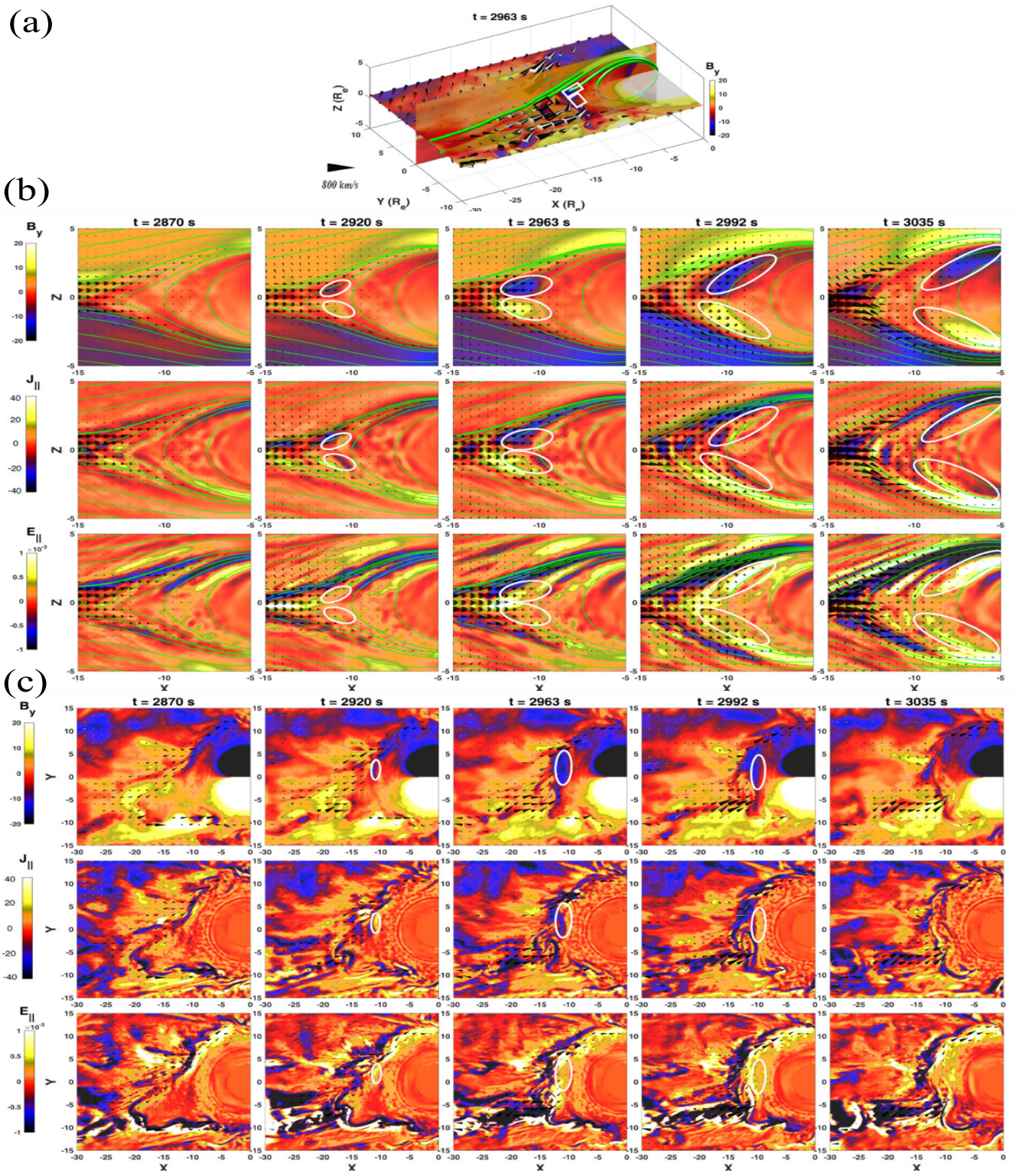

Figure 3.11: (a) Contours of B_y in the equatorial and noon-meridian plane at $t = 2963$ s; Time variation of contours of transverse magnetic filed (B_y) and parallel current density ($J_{\|}$), parallel electric field ($E_{\|}$) in the plane (b) $y = 0\ R_E$ and (c) $z = 0.5\ R_E$ in a time sequence of $t = 2870$ s, $t = 2920$ s, $t = 2963$ s and $t = 3035$ s.

shows the generation and propagation of the new KAWs in the midnight-meridian plane and the plane $z = 0.5\ R_E$, respectively. The black arrows in these figures show the flow vectors. At $t = 2870$ s, there is no signature of KAWs in the near-Earth region of $x > -11\ R_E$, and a close examination of the flow vectors shows that fast flows have also not arrived there yet. This is because magnetotail reconnection is firstly initiated on the dawnside and duskside close to the equatorial magnetopause, not in the midnight region. It is developed in the midnight region at a later time. Nevertheless, at $t = 2920$ s in Figure 3.11b and Figure 3.11c, fast flows due to reconnection have arrived at $x \simeq -11\ R_E$ in this midnight region, and there are well correlated structures in B_y, $J_\parallel$ and $E_\parallel$ (marked as the white circles), exhibiting the features of KAWs similar to Figure 3.4. In this region, charge separation occurs because of the larger inertia of ions than electrons. Ions penetrate deeper into the magnetosphere before being stopped by the strong magnetic field. As a result, a pair of parallel currents appear, as previously found by Swift et al. (2001) [127] based on a 2-D global hybrid simulation. The wave power increases at $t = 2963$ s. Then, the waves propagate to the high latitudes along magnetic field lines. At $t = 3035$ s, the waves have gone further away from the equatorial plane and cannot be shown in the plane of $z = 0.5\ R_E$. A global diploarization is also seen over the time period from $t = 2870$ s to $t = 3035$ s, which causes the expansion of the dipole-like geomagnetic field region. Figure 3.11c shows the corresponding structures in the plane $z = 0.5\ R_E$. The localized structures highlighted by the white circles in Figure 3.11c are the near-equatorial counterparts of these new KAWs. These waves are identified as KAWs in the same manner as the waves in the magnetotail (see Figure 3.6).

Figure 3.12 shows the polarization relation and Walén relation along the green line marked in the contour plot of $J_\parallel$ in Figure 3.12b. $\delta E_\perp$ and $\delta B_\perp$ in Figure 3.12a are also well correlated, with $\delta E_\perp = -1.46\delta B_\perp V_{Ay}$ in $z > 0$ and $\delta E_\perp = 1.27\delta B_\perp V_{Ay}$ in $z < 0$. The ratio of $\delta E_\perp/\delta B_\perp$ in $z > 0$ and $z < 0$ has different signs due to the opposite direction of $k_\parallel$. The perpendicular wave number $k_\perp \rho_i \sim 0.2 - 1.1$ in these waves. The polarization relation in Figure 3.12a is consistent with the theoretically predicted ratio with $|\delta E_\perp/\delta B_\perp| \simeq 1.02V_A - 1.48V_A$ based on equation (1.12). Based on equation (1.16), the theoretically predicted relation between the perturbation of velocity and magnetic field is $\delta V_{iy} \approx 0.27 - 0.93\delta V_{Ay}$. The Walén relation in

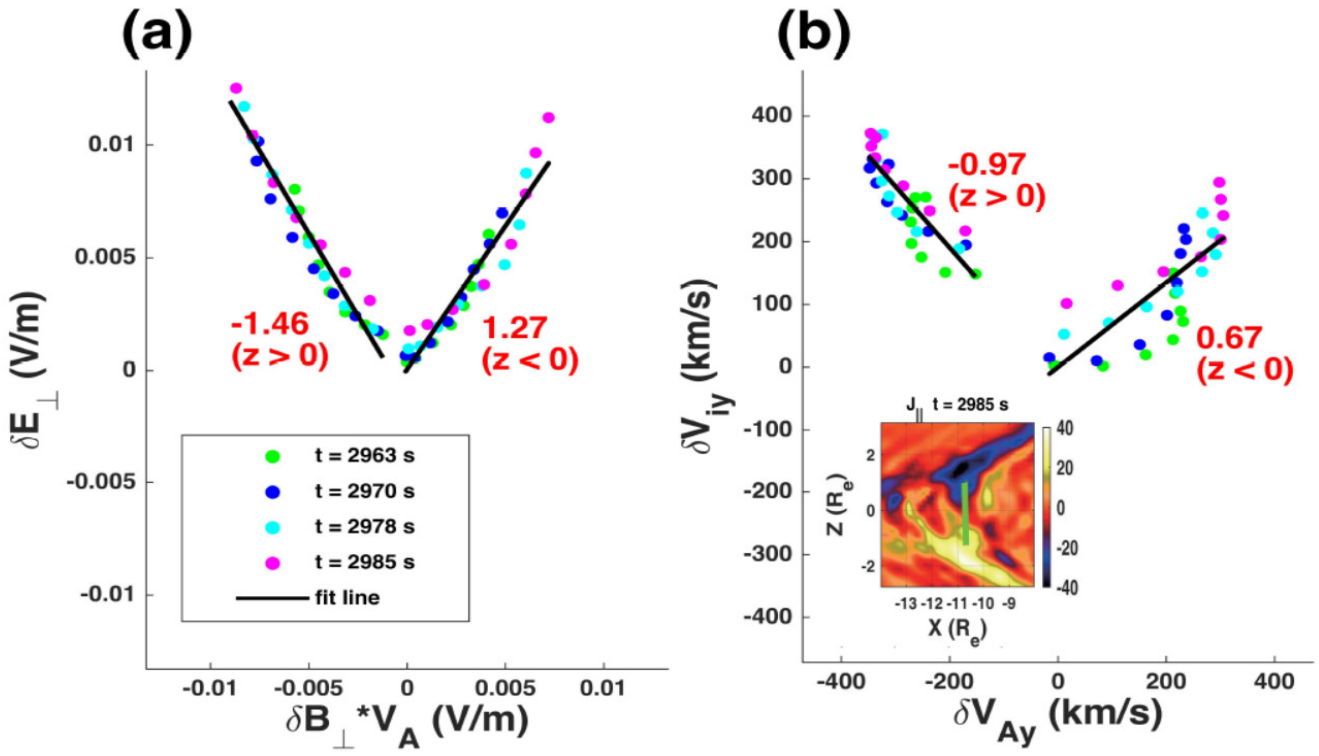

Figure 3.12: (a) Polarization relation and (b) Walén relation: The corresponding $\delta E_\perp$ vs $\delta B_\perp$ and δV_{iy} vs δV_{Ay} both from $t = 2963$ s to $t = 2985$ s along the green line segment marked in the contour of $J_\parallel$ in Figure 3.12b in the plane $y = 0\ R_E$. The solid black lines show the fitted values based on the simulation data.

Figure 3.12b with $\delta V_{iy} = -0.97\delta V_{Ay}$ in $z > 0$ and $\delta V_{iy} = 0.67\delta V_{Ay}$ in $z < 0$ is also consistent with theory.

Figure 3.13 presents the time variations of the same quantities as shown in Figure 3.8 at $(x, y, z) = (-11.1, 0.5, 0.6)\ R_E$ in the flow-braking region. Before $t = 2870$ s, B_x is dominant, $B_z \ll B_x$, and thus the magnetic field line is more stretched (see Figure 3.13b). The flow velocity is very small, as seen from Figure 3.13d, indicating there is no fast flow yet at this near-midnight location. The shaded region from $t = 2870$ s to $t = 3034$ s shows one event of KAWs generated around this position. A pulse of B_y is generated during this time interval, as shown in Figure 3.13b. Near the end of the interval, the background B_x decreases while B_z, the field strength B (as shown in Figure 3.13a) and the average ion perpendicular temperature (as shown in Figure 3.13f) also have a sharp increase, indicating that the position is now inside the dipole-like region due to the global dipolarization and the B_y wave pulse is located just at the edge of the dipole-like field region. Unlike the KAWs in the magnetotail,

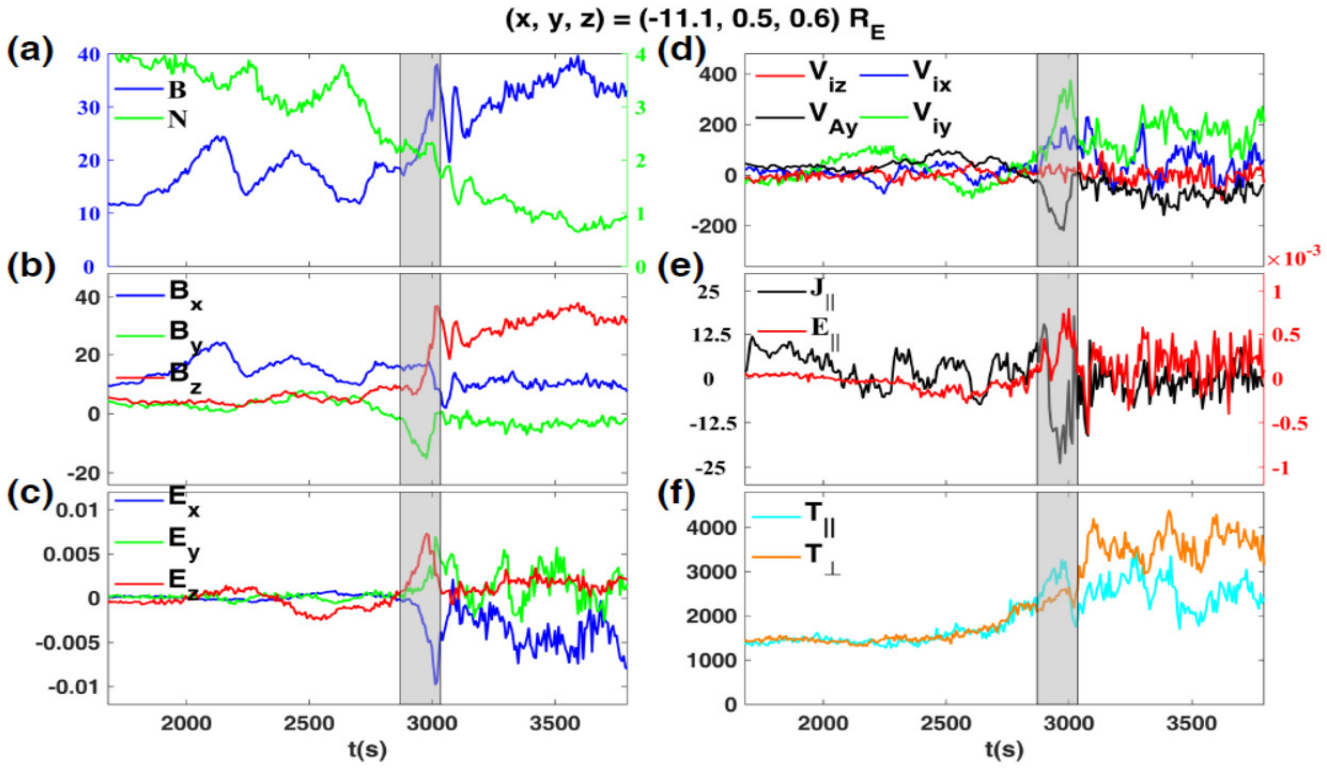

Figure 3.13: Time variation of (a) magnetic field, ion density, (b) x, y, z components of magnetic filed, (c) x, y, z components of electric filed, (d) ion flow velocity, (e) field-aligned electric field and current density, (f) parallel and perpendicular temperature from $t = 1682$ s to $t = 3794$ s at the position $(x, y, z) = (-11.1, 0.5, 0.6)\ R_E$. The shaded region from $t = 2870$ s to $t = 3034$ s shows one event of KAWs generated around this position.

here near the flow braking, V_{ix} from $t = 2870$ s to $t = 3034$ s is very small (see Figure 3.13d). While the perturbation of the magnetic field is mainly in the y-direction, the pulse of electric field perturbation has both E_x and E_z components (see Figure 3.13c) since $k_\perp$ is oblique in the xz plane. Correspondingly, the wave pulse is also seen in V_{iy} and V_{Ay} (Figure 3.13d), $J_\parallel$ and $E_\parallel$ (Figure 3.13e), and both ion temperatures $T_\parallel$ and $T_\perp$ (Figure 3.13f). Note that compressional wave perturbations are also frequently present in the flow braking region. As seen in Figure 3.13, just a few tens of seconds after $t = 3037$ s, a large-amplitude compressional wave pulse is generated, with clear enhancements in B and ion perpendicular temperature. There is an anti-phase correlation between B and N.

3.5 Propagation of Poynting Flux

Since shear Alfvén waves/KAWs generated in the equatorial magnetotail must interact with the transition region between the tail-like and dipole-like fields before they can propagate to

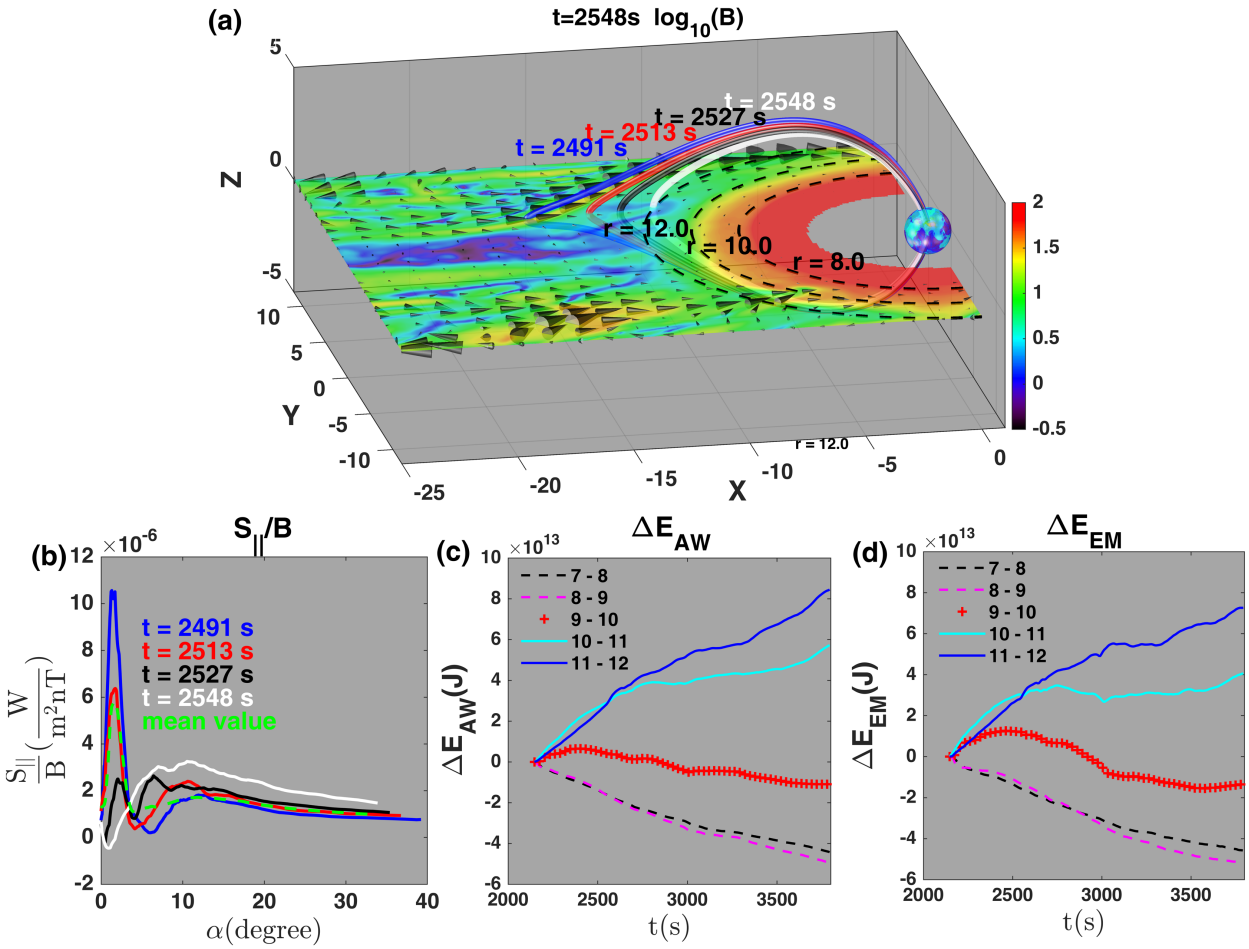

Figure 3.14: (a) Contour of B in the equatorial plane at $t = 2548$ s ; (b) Line plots of $S_{||}/B$ versus α along the magnetic field lines as shown in Figure 3.14a at $t = 2491$ s (blue) $t = 2513$ s (red), $t = 2527$ s (black) and $t = 2548$ s (white), respectively, where $\alpha = 90° - \theta$ with θ being the polar angle; time evolution of (c) Alfvénic wave energy (ΔE_{AW}) and (d) electromagnetic wave energy (ΔE_{EM}) flowing out of the spherical shell over the nightside from $t = 2147$ s to $t = 3794$ s with black dash line from $r = 7.0\ R_E$ to $r = 8.0\ R_E$, magneta dash line from $r = 8.0\ R_E$ to $r = 9.0\ R_E$, red line from $r = 9.0\ R_E$ to $r = 10.0\ R_E$, cyan line from $r = 10.0\ R_E$ to $r = 11.0\ R_E$, blue line from $r = 11.0\ R_E$ to $r = 12.0\ R_E$. Parts of the interface bewteen the surface of the sphere and the equatorial plane are marked as black dash curves in Figure 3.14a

the ionosphere, as discussed above, it is important to understand whether the Poynting flux follows a direct mapping from the plasma sheet to the ionosphere. In the following we estimate how much Alfvénic wave energy can be transmitted across this transition region around $r \sim 10.0\ R_E$. Figure 3.14a shows the contours of B in the equatorial plane at $t = 2548$ s, with ion flow velocity superposed as black arrows. Colored lines in the figure are a magnetic flux tube tracked from $t = 2491$ s to $t = 2548$ s. The transition region between the dipole-like magnetic field region and the tail-like region is around $r = 10.0\ R_E$-$11.0\ R_E$. Note that the dashed lines

in the equatorial plane in Figure 3.14a mark various geocentric distances. The ratio between the parallel Poynting flux and the magnetic field strength, $S_\parallel/B$, along the field line as a function of the latitude α at various times are shown in Figure 3.14b, where $\alpha = 90^\circ - \theta$ with θ being the polar angle. At $t = 2491$ s, the flux tube is stretched tail-like around the equator, going through the plasma sheet. As time proceeds, the flux tube moves earthward. If there were steady driving of Alfven waves and all the wave power in the plasma sheet propagated into the inner magnetosphere along the flux tube, the ratio $S_\parallel/B$ should tend to be nearly a constant, considering that the flux tube cross section area is inversely proportional to B. The results in Figure 3.14b, however, show clearly that not all the wave energy reaches the ionosphere. Overall, the value of $S_\parallel/B$ is quite different between the tail-like part of the field line (near equator, with $\alpha < 10^\circ$) and dipole-like region (higher latitudes). The ratio remains nearly constant only inside the dipole-like field region ($\alpha > 30^\circ$) on the earthward side of the tail-dipole transition region, as seen from Figure 3.14b.

At $t = 2491$ s, $S_\parallel/B$ peaks at $\alpha \simeq 3^\circ$ near the equator where the source of KAW in the tail is, which is outside the transition region, with the peak value $\sim 10.5 \times 10^{-6}$ W/(m^{2}nT). As discussed in Figure 3.10, the structure of KAWs from the tail are then significantly altered by the flow braking region. A dip is seen in the ratio $S_\parallel/B$ at $\alpha \simeq 7^\circ$, and then another much weaker peak appears, associated with the Poynting flux both transimitted from the magnetotail and locally generalized, which only reaches 1.7×10^{-6} W/(m^{2}nT) at $\alpha = 13^\circ$ in Figure 3.14b for $t = 2491$ s. The ratio then decreases from $\alpha = 13^\circ$ to $\alpha = 30^\circ$, which is likely due to ion Laudau damping. The ratio then reaches nearly constant in $\alpha > 30^\circ$.

At $t = 2513$ s, the peak value of $S_\parallel/B$ near the equator has decreased to about 6.2×10^{-6} W/(m^{2}nT) as the tail flux tube moves closer to the Earth and some waves have propagated away from the equator. Again, $S_\parallel/B$ decreases significantly from the tail-like to dipole-like field region. The tail KAWs continue to propagate away at $t = 2527$ s. By $t = 2548$ s, the flux tube has moved to $L \simeq 12\ R_E$ (see the white field line in Figure 3.14a), and the wave energy has spread out over the field line. At later times, part of Shear Alfvén wave/KAW energy is seen to be reflected at the inner boundary, similar to that described in Guo et al. (2015) [50]. Given that the average Alfvén speed along the magnetic field lines is around 1500 km/s, it

takes about $80 - 100$ s for Shear Alfvén waves/KAWs to arrive at the inner boundary and be reflected. The peak values of $S_\parallel/B$ at $\alpha \simeq 3^\circ$ at $t = 2491$ s and $t = 2548$ s are roughly corresponding to the initial and final stage, respectively, of the source Poynting flux associated with a fast flow event outside the transition region. The difference between these two peak values is $\sim 10.5 \times 10^{-6}$ W/(m^{2}nT) as the source Alfvénic energy from the tail propagates away over this time interval. Similarly, the difference between the two peak values at $\alpha \simeq 13^\circ$, $\sim 1.5 \times 10^{-6}$ W/(m^{2}nT), roughly corresponds to the increase of Alfvénic energy in the dipole-like field region as a result of the fast flow event. Such a result indicates that a factor of less than $1.5 \times 10^{-6}/10.5 \times 10^{-6} \sim 1/7$ of the Alfvénic wave energy from the magnetotail goes across the transition region into the dipole-like field region during the fast flow period. After a decreasing of the wave power over α, the values of $S_\parallel/B$ remain nearly constant in α for $\alpha > 30^\circ$ with $S_\parallel/B \sim 1.49 \times 10^{-6}$ W/(m^{2}nT) at $t = 2491$ s and $S_\parallel/B \sim 0.77 \times 10^{-6}$ W/(m^{2}nT) at $t = 2548$ s. As a result, the Poynting flux received in the ionosphere during the period from $t = 2491$ s to $t = 2548$ s can be estimated as $\sim 0.72 \times 10^{-6}$ W/(m^{2}nT). Overall, roughly less than $0.72 \times 10^{-6}/10.5 \times 10^{-6} \sim 1/14$ of the Alfvénic wave energy from the magnetotail fast flow reaches the ionosphere.

Figure 3.14c shows the time evolution of Alfvénic wave energy (ΔE_{AW}) flowing out of the spherical shell over the nightside for different radii, where $\Delta E_{AW}(r_1, r_2, t) = E_{AW}(r_1, t) - E_{AW}(r_2, t)$ with $E_{AW}(r, t)$ being written as,

$$E_{\mathrm{AW}}(r,t) = -\int_{t'=2147}^{t'=t}\int_{\phi=\pi/2}^{\phi=3\pi/2}\int_{\theta=0}^{\theta=\pi} \mathbf{S}_\parallel \cdot \hat{\mathbf{r}}\mathbf{r^2}\sin(\theta)\,\mathrm{d}\theta\,\mathrm{d}\phi\,\mathrm{d}\mathbf{t}', \tag{3.1}$$

with $\hat{\mathbf{r}}$ being the unit vector in the radial direction and (r, θ, ϕ) giving the radial distance, polar angle, and azimuthal angle. From $r = 12.0\ R_E$ to $r = 10.0\ R_E$, the total Alfvénic wave energy is increasing as seen by an over all increasing positive ΔE_{AW} (see the blue and cyan line), which means there are new sources of shear Alfvén wave coming from the tail to the tail-dipole field transition region. Evidence of the decrease of shear Alfvénic wave energy from the magnetotail to the inner magnetosphere can also be seen in Figure 3.14b.

In the dipole-like field region, the wave energy decreases from $r = 9.0\ R_E$ to $r = 7.0\ R_E$ as seen by an over all decreasing negative ΔE_{AW} (see the black and magenta line) in Figure

3.14c. Such a decrease may be due to ion Landau damping. Note that our simulation also shows that shear Alfvén waves/KAWs are present throughout the inner magnetosphere [79]. They may be generated by mode conversion from compressional waves that propagate across the field lines from the tail. Such a process of coupling between the compressional and transverse modes will be investigated elsewhere. The presence of KAWs, including kinetic field-line resonance, in the inner magnetosphere has been observed by Chaston et al. (2014) [23].

The region from $r = 10.0\ R_E$ to $r = 9.0\ R_E$ is not fixed in the tail-dipole field transition region or dipole-like field region. The total Alfvénic wave energy would not be keeping decreasing or increasing (see the red line in Figure 3.14c). For example, the region is located in the tail-dipole field transition region and ΔE_{AW} is increasing from $t = 2147$ s to $t = 2404$ s. From $t = 2404$ s to $t = 2662$ s, the region is located in the dipole-like field region due to the global dipolarization and ΔE_{AW} is decreasing.

To assess the contribution of the new local source and external source to E_{AW}, Figure 3.14d shows the time evolution of electromagnetic wave energy, (ΔE_{EM}), flowing out of the spherical shell over the nightside for different radii. The quantity E_{EM} is calculated in a similar way as E_{AW} by substituting $\mathbf{S}_{\parallel}$ with $\mathbf{S}$. Since mode conversion from compressional wave to Alfvén wave does not change the value of E_{EM}. The increase of E_{EM} is the Alfvénic wave energy totally coming from the local source. Overall, the lines in Figure 3.14d have the same trends with those in Figure 3.14c. However, $\Delta E_{EM}(11, 12, t)$ and $\Delta E_{EM}(10, 11, t)$ at $t = 3794$ s have a value of 7.3×10^{13} J and 4.1×10^{13} J, respectively, smaller than $\Delta E_{AW}(11, 12, t)$ and $\Delta E_{AW}(10, 11, t)$ with a value of 8.5×10^{13} J and 5.7×10^{13} J, respectively. This is because parts of compressional wave energy are converted to Alfvénic wave energy. In a word, the generation of much of the wave energy is local while some of the wave generation is likely due to mode conversion.

The pattern of Parallel Poynting flux carried by Alfvén waves in the ionosphere is obtained by mapping of the inner boundary at $r = 3.5\mathrm{R_E}$ along the geomagnetic field lines to $r = 1.01\mathrm{R_E}$ as shown in Figure 3.15a. The contour of parallel Poynting flux is viewed from the south, with the midnight on the bottom, dawn on the right, and the dashed circles marking the geomagnetic latitude (MLAT). The negative parallel Poynting flux with a peak

of -2.0 ergs $\mathrm{cm}^{-2}\mathrm{s}^{-1}(\mathrm{mW/m}^2)$ is centered at $70°$ latitude in the nightside ionosphere and flowing downward. Figure 3.15b shows the ion energy flux, 15 minutes after the substorm onset, from statistical result of DMSP satellites from 1996 to 2007, adapted from Wing et al. (2013) [139]. The overall ion energy flux is centered around $67°$ latitude with a smaller peak of 0.25 ergs $\mathrm{cm}^{-2}\mathrm{s}^{-1}$. The pattern from hybrid simulation result is centered at $3°$ latitude higher than the statistical result with a higher value. That is reasonable because of the fact that the latitude and values are correlated with the solar wind conditions and the hybrid result is obtained from only a single case.

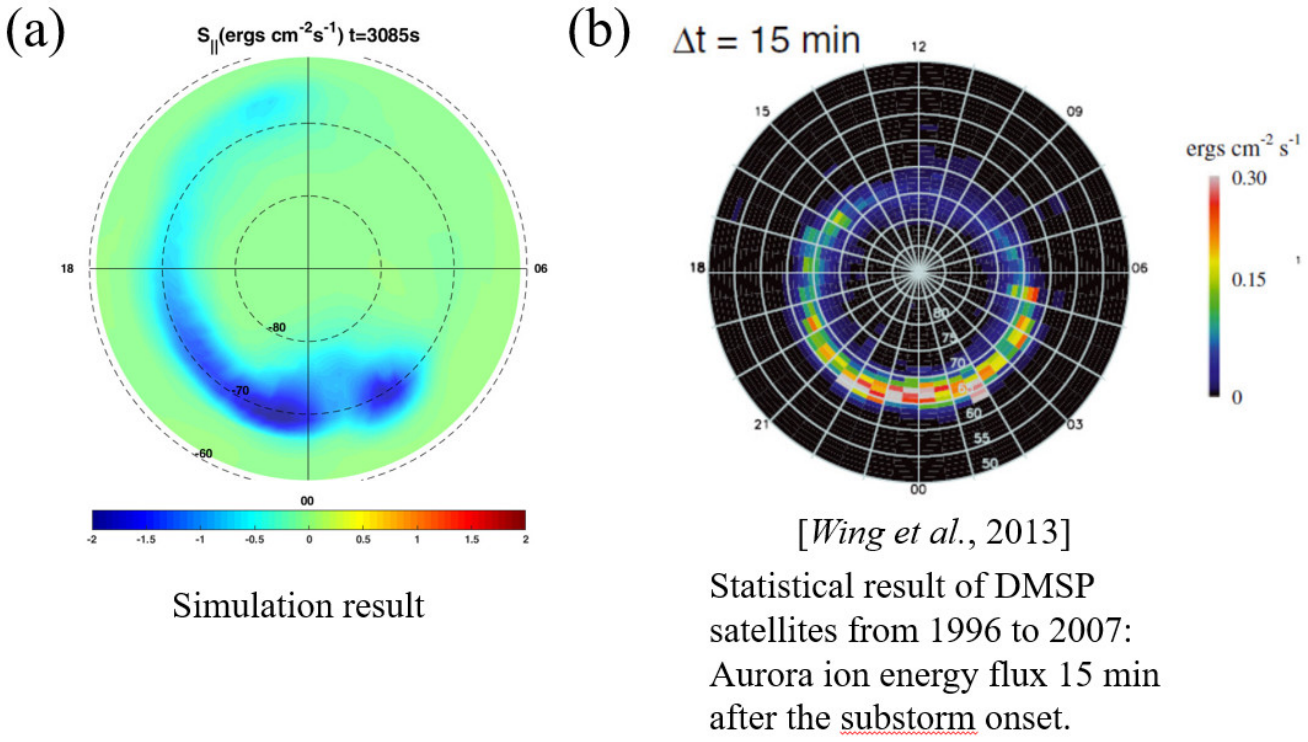

Figure 3.15: Contours of (a) parallel Poynting flux from simulation result at $t = 3085$s and (b) ion energy flux from statistical result of DMSP satellites adapted from Wing et al. (2013) [139], viewed from the south, with the midnight on the bottom, dawn on the right, and the dashed circles marking the geomagnetic latitude (MLAT).

3.6 Ion Acceleration in the Magnetotail

To interpret ion acceleration in the magnetotail, a typical ion is traced as seen in Figure 3.16. The ion is initially at $1.2\mathrm{R_E}$ above the equator on the dawn side near the reconnection region.

Significantly ion acceleration up to $50\mathrm{keV}$ at different locations are seen by the color of the points.

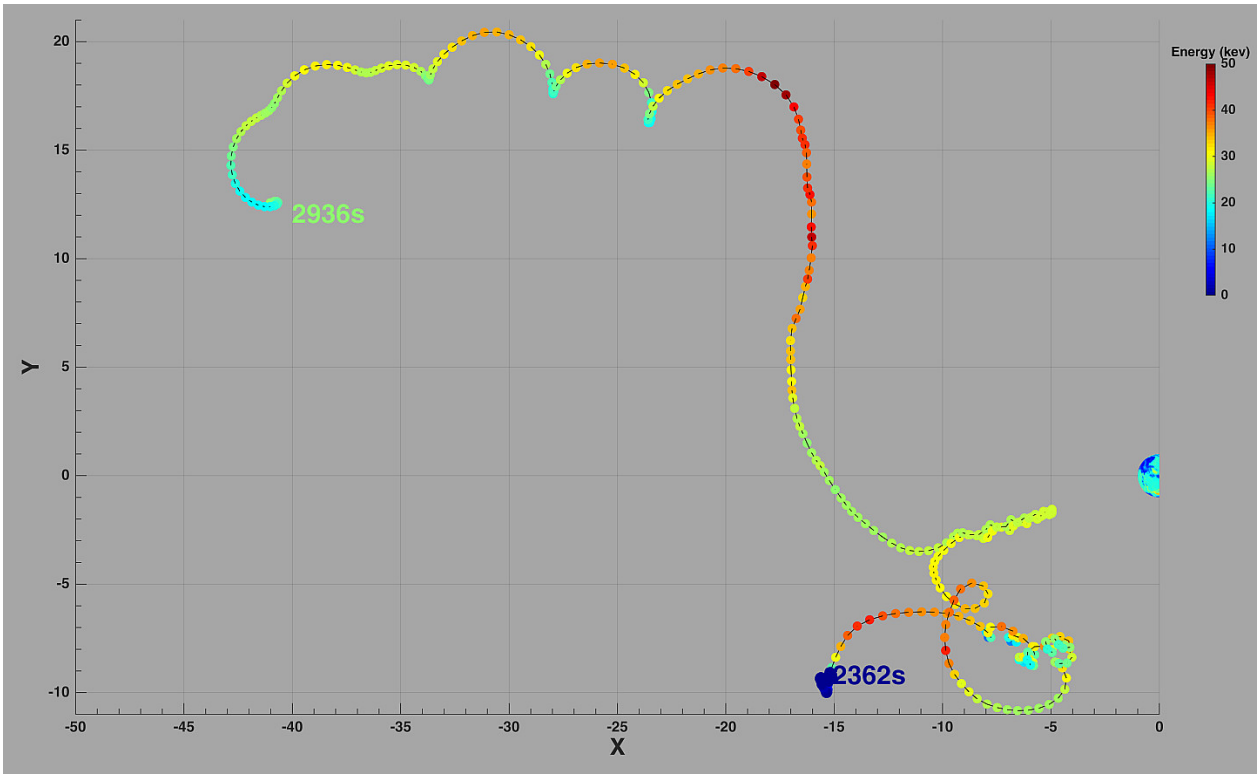

Figure 3.16: Trajectory of a typical ion from $t = 2362\mathrm{s}$ to $t = 2936\mathrm{s}$ is projected on the $x - y$ plane. The colors of the balls show the ion kinetic energy level.

Figure 3.17 show the diagnostics of ion acceleration with details. Line plots are the positions of ions, x and y position in small range, z position in small range, magnetic field strength (B) and ion number density (N), three components of $\mathbf{E}+\mathbf{V_i}\times\mathbf{B}$, total kinetic energy ($KE_{total}$) with parallel component ($KE_{||}$) and perpendicular component ($KE_{\perp}$), first adiabatic invariant (μ), three components of electric field, and $J_{||}$ and $E_{||}$ along the trajectory of the typical ion in Figure 3.16. The gray patches denote the plasma sheet in the magnetotail while the yellow patch marks the plasma sheet near the flow-braking region. At time $t0 = 2380\mathrm{s}$, the ion with kinetic energy $KE_{total} = 0.6\mathrm{keV}$ is at $1.0R_E$ above the equator with $x = -15.1\mathrm{R_E}$ and $y = -9.3\mathrm{R_E}$ on the dawn side near the reconnection region as seen in Figure 3.17b-c and Figure 3.17j. X-line point is around $x = -15.0\mathrm{R_E}$. The ion is initially in the lobe with the high magnetic field strength ($46\mathrm{nT}$) and low ion number density ($0.3\mathrm{cm}^{-3}$) as seen in Figure 3.17d. Then the ion moves toward the plasma sheet, crossing the plasma sheet boundary layer and arriving at the reconnection site at $t1 = 2497\mathrm{s}$ (see Figure 3.17k). Before $t1 = 2497\mathrm{s}$,

three components of $\mathbf{E} + \mathbf{V_i} \times \mathbf{B}$ are very small because the magnetic field line is frozen in the plasma with $\mathbf{E} + \mathbf{V_i} \times \mathbf{B} = \mathbf{0}$ nearly satisfied. At $t1 = 2497\mathrm{s}$, the ion decouples from the magnetic field line as shown by the large values of three components of $\mathbf{E} + \mathbf{V_i} \times \mathbf{B}$. The ion is accelerated to a peak energy of $42.9\mathrm{keV}$. The parallel acceleration up to $2.5\mathrm{keV}$ (see the enhancement of $KE_{||}$ in Figure 3.17f) is seen first in the boundary layer at $t1 = 2497\mathrm{s}$ by KAWs (see the finite value of $J_{||}$ and $E_{||}$). Then, significantly large perpendicular ion acceleration up to $39.5\mathrm{keV}$ at $t = 2518\mathrm{s}$ is seen by the increase of $KE_{\perp}$ in Figure 3.17f. Following that is the perpendicular kinetic energy is transferred to parallel kinetic energy. Meantime, the total kinetic energy is also increasing from $41.4\mathrm{keV}$ at $t = 2518\mathrm{s}$ to around $42.9\mathrm{keV}$ at $t = 2519\mathrm{s}$. That means around $1.5\mathrm{keV}$ of the parallel kinetic energy are from the acceleration of $E_{||}$ within one second. The first adiabatic invariant (magnetic moment $\mu = mv_{\perp}^2/(2B)$) shown in Figure 3.17g is no longer a constant in the plasma sheet. As Liang et al. (2017) [76] presented, an increase in the gyro-averaged magnetic moment causes perpendicular stochastic heating when ion is accelerated. Then the ion is trapped by KAWs as seen by the periodical perturbation of $KE_{\perp}$ from $2525\mathrm{s}$ to $t4 = 2658\mathrm{s}$ correlated with finite $J_{||}$ and $E_{||}$, and strong perturbation of electric field (see Figure 3.17h).

The ion moves earthward with KAWs to the flow-braking region with $(x, y, z) = (-7.8, -7.4, -1.8)\mathrm{R_E}$ at $t2 = 2535\mathrm{s}$ (see Figure 3.17l). The first adiabatic invariant at the flow-braking region is smaller than that of the plasma sheet in the magnetotail. The ion precipitates along field lines into $r = 9\mathrm{R_E}$ at $t = 2597\mathrm{s}$ and then be bounced back to the plasma sheet in the magnetotail at $t3 = 2610\mathrm{s}$. The acceleration of the ion in the magnetotail plasma sheet marked as the second gray patch is quite similar with the first one. The ion is drifted duskward to $y = -2.9\mathrm{R_E}$ owing to the magnetic gradient and curvature drift at $t4 = 2658\mathrm{s}$. From $t4 = 2658\mathrm{s}$ to $t5 = 2716\mathrm{s}$, the ion moves toward the ionosphere and be bounced back to the plasma sheet. Few KAWs are found in this region because the reconnection near midnight is weak during this time interval. The ion is then drifted to the duskside and accelerated by another KAW (see Figure 3.17m). The ion are accelerated from $27\mathrm{keV}$ at $t = 2743\mathrm{s}$ to $40\mathrm{keV}$ at $t6 = 2783\mathrm{s}$ in an average energy level. From $t6 = 2783\mathrm{s}$, the ion number density keeps increasing to $5.7\mathrm{cm}^{-3}$, a higher ion number density than the average value in the plasma sheet. The ion is crossing the low-latitude

boundary layers seen by the contour plot of ion number density (N) in Figure 3.17n. During the crossing, the ion is further accelerated to $53.5\mathrm{keV}$ by the Kelvin–Helmholtz instability at the boundary layer. The acceleration mechanism is not KAW because of the nearly zero value of three components of $\mathbf{E} + \mathbf{V_i} \times \mathbf{B}$ and $E_{||}$. Then the ion moves tailward with the tailward convection flows around the boundary layer.

3.7 Ions Tracing at the Flow-braking Region near Substorm Current Wedge

Ions at the flow braking region on the dawnside near substorm current wedge where fast flows hit the inner magnetosphere are traced. Figure 3.18 shows the projection of the orbits of ions traced from $t = 2362\mathrm{s}$ to $t = 2730\mathrm{s}$ on the equatorial plane. At the initial time, the ions are in the flow braking region as seen from the black cones in the contour plot of ion number density. The red rectangle in Figure 3.18 marks the initial positions of the ions. At $t = 2730\mathrm{s}$, most of the ions drift westward similar as the ions in the ring current. Only around one fourth of particles drift eastward. The interesting fact is the ions drifting eastward are all in a low energy level below around $20\mathrm{keV}$ as seen in Figure 3.18b. That is because the magnetic drift making ions drift westward at the localized position is proportional to ion kinetic energy. $\mathbf{E} \times \mathbf{B}$ drift can either be westward or eastward at the flow-braking region. The ions with low energy level can be drifted eastward if the drift velocity of the localized $\mathbf{E} \times \mathbf{B}$ drift is eastward and large enough to overcome the effect of the magnetic drift.

3.8 Summary

In this chapter, the generation and propagation of KAWs in the magnetotail are studied via a 3-D global hybrid simulation based on ANGIE3D. The main results are:

1. KAWs are generated by the near-tail reconnection, propagating earthward and tailward. As part of the structure of the reconnection, the electromagnetic fluctuations, parallel electric, parallel currents, and parallel Poynting fluxes are carried by KAWs to the ionosphere. These highly 3-D Alfvénic waves with $k_\perp \gg k_\parallel$ are identified by the polarization and dispersion relations of Alfvén modes. The spectral break of the electromagnetic power spectral density shows that ion kinetic physics begins to show up at $\omega \sim \Omega_i$.

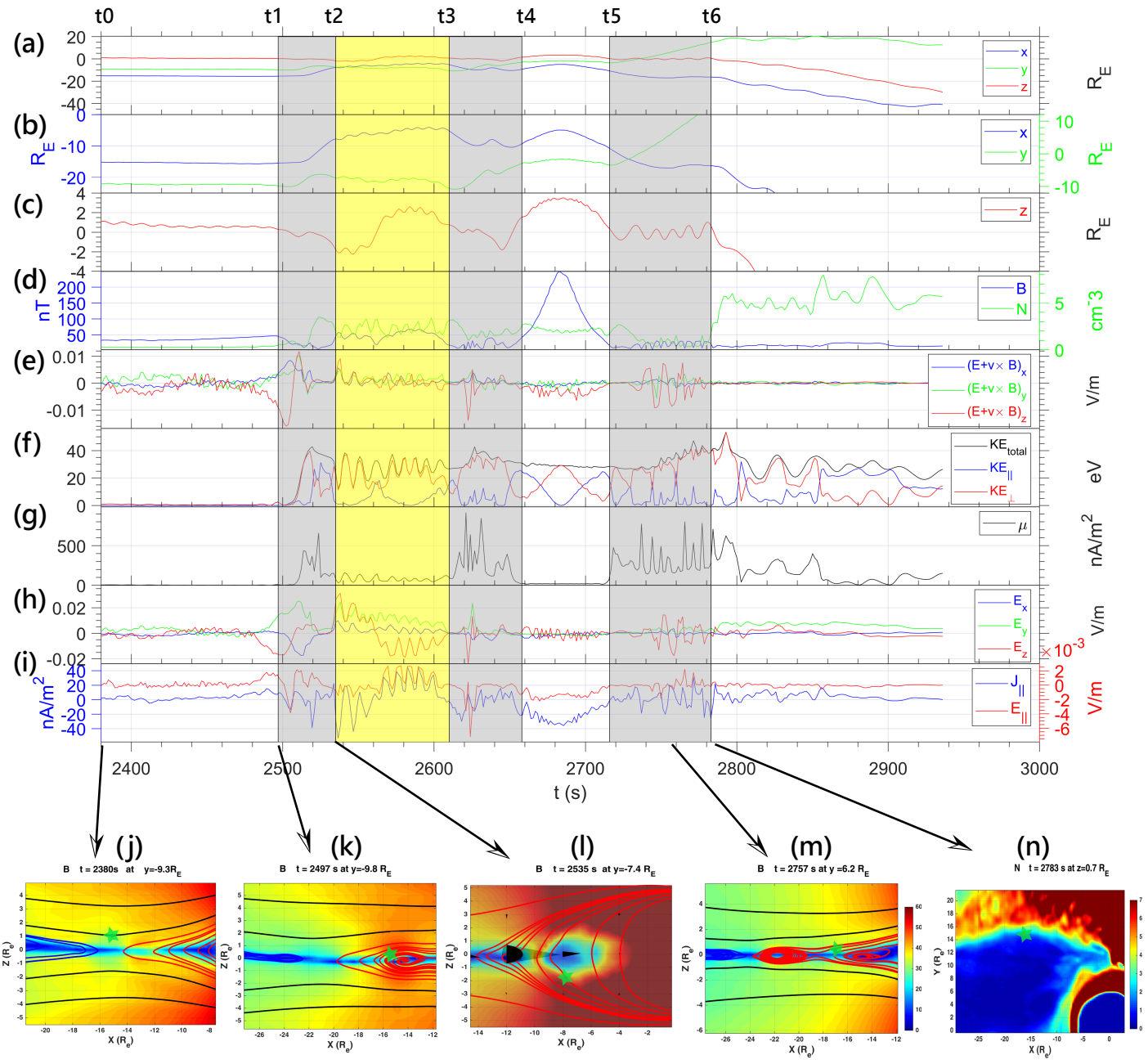

Figure 3.17: Line plots of (a) position, (b) x and y position in small range, (c) z position in small range, (d) magnetic field strength (B) and ion number density (N), (e) three components of $\mathbf{E}+\mathbf{V_i}\times\mathbf{B}$, (f) total kinetic energy (KE_{total}) with parallel component ($KE_{||}$)and perpendicular component ($KE_{\perp}$), (g) first adiabatic invariant (μ), (h) three components of electric field, and (i) $J_{||}$ and $E_{||}$ along the trajectory of the typical ion in Figure 3.16. The gray patches denote the plasma sheet in the magnetotail while the yellow patch marks the plasma sheet near the flow-braking region. Contours of B at (j) 2380s, (k) 2497s, (l) 2535s and (m) 2757s in the $x-z$ plane with typical magnetic field lines; (n) contour of N at 2783s in the $x-y$ plane. Green star denotes the location of the traced ion.

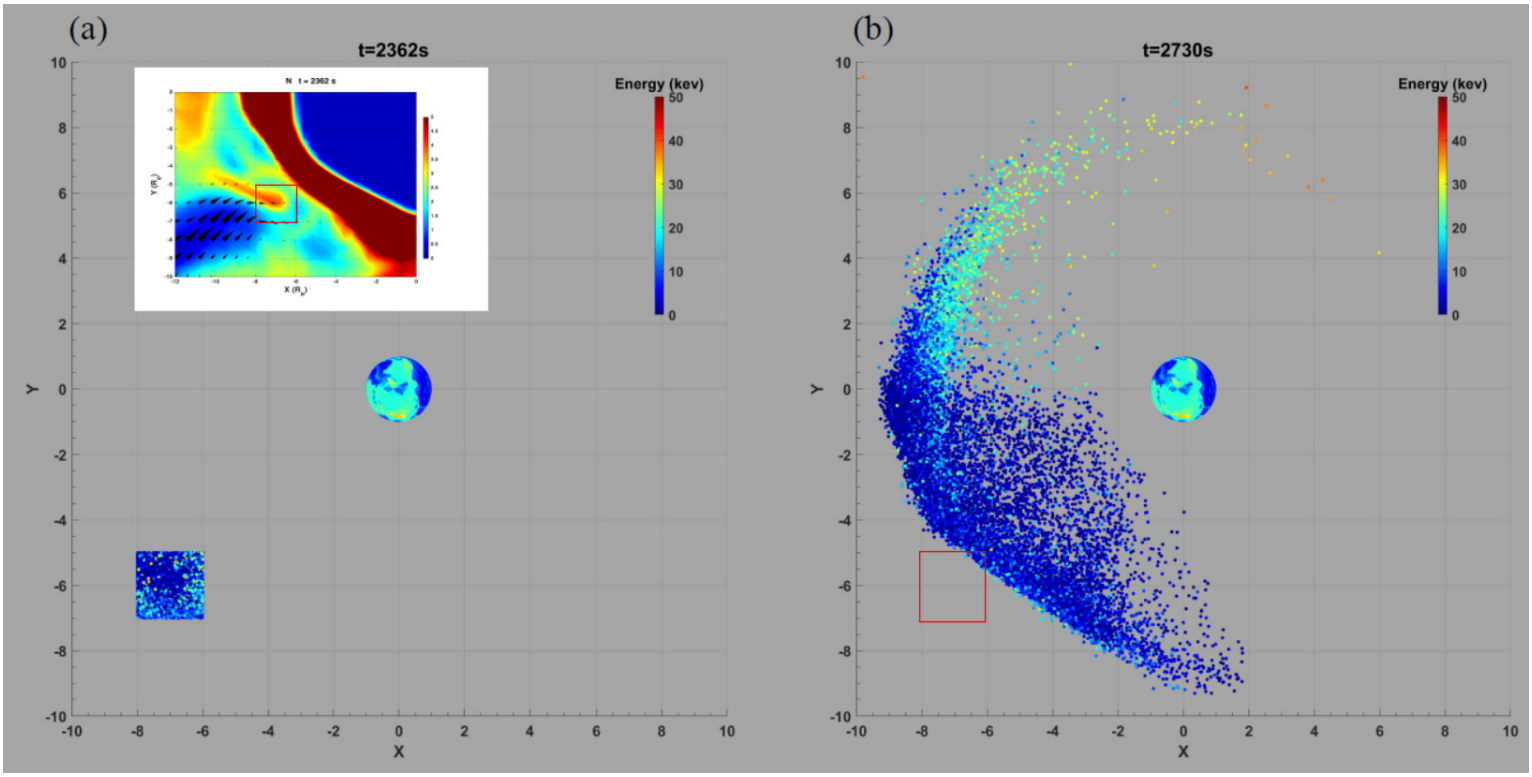

Figure 3.18: Projection on the equatorial plane of the orbits of particles traced from (a) $t = 2362\text{s}$ with contour of ion number density to (b) $t = 2730\text{s}$ at the flow braking region. Red rectangle marks the initial positions of particles.

.

2. As the shear Alfvén waves generated in the tail plasma sheet encounter the strong dipole-like field in the flow braking region, their wave power is found to be altered.

3. KAWs are also generated at the inner edge of flow-braking region in front of the dipole-like field due to the ion inertial effects. Polarization and dispersion relations of these waves are also presented in this chapter.

4. The total Alfvénic wave energy on the nightside is estimated. Roughly less than $1/7$ of Alfvénic wave energy originating from magnetotail reconnection can cross the transition region around $r = 10.0\ R_E \sim 11.0\ R_E$, and less than $1/14$ of the Alfvénic wave energy from the magnetotail reaches the ionosphere. Magnetotail reconnection, local sources at the flow-braking region, and mode conversion are the sources of Alfvénic wave energy of the ionosphere.

5. Overall pattern of ion energy flux is consistent with statistical result of DMSP satellites except the higher latitude and values, indicating the importance of KAWs on the aurora brightening. That is reasonable because of the fact that the latitude and values are correlated with the solar wind conditions and the hybrid result is obtained from only a single case.

6. Ion acceleration in the magnetotail is discussed. The ion is seen accelerated and trapped by KAWs associated with magnetic reconnection and flow braking. Ions are also accelerated when crossing the low-latitude boundary layer. An increased gyro-averaged magnetic moment at the stage of ion acceleration indicates the perpendicular stochastic heating of ions.

7. Most of the ions drift westward due to magnetic drift at the flow braking region near substorm current wedge. Part of the ions at low energy level (below around $20\mathrm{keV}$) are seen to drift eastward when the eastward drift velocity caused by localized $\mathbf{E} \times \mathbf{B}$ drift is larger than the westward drift velocity caused by the magnetic drift.

It should be pointed out that as the wave propagates closer to the ionosphere, they will be in the inertial regime when β is less than the electron-to-ion mass ratio m_e/m_i. Nevertheless, inertial Alfvén waves (IAWs) are not included in the hybrid model, in which electrons are considered as a massless fluid. Electron Landau damping is also ignored in the model.

The parallel electric field is clearly present in the polarization of KAWs, but its magnitude in our simulation appears to be larger than that predicted by the linear theory. The magnetic field perturbations in the KAWs generated in the tail fast flows are of large amplitude (e.g., Figure 3.8), and the waves are localized, embedded in the nonuniform plasma. This introduces uncertainty in the estimate of $E_\parallel$. In our diagnostics, we have calculated $E_\parallel$ by projecting $\mathbf{E}$ to the wavy local magnetic field $\mathbf{B}$.

Overall, our simulation presents a comprehensive picture of the generation and structure of KAWs in the global magnetosphere and their roles in ion acceleration and heating as well as their connection to the ionosphere. The shear Alfvén waves and KAWs are shown to be significant carriers of the parallel currents and Poynting fluxes that are injected to the ionosphere.

Nevertheless, due to the presence of multiple boundary/transition layers in the magnetosphere, the magnitude of Poynting fluxes in the tail KAWs is not simply mapped to the ionosphere.

Chapter 4

Comparison between Hybrid Simulation and Observations from THEMIS and DMSP

The above results are based on hybrid simulation. By correlating the observations with the results of the simulations, we will learn about the physics of the coupling of the tail to the inner magnetosphere and enhance the reliability of our simulation results. Chapter 4 makes a comparison with observations from THEMIS and DMSP. THEMIS spacecrafts are presently in the near-Earth near-equatorial region providing evidence and characteristics of fast flows and Alfvén waves/ KAWs. Meantime, the DMSP observations at low altitude will show when and where the fast flows and Alfvén waves produce the expected iononspheric precipitation. Section 4.1 introduces the background of the satellite observation event. Comparison between hybrid simulation and observations from THEMIS and DMSP satellites is given in Section 4.2. This satellite observation event is associated with a dipolarization front. The ion heating in the near-Earth plasma sheet associated with dipolarization is investigated in Section 4.3. The results are summarized in Section 4.4.

4.1 Background

The solar wind parameters and geomagnetic activity indices are from the OMNI data sets. The OMNI are located around $245R_E$ away from the Earth in the solar wind in 29-Mar-09. Figure 4.1 shows the OMNI data for 29-Mar-09 from 0300-0700 UT. The quantity plotted in panels (a)-(e) is labeled on the vertical axis on the right. There is a sharp turn of B_z component from 4 to $-2\mathrm{nT}$ at 0400 UT as seen from Figure 4.1a. After that B_z is relatively steady and B_y is very small except at about 0440 UT (see Figure4.1b). B_x component is around $-4\mathrm{nT}$ (see Figure 4.1c). Considering the tilt of dipole magnetic field, the reconnection site at the dayside

magnetopause is around at the equator. Thus, purely southward IMF with $B_z = -4.47\mathrm{nT}$ is selected in the simulation case without tilt of dipole magnetic field to keep the reconnection site is around at the equator. Mach number is $M_A = 8.0$ with solar wind flow velocity $V_0 = 405\mathrm{km/s}$, ion number density $N_0 = 3.7\mathrm{cm}^{-3}$, ion temperature $T_{i0} = 7\mathrm{ev}$ and electron-to-ion temperature ratio $T_{e0}/T_{i0} = 2$ in the solar wind. The results in this case is quite similar with that we have obtained from the case in Chapter 3 except the perturbations and fast flows in this case are relatively weaker. Figure 4.1e shows the Auroral Electrojet (AE) Index, which describes the disturbance level recorded by auroral zone magnetometers and represents substorm intensity. The onset of substorm is around 0516 UT as seen by the sharp increase of AE index. Figure 4.1f shows that we are in the early stage of the main phase of a storm as seen by the decrease of Symmetric H-component (SYM/H) index which describes the geomagnetic disturbances at mid-latitudes in terms of longitudinally symmetric disturbances for H component (parallel to the dipole axis).

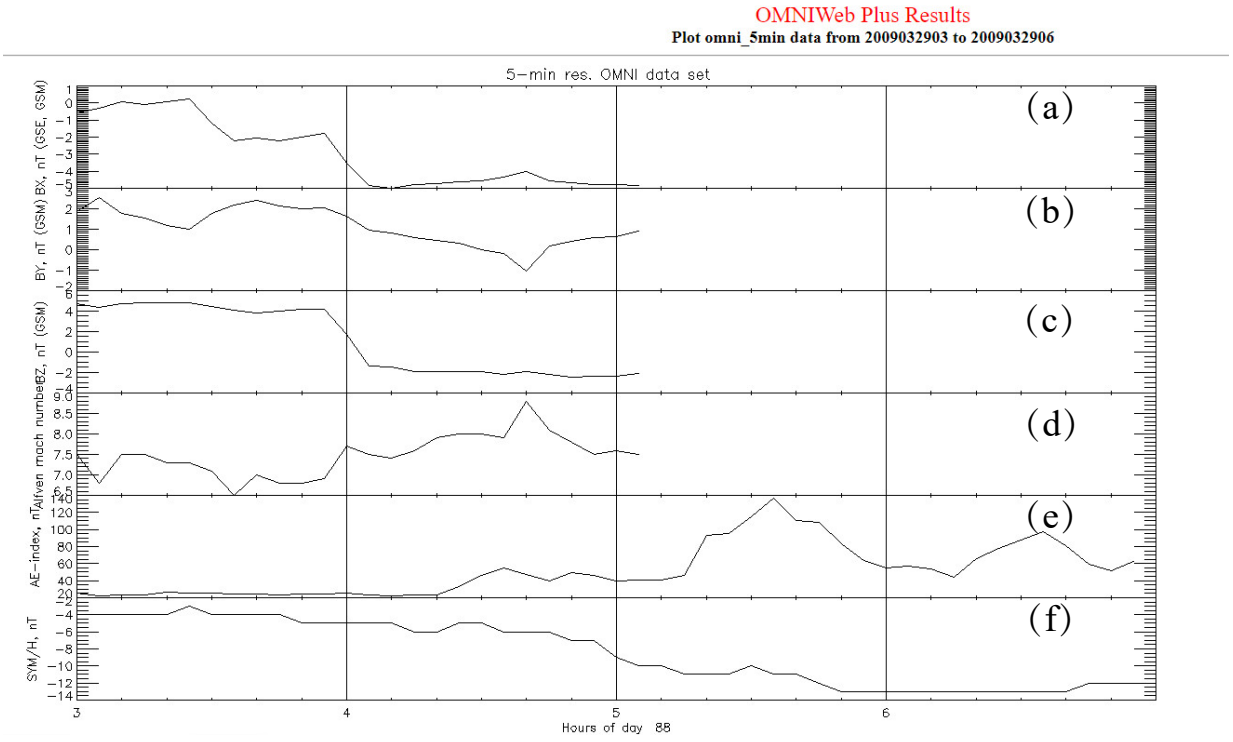

Figure 4.1: OMNI data for 29-Mar-09 from 0300-0700 UT. The quantity plotted in panels (a)–(e) is labeled on the vertical axis on the left. Adapted from *https* : *//omniweb.gsfc.nasa.gov/form/omni_min.html*

Figure 4.2 shows the observation event of 29-Mar-09 from 0430-0600 UT by THEMIS [113]. This event is located on the duskside around $11R_E$ away from the Earth. As shown in Figure 4.2a, the growth phase starts around 0430 UT and the onset of substorms is around 0516 UT. The locations of THEMIS probes are illustrated in Figure 4.2b. The probes are located in the pre midnight of the near-Earth magnetotail with $x \sim 11R_E - 15R_E$. THEMIS P3 (green triangle) is located around $(x, y, z) = (-11.0, 3.0, -0.3)\ R_E$, slightly above the center of plasma sheet marked by the dash magenta line. Next, we will focus on the observation from THEMIS P3 (see Figure 4.3) based on the locations where KAWs are found in the magnetotail.

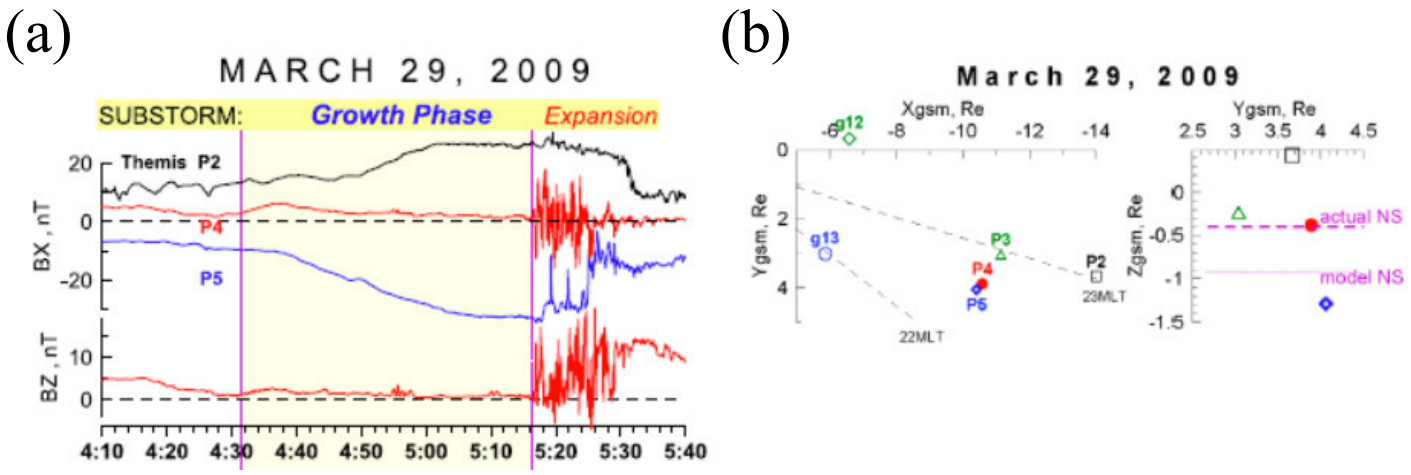

Figure 4.2: (a) Substorm observed by THEMIS (THEMIS P2, P4, P5 probes); (b) Positions of THEMIS. Adapted from Sergeev et al. [113].

4.2 Comparison with Observations from THEMIS and DMSP

As seen in Figure 4.3, both magnetic field (see Figure 4.3a and Figure 4.3b) and electric field (see Figure4.3c) have a larger perturbation from 0515-0530 UT. Meantime, ion flow velocity (see Figure 4.3d) has a sharp increase denoting the spacecraft is passing by fast flows. Combined with the increase of ion energy (see Figure 4.3e), parallel Poynting flux (see Figure4.3f) and particle energy flux density (see Figure 4.3g), this event is likely a KAW event.

To compare with the observation from THEMIS P3, a virtual satellite marked as P1 in Figure 4.4 is put at a fixed location with $(x, y, z) = (-11.0, 6.0, 0.6)\ R_E$. This location is

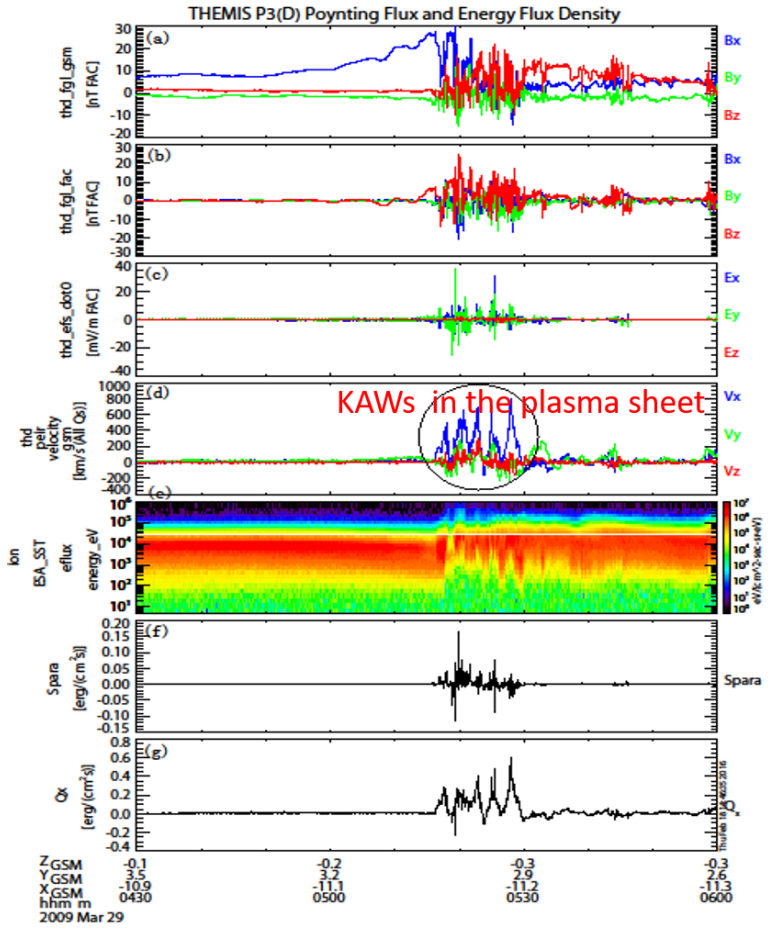

Figure 4.3: Data from THEMIS P3 on 29 March 2009 from $0430 - 0600\mathrm{UT}$. Plotted are (a) GSM components of the magnetic field, (b) field aligned coordinates of the magnetic field, (c) field aligned components of the electric field, (d) GSM components of ion velocity, (e) ion energy spectrum, (f) Poynting flux and (g) energy flux density. Black circle marks a KAW event from $0515 - 0530\mathrm{UT}$.

chosen based on two criteria. Firstly, it is at the location where a dipolarization would pass by near dipole-like and tail-like magnetic field transition region. Secondly, the location should be above the plasma sheet center most of the time. Since the center of plasma sheet is around at the equator in hybrid simulation, a positive z is selected to make sure the virtual satellite is roughly above the center of the plasma sheet same as THEMIS P3. Considering the dipolarization is weak at $(x, y, z) = (-11.0, 3.0, 0.6)\ R_E$ as shown in Figure 4.4, the location of the virtual satellite is shifted duskward about $3.0\ R_E$. The simulation time when the dipolarization arrives the virtual satellite is corresponding to $0516\mathrm{UT}$ when the dipolarization is observed by THEMIS P3. At 0502UT, a weak dipolarization with $B_z \sim 5\mathrm{nT}$ marked by the red rectangle in Figure 4.4a occurs at $17.0\ R_E$ at the equator along the line $y = 6.0\ R_E$. As time proceeds,

the dipolarization propagates earthward and becomes stronger with $B_z \sim 12\mathrm{nT}$. Fourteen minutes later, the dipolarization arrives the virtual satellite as shown in Figure 4.4b. Behind the dipolarization are the fast flows with a peak of $443\mathrm{km/s}$.

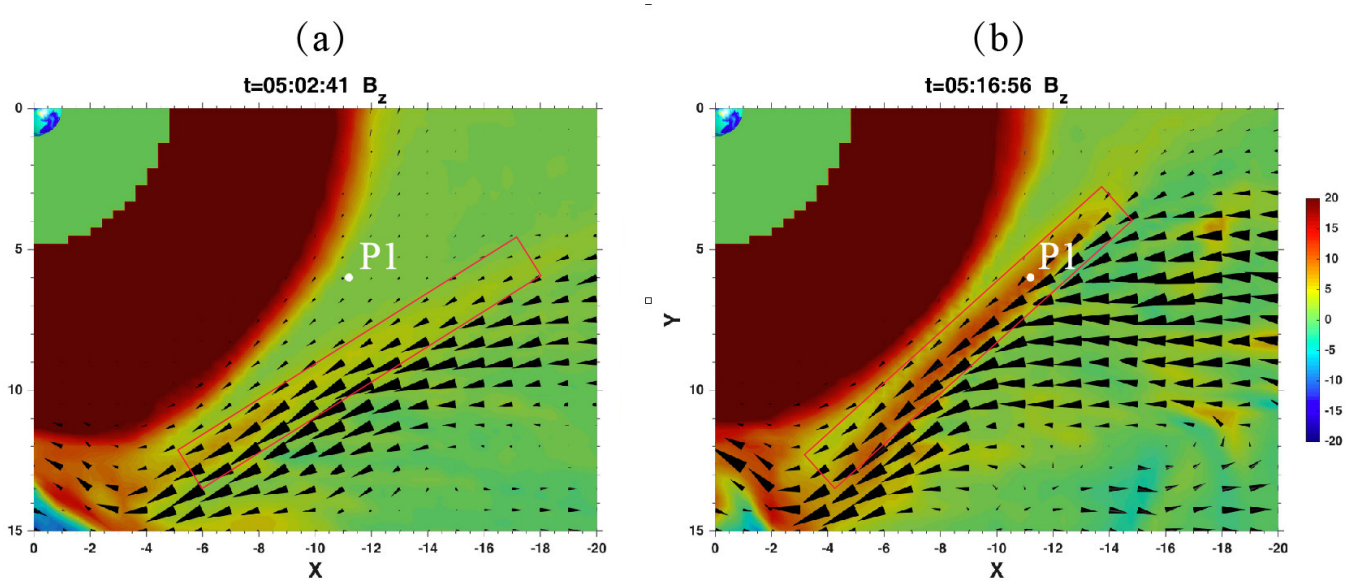

Figure 4.4: Contours of B_z in the equatorial plane at (a) 0502UT and (b) 0516UT show the propagation of dipolarization in hybrid simulation. White point marked as P1 denotes the location of a virtual satellite; red rectangle denotes the dipolarization; Black cones denote ion flow velocity.

Our hybrid simulation results are consistent with the observation results as shown in Figure 4.5 and Figure 4.6. Figure 4.5 shows GSM components of the magnetic field and electric field from THEMIS D (P3) probe (black lines) and hybrid simulation (colorful lines) from $0500 - 0550\mathrm{UT}$. Starting from $t1 = 0516\mathrm{UT}$, B_z is increasing overall, which denotes the arriving of dipolarization. The effects of substorm begin to be detected in the region. After $t1$, strongly wave activities lasting for 18 minutes are seen from $t1$ to $t2 = 0534\mathrm{UT}$ by the perturbations of magnetic field and electric field. As seen from Figure 4.5a-c, The perturbations of magnetic field and electric field are around $10\mathrm{nT}$ (see Figure 4.5a–c) and $10\mathrm{mV/m}$ (see Figure 4.5d–f). Rare wave activities are seen before $t1$ and after $t2$. Figure 4.6 shows magnetic field strength, ion number density, GSM components of the ion flow velocity, and parallel Poynting flux. From $t1$ to $t2$, the oscillation of ion number density is anti-phase with that of the magnetic field as shown in Figure 4.6a-b . The earthward ion flow velocity of fast flows is a few hundred kilometers per second with a peak of around $600\mathrm{km/s}$ (see Figure 4.6c-e).

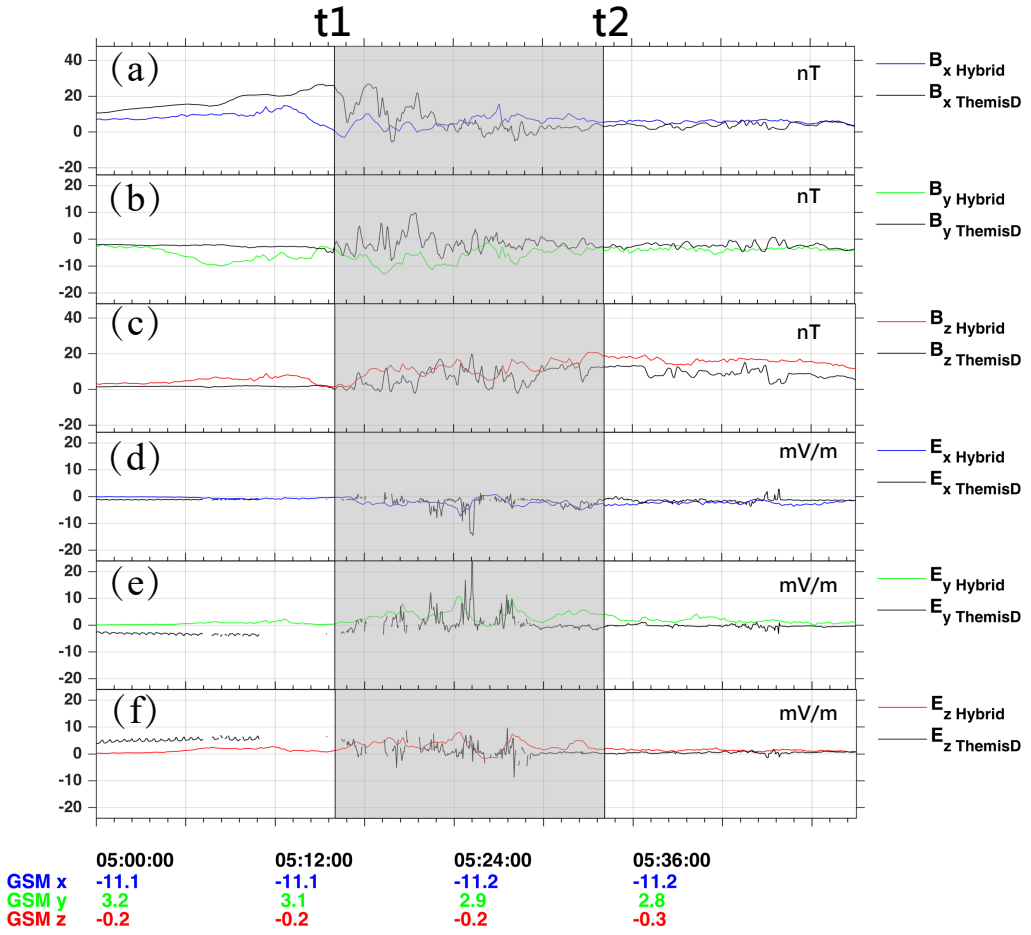

Figure 4.5: Plotted are GSM components of the magnetic field and electric field from THEMIS D (P3) probe and hybrid simulation.

The fast flows pass by every $2-4$ minutes. The peak of parallel Poynting flux is around $0.05-0.1\mathrm{mW/m^2}$. In Figure 4.6f, Poynting flux could be either positive (when the probe is above plasma sheet center) or negative (when the probe is below plasma sheet center) due to the flapping of plasma sheet. Here, we only care about the strength of the Poynting flux.

The wave activities discussed above are KAWs as shown in Figure 4.7. Figure 4.7 shows the time evolution of contours of parallel current density ($J_\parallel$), parallel electric field ($E_\parallel$), transverse magnetic field (B_y), and parallel Poynting flux ($S_\parallel$) in the xz plane at $y = 6.0\ R_E$. At $0502:41$ UT, the values of B_y, $J_\parallel$, $E_\parallel$, and $S_\parallel$ are very small. There is no signatures of KAWs at the location of the virtual satellite P1. At $0506:19$ UT the structures marked by the green rectangles are quite similar with KAWs diagnosed in Chapter 3 except the relatively smaller values of the perturbations, $J_\parallel$ and $E_\parallel$. As time proceeds from $0502:41$ UT to $0506:19$ UT, the KAWs generated in the magnetotail propagate to near-earth dipole-like region and KAWs

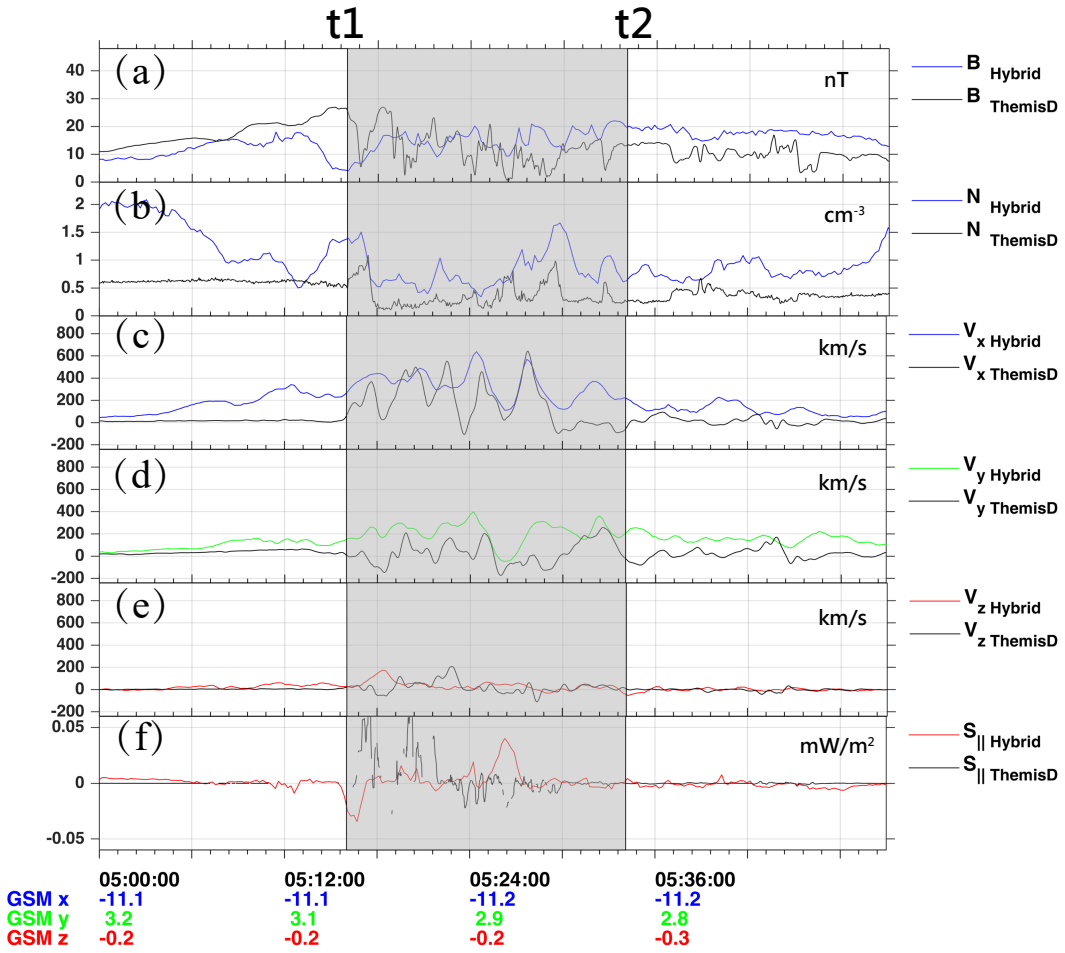

Figure 4.6: Plotted are (a) magnetic field strength, (b) ion number density, (c-e) GSM components of the ion flow velocity, and (f) parallel Poynting flux from THEMIS D(P3) probe and hybrid simulation.

generated in the flow-braking region also appears. The two kind of KAWs are both denoted by the green rectangles in Figure 4.7.

What happened at the meantime in the ionosphere? THEMIS P3(D) locations (when the parallel pointing flux is observed) are mapped to the ionosphere using Tsyganenko T96 model: $(MLAT, MLT) = (-68.8, 22.75)$ to $(-67.3, 22.8)$. The Tsyganenko models are semi-empirical magnetic models , based on observations of a large number of satellites (IMP, ISEE, POLAR, Geotail, etc). The closest conjunction in time and space from DMSP are DMSP F17 from $0521 - 0522$UT marked as cyan line in Figure 4.8a. Evidence of broadband acceleration (proxy for Alfven waves) is shown in Figure 4.8b during this time.The locations of DMSP F17 at 0521 UT and 0522 UT are mapped to the equator at $(x, y, z) = (-24.0, 9.7, 0)$ R_E (see the line L1 in Figure 4.9) near the location of magnetic reconnection and $(x, y, z) =$

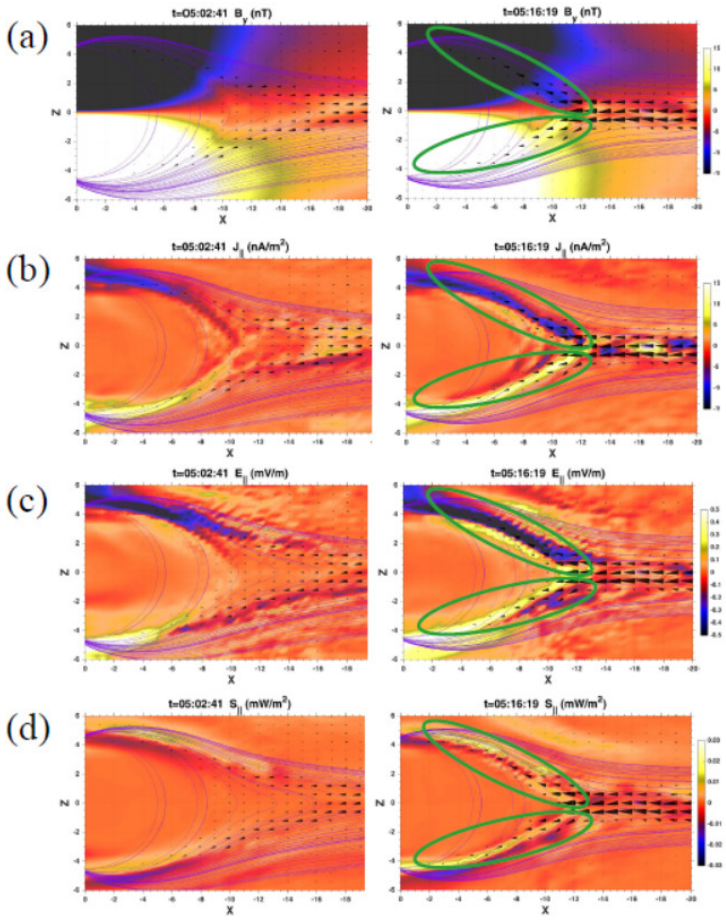

Figure 4.7: Contours of (a) transverse magnetic field (B_y), (b) parallel current density ($J_\parallel$), (c) parallel electric field ($E_\parallel$) and (d) parallel Poynting flux ($S_\parallel$) at $0502:41$ UT and $0506:19$ UT with typical magnetic field fines and ion flow velocity(black cones) in the plane $y = 6.0\ R_E$.

$(-11.1, 7.6, 0)\ R_E$ (see the line L2 in Figure 4.9) in the flow-braking region on the duskside, respectively. These locations are in the regions where KAWs are found in our simulation as shown in Section 3.3 and Section 3.4. Other DMSP events including $F13\ 0538 - 0544$ at $MLT = 23:30 - 02:00$ and $F16\ 0608 - 0612$ at $MLT = 00:39 - 02:17$ during the same period are mapped to around $(x, y, z) = (-9.2, -5.4, 0)\ R_E$ (see the line L4 in Figure 4.9) in the flow-braking region and $(x, y, z) = (-18.2, -7.7, 0)\ R_E$ (see the line L3 in Figure 4.9) near the location of magnetic reconnection on the dawnside, respectively. In a summary, THEMIS and DMSP observations show the presence of shear Alfvén signatures under a similar upstream condition, associated with fast flows. The coordinated THEMIS and DMSP events illustrate the spatial connection between the local plasma sheet and the ionosphere. The shear

Alfvén events of DMSP are mapped to various locations in the plasma sheet, similar to the simulation.

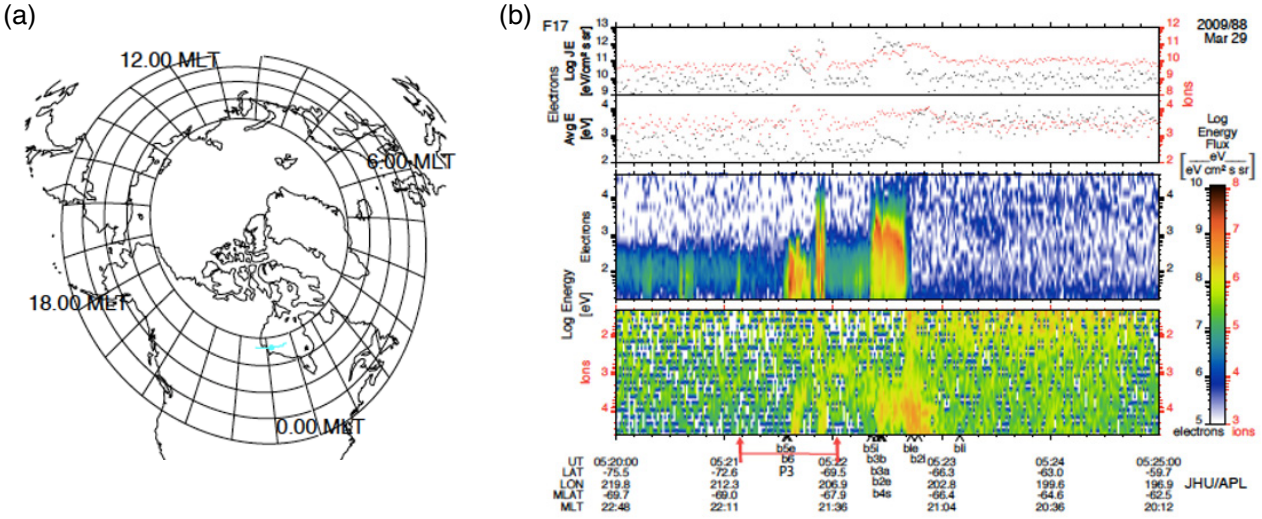

Figure 4.8: (a) Locations of DMSP F17 from 0521–0522 UT (cyan line) and (b) spectrum of energy and energy flux for ions and electrons, respectively.

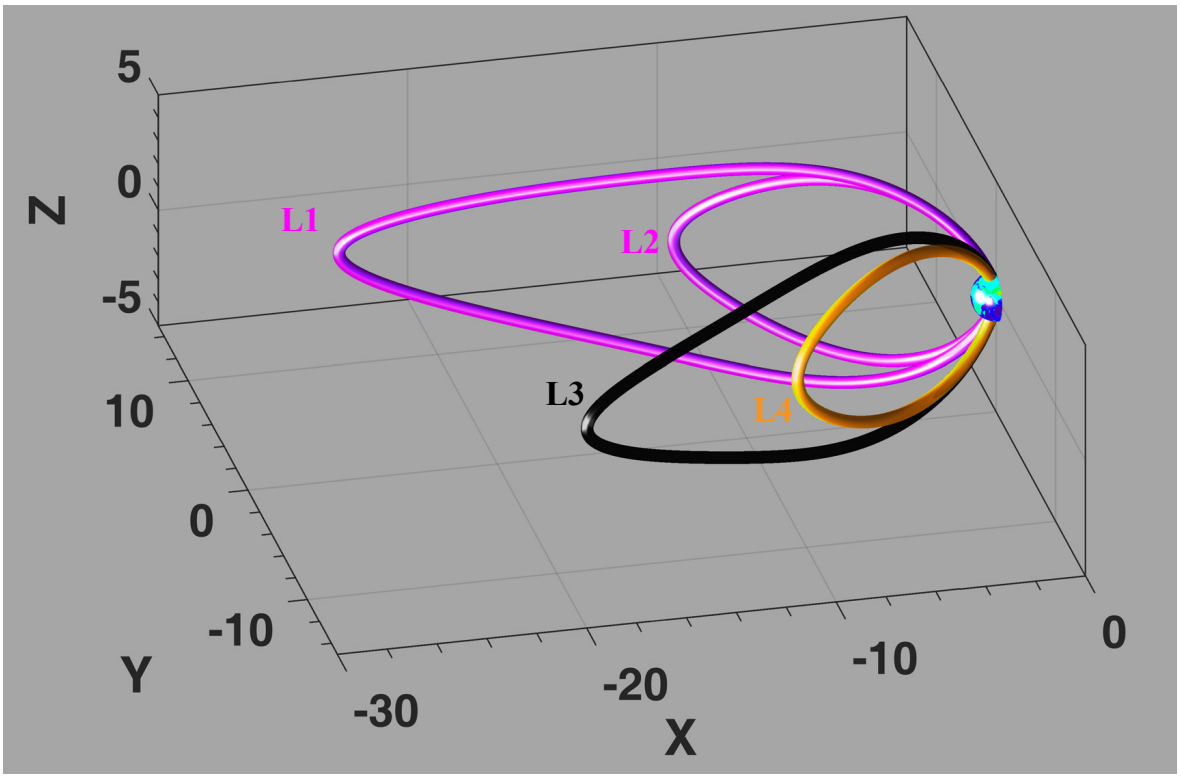

Figure 4.9: Typical magnetic field lines mapped to the equator from the ionosphere for near-Earth magnetotail (L1 on the duskside and L3 on the dawnside) and flow-braking region (L2 on the duskside and L4 on the dawnside), where magenta lines are obtained from DMSP F17 event, and the orange and black lines are from DMSP F13 and F16 events, respectively.

4.3 Ion Heating in the Near-Earth Plasma Sheet Associated with Dipolarization

The ion velocity distributions $f(V_{||}, V_{\perp 1})$ (left column) and $f(V_{||}, V_{\perp 1})$ (right column) at the location of virtual satellite P1 associate with dipolarization are shown in Figure 4.10. $V_{||}$ is along the local magnetic field line, $V_{\perp 1}$ is in $x-z$ plane and perpendicular to the magnetic field line and $V_{\perp 2}$ is perpendicular to both $V_{||}$ and $V_{\perp 1}$. Before the peak of dipolarization arrives, a high-speed earthward ion beam, centered at about $V_{||} = 350\mathrm{km/s}$, is observed at $t = 0516 : 49$UT, coexisting with another lower-speed tailward ion beam at about $V_{||} = -250\mathrm{km/s}$. $V_{\perp 2}$ is around $-180\mathrm{km/s}$ for both of them with $V_{\perp 1} \sim 0\mathrm{km/s}$ as shown in the top panels in Figure 4.10. The dominating parallel ion heating is likely as a result of the parallel electric field carried by KAWs and reflected KAWs at the inner boundary. The two beams begin to merge as shown in the middle panels at $t = 0517 : 24$UT. The tailward ion beam encounters the dipolarization and is reflected earthward by the earthward propagating dipolarization due to the dipolarization front-associated E_y field as illustrated by Zhou et al. (2010) [145]. Then ion beam is braked to be centered at $V_{||} = 150\mathrm{km/s}$ in the parallel direction by the dipole-like field while ions are heated by Betatron heating to be centered at $V_{\perp 2} = -450\mathrm{km/s}$ and $V_{\perp 1} = 100\mathrm{km/s}$ as seen by the bottom panels at $t = 0518 : 43$UT.

4.4 Summary

In this chapter, our simulation result are compared with the observations from THEMIS and DMSP satellites. The results are shown below.

1. The wave structure during a substorm is investigated in the simulation. Our hybrid simulation results are consistent with THEMIS P3(D) observations.

2. Kinetic Alfvén waves are observed by THEMIS in the plasma sheet, and the corresponding shear Alfvénic signatures are observed by DMSP. The shear Alfvén events observed by DMSP are found to be mapped to various locations in the plasma sheet from $x = -25\ R_E$ (consistent with magnetic reconnection region in our simulation) to $x = -9\ R_E$ (consistent with the flow-braking region in our simulation).

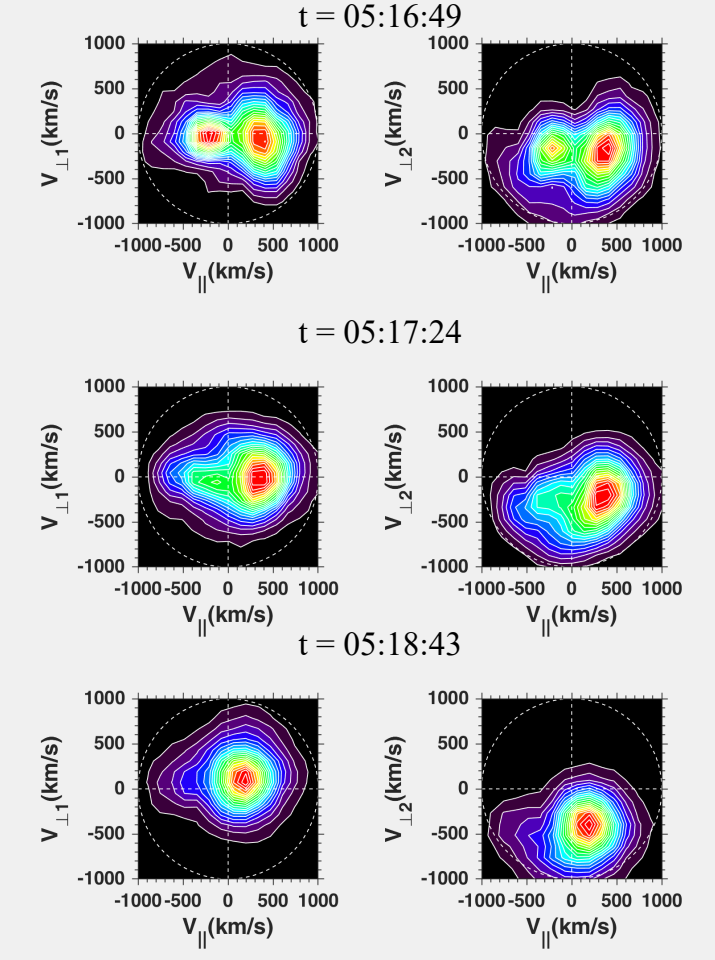

Figure 4.10: Ion velocity distributions $f(V_{||}, V_{\perp 1})$ (left column) and $f(V_{||}, V_{\perp 2})$ (right column) at the location of virtual satellite P1, at $t = 0516:49$UT, $t = 0517:24$UT, and $t = 0518:43$UT. $V_{||}$ is along the local magnetic field line, $V_{\perp 1}$ is in $x-z$ plane and perpendicular to the magnetic field line and $V_{\perp 2}$ is in the direction to complete the orthogonal coordinate.

3. Ion velocity distributions at the location of virtual satellite P1 near dipolarization are investigated. The parallel ion heating is likely as a result of the parallel electric field carried by KAWs and reflected KAWs at the inner boundary. The two beams merge due to the tailward ion beam encounters the dipolarization and is reflected earthward by the earthward propagating dipolarization. Eventually, parallel energy is transferred to perpendicular energy at the flow-braking region.

Chapter 5

Summary and Future Work

In this work, a comprehensive investigation based on 3-D global hybrid simulation has been carried out to understand the generation and dynamics of the KAWs associated with reconnection and fast flows in the magnetotail. The simulation results are correlated with the observations from THEMIS and DMSP satellites. The main results are:

1. KAWs are generated by the near-tail reconnection, propagating earthward and tailward. As part of the structure of the reconnection, the electromagnetic fluctuations, parallel electric, parallel currents, and parallel Poynting fluxes are carried by KAWs to the ionosphere. These highly 3-D Alfvénic waves with $k_\perp \gg k_\parallel$ are identified by the polarization and dispersion relations of Alfvén modes. The spectral break of the electromagnetic power spectral density shows that ion kinetic physics begins to show up at $\omega \sim \Omega_i$.

2. As the shear Alfvén waves generated in the tail plasma sheet encounter the strong dipole-like field in the flow braking region, their wave power is found to be altered.

3. KAWs are also generated at the inner edge of flow-braking region in front of the dipole-like field due to the ion inertial effects. Polarization and dispersion relations of these waves are also presented.

4. The total Alfvénic wave energy on the nightside is estimated. Roughly less than $1/7$ of Alfvénic wave energy originating from magnetotail reconnection can cross the transition region around $r = 10.0\ R_E \sim 11.0\ R_E$, and less than $1/14$ of the Alfvénic wave energy from the magnetotail reaches the ionosphere. Magnetotail reconnection, local sources at

the flow-braking region, and mode conversion are the sources of Alfvénic wave energy of the ionosphere.

5. The overall pattern of ion energy flux is consistent with the statistical result of DMSP satellites except for the higher latitude and values. That is reasonable because of the fact that the latitude and values are correlated with the solar wind conditions and the hybrid result is obtained from only a single case.

6. Ion acceleration in the magnetotail is discussed. The ion is seen accelerated and trapped by KAWs associated with magnetic reconnection and flow braking. Ions are also accelerated when crossing the low-latitude boundary layer. An increased gyro-averaged magnetic moment at the stage of ion acceleration indicates the perpendicular stochastic heating of ions.

7. Most of the ions drift westward due to magnetic drift at the flow braking region near substorm current wedge. Part of the ions at low energy level (below around $20\mathrm{keV}$) are seen to drift eastward when the eastward drift velocity caused by localized $\mathbf{E} \times \mathbf{B}$ drift is larger than the westward drift velocity caused by the magnetic drift.

8. The wave structure during a substorm is investigated in the simulation. Our hybrid simulation results are consistent with THEMIS P3(D) observations.

9. Kinetic Alfvén waves are observed by THEMIS in the plasma sheet, and the corresponding shear Alfvénic signatures are observed by DMSP. The shear Alfvén events observed by DMSP are found to be mapped to various locations in the plasma sheet from $x = -25\ R_E$ (consistent with magnetic reconnection region in our simulation) to $x = -9\ R_E$ (consistent with the flow-braking region in our simulation).

10. Ion velocity distributions at the location of virtual satellite P1 associate with dipolarization are investigated. The parallel ion heating is likely as a result of the parallel electric field carried by KAWs and reflected KAWs at the inner boundary. The two beams merge due to the tailward ion beam encounters the dipolarization and is reflected earthward by

the earthward propagating dipolarization. Eventually, parallel energy is transferred to perpendicular energy at the flow-braking region.

The simulation in the previous chapters is only focusing on cases with purely southward IMF. There are still a lot of work to do mainly in two directions as listed below.

Firstly, the magnetospheric preconditioning can affect the response of the inner magnetosphere [72]. In the future, the steady southward IMF cases will be extended to include the IMF direction change. The IMF direction change can be carried into the simulation domain by an interplanetary rotational discontinuity(RD) with different width. Cases in which the IMF B_z component is initially northward and then turns southward will be investigated under different solar wind conditions. By looking at the southward turning following a northward IMF, we will examine the effect on the generation, dynamics evolution, and trend of Alfvénic fluctuations in the tail magnetosphere and its impact on the ionosphere.

Secondly, since a fraction of IMF By can penetrate into the plasma sheet, a guide field reconnection may exist in the tail. The strength of Alfvénic and compressional waves as well as the energy carried by KAWs depend on the guide field [75]. Previous global MHD simulations indicated that in the presence of the IMF B_y, the plasma sheet exhibits a twist and/or stretch [121]. Satellite observations found that the IMF B_y causes the tail field to depart from bilateral symmetry [72]. The asymmetry of fast flows and Alfvénic fluctuations will be examined under southward IMF with a stronger guide field B_y.

References

[1] SI Akasofu. Polar and magnetospheric substorms, reidel publ. *Co., Dordrecht, Holland*, 1968.

[2] Hannes Alfvén. Existence of electromagnetic-hydrodynamic waves. *Nature*, 150(3805):405–406, 1942.

[3] RR Anderson, CC Harvey, MM Hoppe, BT Tsurutani, TE Eastman, and J Etcheto. Plasma waves near the magnetopause. *Journal of Geophysical Research: Space Physics*, 87(A4):2087–2107, 1982.

[4] V Angelopoulos, JA Chapman, FS Mozer, JD Scudder, CT Russell, K Tsuruda, T Mukai, TJ Hughes, and K Yumoto. Plasma sheet electromagnetic power generation and its dissipation along auroral field lines. *Journal of Geophysical Research: Space Physics*, 107(A8):SMP–14, 2002.

[5] V Angelopoulos, CF Kennel, FV Coroniti, R Pellat, MG Kivelson, RJ Walker, CT Russell, W Baumjohann, WC Feldman, and JT Gosling. Statistical characteristics of bursty bulk flow events. *Journal of Geophysical Research: Space Physics*, 99(A11):21257–21280, 1994.

[6] V Angelopoulos, TD Phan, DE Larson, FS Mozer, RP Lin, K Tsuruda, H Hayakawa, T Mukai, S Kokubun, T Yamamoto, et al. Magnetotail flow bursts: association to global magnetospheric circulation, relationship to ionospheric activity and direct evidence for localization. *Geophysical research letters*, 24(18):2271–2274, 1997.

[7] Vassilis Angelopoulos, Wo Baumjohann, CF Kennel, F Vo Coroniti, MG Kivelson, R Pellat, RJ Walker, H Lühr, and G Paschmann. Bursty bulk flows in the inner central plasma sheet. *Journal of Geophysical Research: Space Physics*, 97(A4):4027–4039, 1992.

[8] Vassilis Angelopoulos, James P McFadden, Davin Larson, Charles W Carlson, Stephen B Mende, Harald Frey, Tai Phan, David G Sibeck, Karl-Heinz Glassmeier, Uli Auster, et al. Tail reconnection triggering substorm onset. *Science*, 321(5891):931–935, 2008.

[9] Aaron Barnes and Joseph V Hollweg. Large-amplitude hydromagnetic waves. *Journal of Geophysical Research*, 79(16):2302–2318, 1974.

[10] W Baumjohann, M Hesse, S Kokubun, T Mukai, T Nagai, and AA Petrukovich. Substorm dipolarization and recovery. *Journal of Geophysical Research: Space Physics*, 104(A11):24995–25000, 1999.

[11] Wolfgang Baumjohann, Götz Paschmann, and Hermann Lühr. Characteristics of high-speed ion flows in the plasma sheet. *Journal of Geophysical Research: Space Physics*, 95(A4):3801–3809, 1990.

[12] JW Belcher, Leverett Davis, and EJ Smith. Large-amplitude alfvén waves in the interplanetary medium: Mariner 5. *Journal of Geophysical Research*, 74(9):2302–2308, 1969.

[13] Charles K Birdsall and A Bruce Langdon. *Plasma physics via computer simulation*. CRC press, 2018.

[14] J Birn, JF Drake, MA Shay, BN Rogers, RE Denton, M Hesse, M Kuznetsova, ZW Ma, A Bhattacharjee, A Otto, et al. Geospace environmental modeling (gem) magnetic reconnection challenge. *Journal of Geophysical Research: Space Physics*, 106(A3):3715–3719, 2001.

[15] Joachim Birn and Eric Ronald Priest. *Reconnection of magnetic fields: magnetohydrodynamics and collisionless theory and observations*. Cambridge University Press, 2007.

[16] Michael N Caan, Robert L McPherron, and Christopher T Russell. Solar wind and substorm-related changes in the lobes of the geomagnetic tail. *Journal of Geophysical Research*, 78(34):8087–8096, 1973.

[17] C Chaston, J Bonnell, JP McFadden, CW Carlson, C Cully, O Le Contel, A Roux, HU Auster, KH Glassmeier, V Angelopoulos, et al. Turbulent heating and cross-field transport near the magnetopause from themis. *Geophysical Research Letters*, 35(17), 2008.

[18] CC Chaston, JW Bonnell, L Clausen, and V Angelopoulos. Correction to "energy transport by kinetic-scale electromagnetic waves in fast plasma sheet flows". *Journal of Geophysical Research: Space Physics*, 117(A12), 2012.

[19] CC Chaston, CW Carlson, WJ Peria, RE Ergun, and JP McFadden. Fast observations of inertial alfvén waves in the dayside aurora. *Geophysical research letters*, 26(6):647–650, 1999.

[20] CC Chaston, Vincent Génot, JW Bonnell, CW Carlson, JP McFadden, RE Ergun, RJ Strangeway, EJ Lund, and KJ Hwang. Ionospheric erosion by alfvén waves. *Journal of Geophysical Research: Space Physics*, 111(A3), 2006.

[21] CC Chaston, JR Johnson, M Wilber, M Acuna, ML Goldstein, and H Reme. Kinetic alfvén wave turbulence and transport through a reconnection diffusion region. *Physical review letters*, 102(1):015001, 2009.

[22] CC Chaston, M Wilber, FS Mozer, Masaki Fujimoto, ML Goldstein, M Acuna, H Reme, and A Fazakerley. Mode conversion and anomalous transport in kelvin-helmholtz vortices and kinetic alfvén waves at the earth's magnetopause. *Physical review letters*, 99(17):175004, 2007.

[23] Christopher C Chaston, John W Bonnell, John R Wygant, Forrest Mozer, Stuart D Bale, Kris Kersten, Aaron W Breneman, Craig A Kletzing, William S Kurth, George B Hospodarsky, et al. Observations of kinetic scale field line resonances. *Geophysical Research Letters*, 41(2):209–215, 2014.

[24] Chio-Zong Cheng and Jay R Johnson. A kinetic-fluid model. *Journal of Geophysical Research: Space Physics*, 104(A1):413–427, 1999.

[25] LBN Clausen, JBH Baker, JM Ruohoniemi, SE Milan, and BJ Anderson. Dynamics of the region 1 birkeland current oval derived from the active magnetosphere and planetary electrodynamics response experiment (ampere). *Journal of Geophysical Research: Space Physics*, 117(A6), 2012.

[26] Richard Courant, Kurt Friedrichs, and Hans Lewy. Über die partiellen differenzengleichungen der mathematischen physik. *Mathematische annalen*, 100(1):32–74, 1928.

[27] SWH Cowley. Magnetosphere-ionosphere interactions: A tutorial review. *Magnetospheric Current Systems, Geophys. Monogr. Ser*, 118:91–106, 2000.

[28] JC Coxon, SE Milan, LBN Clausen, BJ Anderson, and H Korth. The magnitudes of the regions 1 and 2 birkeland currents observed by ampere and their role in solar wind-magnetosphere-ionosphere coupling. *Journal of Geophysical Research: Space Physics*, 119(12):9804–9815, 2014.

[29] Lei Dai. Collisionless magnetic reconnection via alfvén eigenmodes. *Physical review letters*, 102(24):245003, 2009.

[30] Lei Dai, Chi Wang, Yongcun Zhang, Benoit Lavraud, James Burch, Craig Pollock, and Roy B Torbert. Kinetic alfvén wave explanation of the hall fields in magnetic reconnection. *Geophysical Research Letters*, 44(2):634–640, 2017.

[31] PA Damiano, JR Johnson, and CC Chaston. Ion temperature effects on magnetotail alfvén wave propagation and electron energization. *Journal of Geophysical Research: Space Physics*, 120(7):5623–5632, 2015.

[32] PA Damiano, E-H Kim, JR Johnson, and P Porazik. Electron energization by parallel electric fields in poloidal standing waves. *Journal of Geophysical Research: Space Physics*, 124, 2019.

[33] William Daughton, Jack Scudder, and Homa Karimabadi. Fully kinetic simulations of undriven magnetic reconnection with open boundary conditions. *Physics of Plasmas*, 13(7):072101, 2006.

[34] M Dobrowolny. Velocity shear instability of alfvén waves in a high β collisionless plasma. *The Physics of Fluids*, 20(6):1027–1028, 1977.

[35] Marino Dobrowolny. Kelvin-helmholtz instability in a high-β collisionless plasma. *The Physics of Fluids*, 15(12):2263–2270, 1972.

[36] SP Duan, Lei Dai, Chi Wang, J Liang, ATY Lui, LJ Chen, ZH He, YC Zhang, and V Angelopoulos. Evidence of kinetic alfvén eigenmode in the near-earth magnetotail during substorm expansion phase. *Journal of Geophysical Research: Space Physics*, 121(5):4316–4330, 2016.

[37] EM Dubinin, PL Israelevich, and NS Nikolaeva. Auroral electromagnetic disturbances at an altitude of 900 km: The relationship between the electric and magnetic field variations. *Planetary and space science*, 38(1):97–108, 1990.

[38] James W Dungey. Interplanetary magnetic field and the auroral zones. *Physical Review Letters*, 6(2):47, 1961.

[39] JP Eastwood, TD Phan, M Øieroset, and MA Shay. Average properties of the magnetic reconnection ion diffusion region in the earth's magnetotail: The 2001–2005 cluster observations and comparison with simulations. *Journal of Geophysical Research: Space Physics*, 115(A8), 2010.

[40] Yusuke Ebihara and Takashi Tanaka. Evolution of auroral substorm as viewed from mhd simulations: dynamics, energy transfer and energy conversion. *Reviews of Modern Plasma Physics*, 4(1):1–29, 2020.

[41] M Fujimoto, MS Nakamura, I Shinohara, T Nagai, T Mukai, Y Saito, T Yamamoto, and S Kokubun. Observations of earthward streaming electrons at the trailing boundary of a plasmoid. *Geophysical research letters*, 24(22):2893–2896, 1997.

[42] N Yu Ganushkina, MW Liemohn, and S Dubyagin. Current systems in the earth's magnetosphere. *Reviews of Geophysics*, 56(2):309–332, 2018.

[43] Natalia Yu Ganushkina, Michael W Liemohn, S Dubyagin, IA Daglis, I Dandouras, DL De Zeeuw, Y Ebihara, Raluca Ilie, R Katus, M Kubyshkina, et al. Defining and resolving current systems in geospace. *arXiv preprint arXiv:1701.04714*, 2017.

[44] Daniel J Gershman, F Adolfo, John C Dorelli, Scott A Boardsen, Levon A Avanov, Paul M Bellan, Steven J Schwartz, Benoit Lavraud, Victoria N Coffey, Michael O Chandler, et al. Wave-particle energy exchange directly observed in a kinetic alfvén-branch wave. *Nature communications*, 8:14719, 2017.

[45] Nicolas Gillet, Dominique Jault, Elisabeth Canet, and Alexandre Fournier. Fast torsional waves and strong magnetic field within the earths core. *Nature*, 465(7294):74–77, 2010.

[46] RG Giovanelli. A theory of chromospheric flares. *Nature*, 158(4003):81–82, 1946.

[47] CK Goertz. Kinetic alfvén waves on auroral field lines. *Planetary and Space Science*, 32(11):1387–1392, 1984.

[48] CK Goertz and RW Boswell. Magnetosphere-ionosphere coupling. *Journal of Geophysical Research: Space Physics*, 84(A12):7239–7246, 1979.

[49] RA Greenwald and ADM Walker. Energetics of long period resonant hydromagnetic waves. *Geophysical Research Letters*, 7(10):745–748, 1980.

[50] Zhifang Guo, Minghua Hong, Yu Lin, Aimin Du, Xueyi Wang, Mingyu Wu, and Quanming Lu. Generation of kinetic alfven waves in the high-latitude near-earth magnetotail: A global hybrid simulation. *Physics of Plasmas*, 22(2):022117, 2015.

[51] Donald A Gurnett and Amitava Bhattacharjee. *Introduction to plasma physics: with space and laboratory applications*. Cambridge university press, 2005.

[52] Douglas C Hamilton, G Gloeckler, FM Ipavich, W Stüdemann, B Wilken, and G Kremser. Ring current development during the great geomagnetic storm of february 1986. *Journal of Geophysical Research: Space Physics*, 93(A12):14343–14355, 1988.

[53] Akira Hasegawa. Kinetic theory of mhd instabilities in a nonuniform plasma. *Solar Physics*, 47(1):325–330, 1976.

[54] Akira Hasegawa and Liu Chen. Kinetic processes in plasma heating by resonant mode conversion of alfvén wave. *The Physics of Fluids*, 19(12):1924–1934, 1976.

[55] Michael Hesse and Joachim Birn. On dipolarization and its relation to the substorm current wedge. *Journal of Geophysical Research: Space Physics*, 96(A11):19417–19426, 1991.

[56] Robert E Holzer and James A Slavin. A correlative study of magnetic flux transfer in the magnetosphere. *Journal of Geophysical Research: Space Physics*, 84(A6):2573–2578, 1979.

[57] MH Hong, DW Swift, and Y Lin. Ion dynamics associated with alfven wave in the near-earth magnetotail: Two-dimensional global hybrid simulation. *Advances in Space Research*, 41(8):1298–1304, 2008.

[58] M Hoshino, T Mukai, T Terasawa, and I Shinohara. Suprathermal electron acceleration in magnetic reconnection. *Journal of Geophysical Research: Space Physics*, 106(A11):25979–25997, 2001.

[59] Guang-Li Huang, De-Yu Wang, De-Jin Wu, H De Feraudy, D Le Quéau, M Volwerk, and Bengt Holback. The eigenmode of solitary kinetic alfvén waves observed by freja satellite. *Journal of Geophysical Research: Space Physics*, 102(A4):7217–7224, 1997.

[60] PD Hudson. Rotational discontinuities in an anisotropic plasma. *Planetary and Space Science*, 19(12):1693–1699, 1971.

[61] Fu Huishan, Grigorenko Elena, Gabrielse Christine, Liu Chengming, Lu San, Hwang Kyoung-Joo, Zhou Xuzhi, Wang Zhe, and Chen Fang. Magnetotail dipolarization fronts and particle acceleration: A review. *SCIENCE CHINA Earth Sciences*.

[62] JA Jacobs, Y Kato, S Matsushita, and VA Troitskaya. Classification of geomagnetic micropulsations. *Journal of Geophysical Research*, 69(1):180–181, 1964.

[63] Jay R Johnson and CZ Cheng. Kinetic alfvén waves and plasma transport at the magnetopause. *Geophysical research letters*, 24(11):1423–1426, 1997.

[64] Y Kamide and S Matsushita. Simulation studies of ionospheric electric fields and currents in relation to field-aligned currents, 2. substorms. *Journal of Geophysical Research: Space Physics*, 84(A8):4099–4115, 1979.

[65] H Karimabadi, V Roytershteyn, HX Vu, YA Omelchenko, J Scudder, W Daughton, A Dimmock, K Nykyri, M Wan, D Sibeck, et al. The link between shocks, turbulence, and magnetic reconnection in collisionless plasmas. *Physics of Plasmas*, 21(6):062308, 2014.

[66] A Keiling, V Angelopoulos, A Runov, J Weygand, SV Apatenkov, S Mende, J McFadden, D Larson, O Amm, K-H Glassmeier, et al. Substorm current wedge driven by plasma flow vortices: Themis observations. *Journal of Geophysical Research: Space Physics*, 114(A1), 2009.

[67] A Keiling, JR Wygant, C Cattell, M Temerin, FS Mozer, CA Kletzing, J Scudder, CT Russell, W Lotko, and AV Streltsov. Large alfvén wave power in the plasma sheet boundary layer during the expansion phase of substorms. *Geophysical Research Letters*, 27(19):3169–3172, 2000.

[68] Andreas Keiling. Alfvén waves and their roles in the dynamics of the earth's magnetotail: A review. *Space Science Reviews*, 142(1-4):73–156, 2009.

[69] Yu V Khotyaintsev, CM Cully, Andris Vaivads, Mats André, and CJ Owen. Plasma jet braking: Energy dissipation and nonadiabatic electrons. *Physical Review Letters*, 106(16):165001, 2011.

[70] Atmo Kivelson. *Introduction to space physics*. Cambridge university press, 1995.

[71] Nicholas A Krall and Alvin W Trivelpiece. Principles of plasma physics. *American Journal of Physics*, 41(12):1380–1381, 1973.

[72] Benoit Lavraud, E Larroque, E Budnik, Vincent Génot, JE Borovsky, MW Dunlop, Claire Foullon, H Hasegawa, C Jacquey, Katariina Nykyri, et al. Asymmetry of magnetosheath flows and magnetopause shape during low alfvén mach number solar wind. *Journal of Geophysical Research: Space Physics*, 118(3):1089–1100, 2013.

[73] Robert J Leamon, Charles W Smith, Norman F Ness, William H Matthaeus, and Hung K Wong. Observational constraints on the dynamics of the interplanetary magnetic field dissipation range. *Journal of Geophysical Research: Space Physics*, 103(A3):4775–4787, 1998.

[74] Lou C Lee and ZF Fu. A theory of magnetic flux transfer at the earth's magnetopause. *Geophysical Research Letters*, 12(2):105–108, 1985.

[75] Ji Liang, Yu Lin, Jay R Johnson, Xueyi Wang, and Zheng-Xiong Wang. Kinetic alfvén waves in three-dimensional magnetic reconnection. *Journal of Geophysical Research: Space Physics*, 121(7):6526–6548, 2016.

[76] Ji Liang, Yu Lin, Jay R Johnson, Zheng-Xiong Wang, and Xueyi Wang. Ion acceleration and heating by kinetic alfvén waves associated with magnetic reconnection. *Physics of Plasmas*, 24(10):102110, 2017.

[77] Y Lin and DW Swift. Generation of near-earth reconnection by divergent flows in the plasma sheet. *Journal of Geophysical Research: Space Physics*, 107(A11), 2002.

[78] Y Lin and XY Wang. Three-dimensional global hybrid simulation of dayside dynamics associated with the quasi-parallel bow shock. *Journal of Geophysical Research: Space Physics*, 110(A12), 2005.

[79] Y Lin, XY Wang, S Lu, JD Perez, and Q Lu. Investigation of storm time magnetotail and ion injection using three-dimensional global hybrid simulation. *Journal of Geophysical Research: Space Physics*, 119(9):7413–7432, 2014.

[80] Yu Lin, Jay R Johnson, and Xueyi Wang. Three-dimensional mode conversion associated with kinetic alfvén waves. *Physical review letters*, 109(12):125003, 2012.

[81] Yu Lin, JR Johnson, and XY Wang. Hybrid simulation of mode conversion at the magnetopause. *Journal of Geophysical Research: Space Physics*, 115(A4), 2010.

[82] Yu Lin, Simon Wing, Jay R Johnson, XY Wang, Joe D Perez, and Lei Cheng. Formation and transport of entropy structures in the magnetotail simulated with a 3-d global hybrid code. *Geophysical Research Letters*, 44(12):5892–5899, 2017.

[83] CM Liu, HS Fu, Y Xu, Yuri V Khotyaintsev, JL Burch, RE Ergun, DG Gershman, and RB Torbert. Electron-scale measurements of dipolarization front. *Geophysical Research Letters*, 45(10):4628–4638, 2018.

[84] Jiang Liu, V Angelopoulos, Xu-Zhi Zhou, and A Runov. Magnetic flux transport by dipolarizing flux bundles. *Journal of Geophysical Research: Space Physics*, 119(2):909–926, 2014.

[85] S Lu, Y Lin, QM Lu, XY Wang, RS Wang, C Huang, MY Wu, and S Wang. Evolution of flux ropes in the magnetotail: A three-dimensional global hybrid simulation. *Physics of Plasmas*, 22(5):052901, 2015.

[86] San Lu, Quanming Lu, Yu Lin, Xueyi Wang, Yasong Ge, Rongsheng Wang, Meng Zhou, Huishan Fu, Can Huang, Mingyu Wu, et al. Dipolarization fronts as earthward propagating flux ropes: A three-dimensional global hybrid simulation. *Journal of Geophysical Research: Space Physics*, 120(8):6286–6300, 2015.

[87] ATY Lui. Comment on "tail reconnection triggering substorm onset". *Science*, 324(5933):1391–1391, 2009.

[88] ATY Lui, RE Lopez, SM Krimigis, RW McEntire, LJ Zanetti, and TA Potemra. A case study of magnetotail current sheet disruption and diversion. *Geophysical Research Letters*, 15(7):721–724, 1988.

[89] JG Lyon, RE Lopez, CC Goodrich, M Wiltberger, and K Papadopoulos. Simulation of the march 9, 1995, substorm: Auroral brightening and the onset of lobe reconnection. *Geophysical research letters*, 25(15):3039–3042, 1998.

[90] Robert L Lysak and William Lotko. On the kinetic dispersion relation for shear alfvén waves. *Journal of Geophysical Research: Space Physics*, 101(A3):5085–5094, 1996.

[91] Robert L Lysak and Yan Song. Magnetosphere–ionosphere coupling by alfvén waves: Beyond current continuity. *Advances in Space Research*, 38(8):1713–1719, 2006.

[92] Stefano Markidis, Giovanni Lapenta, et al. Multi-scale simulations of plasma with ipic3d. *Mathematics and Computers in Simulation*, 80(7):1509–1519, 2010.

[93] Robert L McPherron, Christopher T Russell, and Michel P Aubry. Satellite studies of magnetospheric substorms on august 15, 1968: 9. phenomenological model for substorms. *Journal of Geophysical Research*, 78(16):3131–3149, 1973.

[94] FS Mozer, SD Bale, and TD Phan. Evidence of diffusion regions at a subsolar magnetopause crossing. *Physical review letters*, 89(1):015002, 2002.

[95] T Nagai, I Shinohara, M Fujimoto, M Hoshino, Y Saito, S Machida, and T Mukai. Geotail observations of the hall current system: Evidence of magnetic reconnection in the magnetotail. *Journal of Geophysical Research: Space Physics*, 106(A11):25929–25949, 2001.

[96] R Nakamura, W Baumjohann, B Klecker, Y Bogdanova, A Balogh, H Reme, JM Bosqued, I Dandouras, JA Sauvaud, K-H Glassmeier, et al. Motion of the dipolarization front during a flow burst event observed by cluster. *Geophysical Research Letters*, 29(20):3–1, 2002.

[97] R Nakamura, W Baumjohann, C Mouikis, LM Kistler, A Runov, M Volwerk, Y Asano, Z Vörös, TL Zhang, B Klecker, et al. Spatial scale of high-speed flows in the plasma sheet observed by cluster. *Geophysical research letters*, 31(9), 2004.

[98] R Nakamura, A Retinò, W Baumjohann, M Volwerk, N Erkaev, B Klecker, EA Lucek, I Dandouras, Mats André, and Yuri Khotyaintsev. Evolution of dipolarization in the near-earth current sheet induced by earthward rapid flux transport. In *Annales Geophysicae*, volume 27, pages 1743–1754. Copernicus GmbH, 2009.

[99] Yasuhito Narita. *Plasma turbulence in the solar system*. Springer Science & Business Media, 2012.

[100] Norman F Ness. The earth's magnetic tail. *Journal of Geophysical Research*, 70(13):2989–3005, 1965.

[101] S Ohtani, Y Miyashita, H Singer, and T Mukai. Tailward flows with positive bz in the near-earth plasma sheet. *Journal of Geophysical Research: Space Physics*, 114(A6), 2009.

[102] N Omidi, X Blanco-Cano, and CT Russell. Macrostructure of collisionless bow shocks: 1. scale lengths. *Journal of Geophysical Research: Space Physics*, 110(A12), 2005.

[103] Hiro Osaki, Kazue Takahashi, Hiroshi Fukunishi, Tsutomu Nagatsuma, Hiroshi Oya, Ayako Matsuoka, and David K Milling. Pi2 pulsations observed from the akebono satellite in the plasmasphere. *Journal of Geophysical Research: Space Physics*, 103(A8):17605–17615, 1998.

[104] Eugene N Parker. Sweet's mechanism for merging magnetic fields in conducting fluids. *Journal of Geophysical Research*, 62(4):509–520, 1957.

[105] Harry E Petschek. Magnetic field annihilation. *NASA Special Publication*, 50:425, 1964.

[106] Martin Pohl, Masahiro Hoshino, and Jacek Niemiec. Pic simulation methods for cosmic radiation and plasma instabilities. *Progress in Particle and Nuclear Physics*, page 103751, 2019.

[107] CJ Pollock, JL Burch, MG Henderson, J-M Jahn, DJ Mccomas, SB Mende, DG Mitchell, GD Reeves, EE Scime, RM Skoug, et al. The role and contributions of energetic neutral atom (ena) imaging in magnetospheric substorm research. In *Magnetospheric ImagingThe Image Prime Mission*, pages 155–182. Springer, 2003.

[108] Kenneth G Powell, Philip L Roe, Timur J Linde, Tamas I Gombosi, and Darren L De Zeeuw. A solution-adaptive upwind scheme for ideal magnetohydrodynamics. *Journal of Computational Physics*, 154(2):284–309, 1999.

[109] J Raeder, RJ Walker, and M Ashour-Abdalla. The structure of the distant geomagnetic tail during long periods of northward imf. *Geophysical research letters*, 22(4):349–352, 1995.

[110] JRLM Raeder, RL McPherron, LA Frank, S Kokubun, G Lu, T Mukai, WR Paterson, JB Sigwarth, HJ Singer, and JA Slavin. Global simulation of the geospace environment modeling substorm challenge event. *Journal of Geophysical Research: Space Physics*, 106(A1):381–395, 2001.

[111] A Runov, V Angelopoulos, MI Sitnov, VA Sergeev, J Bonnell, JP McFadden, D Larson, K-H Glassmeier, and U Auster. Themis observations of an earthward-propagating dipolarization front. *Geophysical Research Letters*, 36(14), 2009.

[112] VS Semenov, T Penz, VV Ivanova, VA Sergeev, HK Biernat, R Nakamura, MF Heyn, IV Kubyshkin, and IB Ivanov. Reconstruction of the reconnection rate from cluster measurements: First results. *Journal of Geophysical Research: Space Physics*, 110(A11), 2005.

[113] V Sergeev, V Angelopoulos, M Kubyshkina, E Donovan, X-Z Zhou, A Runov, H Singer, J McFadden, and R Nakamura. Substorm growth and expansion onset as observed with ideal ground-spacecraft themis coverage. *Journal of Geophysical Research: Space Physics*, 116(A5), 2011.

[114] VA Sergeev, V Angelopoulos, JT Gosling, CA Cattell, and CT Russell. Detection of localized, plasma-depleted flux tubes or bubbles in the midtail plasma sheet. *Journal of Geophysical Research: Space Physics*, 101(A5):10817–10826, 1996.

[115] VA Sergeev, RC Elphic, FS Mozer, A Saint-Marc, and JA Sauvaud. A two-satellite study of nightside flux transfer events in the plasma sheet. *Planetary and space science*, 40(11):1551–1572, 1992.

[116] MA Shay, JF Drake, JP Eastwood, and TD Phan. Super-alfvénic propagation of substorm reconnection signatures and poynting flux. *Physical review letters*, 107(6):065001, 2011.

[117] Feng Shi, Lei Cheng, Yu Lin, and Xueyi Wang. Foreshock wave interaction with the magnetopause: Signatures of mode conversion. *Journal of Geophysical Research: Space Physics*, 122(7):7057–7076, 2017.

[118] Feng Shi, Yu Lin, and Xueyi Wang. Global hybrid simulation of mode conversion at the dayside magnetopause. *Journal of Geophysical Research: Space Physics*, 118(10):6176–6187, 2013.

[119] MJ Shi, CJ Xiao, QS Li, HG Wang, XG Wang, and H Li. Observations of alfvén and slow waves in the solar wind near 1 au. *The Astrophysical Journal*, 815(2):122, 2015.

[120] Kazuo Shiokawa, Wolfgang Baumjohann, and Gerhard Haerendel. Braking of high-speed flows in the near-earth tail. *Geophysical research letters*, 24(10):1179–1182, 1997.

[121] DG Sibeck and R-Q Lin. Size and shape of the distant magnetotail. *Journal of Geophysical Research: Space Physics*, 119(2):1028–1043, 2014.

[122] K Sigsbee, CA Cattell, D Fairfield, K Tsuruda, and S Kokubun. Geotail observations of low-frequency waves and high-speed earthward flows during substorm onsets in the near magnetotail from 10 to 13 re. *Journal of Geophysical Research: Space Physics*, 107(A7):SMP–27, 2002.

[123] MI Sitnov, M Swisdak, and AV Divin. Dipolarization fronts as a signature of transient reconnection in the magnetotail. *Journal of Geophysical Research: Space Physics*, 114(A4), 2009.

[124] JE Stawarz, JP Eastwood, A Varsani, RE Ergun, MA Shay, R Nakamura, TD Phan, JL Burch, DJ Gershman, BL Giles, et al. Magnetospheric multiscale analysis of intense field-aligned poynting flux near the earth's plasma sheet boundary. *Geophysical Research Letters*, 44(14):7106–7113, 2017.

[125] WJ Sun, SY Fu, GK Parks, J Liu, ZH Yao, QQ Shi, Q-G Zong, SY Huang, ZY Pu, and T Xiao. Field-aligned currents associated with dipolarization fronts. *Geophysical Research Letters*, 40(17):4503–4508, 2013.

[126] Daniel W Swift. Use of a hybrid code for global-scale plasma simulation. *Journal of Computational Physics*, 126(1):109–121, 1996.

[127] Daniel W Swift and Yu Lin. Substorm onset viewed by a two-dimensional, global-scale hybrid code. *Journal of Atmospheric and Solar-Terrestrial Physics*, 63(7):683–704, 2001.

[128] K Takahashi, S Kokubun, T Sakurai, RW McEntire, TA Potemra, and RE Lopez. Ampte/cce observations of substorm-associated standing alfvén waves in the midnight sector. *Geophysical research letters*, 15(11):1287–1290, 1988.

[129] B Tan, Y Lin, JD Perez, and XY Wang. Global-scale hybrid simulation of dayside magnetic reconnection under southward imf: Structure and evolution of reconnection. *Journal of Geophysical Research: Space Physics*, 116(A2), 2011.

[130] M Temerin and I Roth. Ion heating by waves with frequencies below the ion gyrofrequency. *Geophysical research letters*, 13(11):1109–1112, 1986.

[131] A Vaivads, Y Khotyaintsev, M André, A Retino, SC Buchert, BN Rogers, P Décréau, G Paschmann, and TD Phan. Structure of the magnetic reconnection diffusion region from four-spacecraft observations. *Physical review letters*, 93(10):105001, 2004.

[132] CL Vásconez, F Pucci, F Valentini, S Servidio, WH Matthaeus, and F Malara. Kinetic alfvén wave generation by large-scale phase mixing. *The Astrophysical Journal*, 815(1):7, 2015.

[133] Vytenis M Vasyliunas. Theoretical models of magnetic field line merging. *Reviews of Geophysics*, 13(1):303–336, 1975.

[134] S Von Alfthan, D Pokhotelov, Y Kempf, S Hoilijoki, I Honkonen, A Sandroos, and M Palmroth. Vlasiator: First global hybrid-vlasov simulations of earth's foreshock and magnetosheath. *Journal of Atmospheric and Solar-Terrestrial Physics*, 120:24–35, 2014.

[135] Claës Walén. On the theory of sunspots. *Arkiv for Astronomi*, 30:1–87, 1944.

[136] A David M Walker. *Magnetohydrodynamic waves in geospace: The theory of ULF waves and their interaction with energetic particles in the solar-terrestrial environment*. CRC Press, 2019.

[137] Raymond J Walker, Tatsuki Ogino, Joachim Raeder, and Maha Ashour-Abdalla. A global magnetohydrodynamic simulation of the magnetosphere when the interplanetary magnetic field is southward: The onset of magnetotail reconnection. *Journal of Geophysical Research: Space Physics*, 98(A10):17235–17249, 1993.

[138] XY Wang, ZX Liu, ZY Li, and XB Zhang. Kinetic alfven waves driven by velocity shear. *Physics of Plasmas*, 5(4):836–840, 1998.

[139] Simon Wing, Matina Gkioulidou, Jay R Johnson, Patrick T Newell, and Chih-Ping Wang. Auroral particle precipitation characterized by the substorm cycle. *Journal of Geophysical Research: Space Physics*, 118(3):1022–1039, 2013.

[140] JR Wygant, A Keiling, CA Cattell, l M Johnson, RL Lysak, M Temerin, FS Mozer, CA Kletzing, JD Scudder, W Peterson, et al. Polar spacecraft based comparisons of intense electric fields and poynting flux near and within the plasma sheet-tail lobe boundary to uvi images: An energy source for the aurora. *Journal of Geophysical Research: Space Physics*, 105(A8):18675–18692, 2000.

[141] JR Wygant, A Keiling, CA Cattell, RL Lysak, M Temerin, FS Mozer, CA Kletzing, JD Scudder, V Streltsov, W Lotko, et al. Evidence for kinetic alfvén waves and parallel electron energization at 4–6 re altitudes in the plasma sheet boundary layer. *Journal of Geophysical Research: Space Physics*, 107(A8):SMP–24, 2002.

[142] Zhonghua Yao, WJ Sun, SY Fu, ZY Pu, Jiang Liu, V Angelopoulos, X-J Zhang, XN Chu, QQ Shi, RL Guo, et al. Current structures associated with dipolarization fronts. *Journal of Geophysical Research: Space Physics*, 118(11):6980–6985, 2013.

[143] X-J Zhang, V Angelopoulos, A Runov, X-Z Zhou, J Bonnell, JP McFadden, D Larson, and U Auster. Current carriers near dipolarization fronts in the magnetotail: A themis event study. *Journal of Geophysical Research: Space Physics*, 116(A5), 2011.

[144] Meng Zhou, Maha Ashour-Abdalla, Xiaohua Deng, David Schriver, Mostafa El-Alaoui, and Ye Pang. Themis observation of multiple dipolarization fronts and associated wave characteristics in the near-earth magnetotail. *Geophysical Research Letters*, 36(20), 2009.

[145] X-Z Zhou, V Angelopoulos, VA Sergeev, and A Runov. Accelerated ions ahead of earthward propagating dipolarization fronts. *Journal of Geophysical Research: Space Physics*, 115(A5), 2010.

[146] Ellen G Zweibel and Masaaki Yamada. Magnetic reconnection in astrophysical and laboratory plasmas. *Annual review of astronomy and astrophysics*, 47:291–332, 2009.

[147] Ellen G Zweibel and Masaaki Yamada. Perspectives on magnetic reconnection. *Proceedings of the Royal Society A: Mathematical, Physical and Engineering Sciences*, 472(2196):20160479, 2016.

Appendices

Appendix A

A.1 Derivation of Walén Relation for KAWs

The set of the basic equations based on the kinetic-fluid theory [24] can be written as

$$\rho\frac{d\mathbf{V}}{dt} = \mathbf{J}\times\mathbf{B} - \nabla\cdot\mathcal{P} - \nabla\cdot\mathbf{\Pi}, \tag{A.1}$$

$$\frac{d\rho}{dt} = -\rho\nabla\cdot\mathbf{V}, \tag{A.2}$$

$$\frac{\partial\mathbf{B}}{\partial t} = -\nabla\times\mathbf{E}, \tag{A.3}$$

$$\nabla\times\mathbf{B} = \mathbf{J}, \tag{A.4}$$

where ρ and $\mathbf{V}$ are mass density and bulk velocity of one fluid, respectively, and $\mathcal{P}$ and $\mathbf{\Pi}$ are diagonal pressure tensor element and off-diagonal pressure tensor element, respectively. The charge quasi-neutrality condition, $n_e e = \sum_i n_i q_i$, is assumed. Substituting the $\mathbf{J}\times\mathbf{B}$ term in equation (A.1) using the perpendicular generalized Ohm's law [71] and ignoring electron inertial terms, we have

$$\mathbf{E}_\perp + \mathbf{V}\times\mathbf{B} = \frac{1}{n_e e}\nabla_\perp\cdot(\mathcal{P}+\mathbf{\Pi}) + \rho\frac{d\mathbf{V}_\perp}{dt}. \tag{A.5}$$

The gyroviscosity contribution is given by [24]

$$\nabla_\perp\cdot\mathbf{\Pi} = \nabla_\perp\delta P_c + \hat{\mathbf{b}}\times\nabla_\perp\delta P_s, \tag{A.6}$$

where $\hat{\mathbf{b}}$ is the unit vector along the background magnetic field, $\delta P_c = \int d^3v\frac{mv_\perp^2}{2}\cos 2\theta\delta f$ and $\delta P_s = \int d^3v\frac{mv_\perp^2}{2}\sin 2\theta\delta f$ with θ being the particle gyrophase angle between $\hat{\mathbf{b}}$ and $\hat{\mathbf{k}}_\perp$(the unit vector along the perpendicular wave vector directions). Fourier transforming fields and ignoring the background gradients and parallel magnetic field fluctuations (this approximation is valid for the whole derivation), the following equation can be obtained from equation (A.5)

$$\mathbf{V}_\perp\times\mathbf{B} + (\Gamma_0 - \Gamma_1)\,\mathbf{E}_\perp = 0, \tag{A.7}$$

where $\Gamma_n = I_n(b)e^{-b}$, with $b = k_\perp^2 \rho_i^2$ and I_n being the modified Bessel function of first kind of order n. The gyroviscosity term is conveniently considered together with the $\rho \frac{d\mathbf{V}_\perp}{dt}$ term because

$$\hat{\mathbf{b}} \times \nabla_\perp \delta P_s = \left(\frac{1-\Gamma_0}{b} - (\Gamma_0 - \Gamma_1) \right) \rho \frac{\partial}{\partial t} \frac{\mathbf{E} \times \mathbf{B}}{B^2}. \tag{A.8}$$

Let us define a new velocity variable

$$\tilde{\mathbf{V}} \equiv \mathbf{V} + \left(\frac{1-\Gamma_0}{b} - (\Gamma_0 - \Gamma_1) \right) \frac{\mathbf{E} \times \mathbf{B}}{B^2}. \tag{A.9}$$

The Ohm's law is then reduced to

$$\tilde{\mathbf{V}} = \frac{1-\Gamma_0}{b} \frac{\mathbf{E} \times \mathbf{B}}{B^2}, \tag{A.10}$$

where

$$\tilde{\mathbf{V}} = \frac{1-\Gamma_0}{b} \frac{1}{\Gamma_0 - \Gamma_1} \mathbf{V}. \tag{A.11}$$

In transforming these equations to real space from their Fourier representation, we employ the Padé approximation, which leads to

$$\frac{1-\Gamma_0}{b} \sim \frac{1}{1+b}, \tag{A.12}$$

and

$$\left(\frac{1-\Gamma_0}{b} \right) \frac{1}{\Gamma_0 - \Gamma_1} \sim 1 + 1.25b. \tag{A.13}$$

The Padé approximation implies upon inversed Fourier transform that

$$\left(1 - \rho_i^2 \nabla_\perp^2\right) \tilde{\mathbf{V}}_\perp \approx \frac{\mathbf{E} \times \mathbf{B}}{B}, \tag{A.14}$$

and

$$\left(1 - 1.25\rho_i^2 \nabla_\perp^2\right) \mathbf{V}_\perp \approx \tilde{\mathbf{V}}_\perp. \tag{A.15}$$

Using equations (A.14) and (A.15), the momentum equation and the Faraday's law can be written as

$$\rho \frac{\partial \tilde{\mathbf{V}}}{\partial t} + \mathbf{V} \cdot \nabla \mathbf{V} = \mathbf{B} \cdot \nabla \mathbf{B} - \nabla \left(P + B^2/2 \right) \tag{A.16}$$

and

$$\frac{\partial \mathbf{B}}{\partial t} = \left(1 - \rho_i^2 \nabla_\perp^2\right) (\mathbf{B} \cdot \nabla \tilde{\mathbf{V}} - \mathbf{B} \nabla \cdot \tilde{\mathbf{V}} - \tilde{\mathbf{V}} \cdot \nabla \mathbf{B}) - \nabla \times \mathbf{E}_\parallel, \tag{A.17}$$

respectively. Based on the parallel Ohm's law,

$$\frac{m_e}{n_e e^2} \partial \mathbf{J}_\parallel / \partial t = -\frac{m_e}{n_e e^2} \mathbf{b} \cdot \nabla \times (\nabla \times \mathbf{E}) = \mathbf{E}_\parallel + \frac{1}{n_e e} \nabla P_e, \tag{A.18}$$

the parallel electric field can be written as

$$\left(1 - \lambda_e^2 \nabla_\perp^2\right) \mathbf{E}_\parallel = -\lambda_e^2 \nabla_\parallel \nabla_\perp \cdot \mathbf{E}_\perp - \frac{T_e}{e\rho} \nabla_\parallel \rho, \tag{A.19}$$

where λ_e is the electron skin depth. Using Ohm's law and keeping terms to order ω/Ω_i, the continuity equation can be expressed as

$$\frac{1}{\rho}\frac{d\rho}{dt} = \frac{e}{m_i\Omega_i^2}\mathbf{B}\times\nabla_\perp\cdot\partial\tilde{\mathbf{V}}/\partial t + \frac{\mathbf{B}\cdot\partial\mathbf{B}/\partial t}{B^2}. \tag{A.20}$$

Neglect compressional effects and background gradients in equation (A.20). Then equation (A.19) can be simplified as

$$\left(1-\lambda_e^2\nabla_\perp^2\right)E_\parallel = -\left(\rho_s^2-\lambda_e^2\left(1-\rho_i^2\nabla_\perp^2\right)\right)\nabla_\parallel\left(\mathbf{B}\times\nabla_\perp\cdot\tilde{\mathbf{V}}\right), \tag{A.21}$$

where $\rho_s^2 \equiv (T_e/T_i)\,\rho_i^2$ is the ion acoustic gyroradius.

Finally, the perpendicular terms of equations (A.16) and (A.17) in the homogeneous limit in the Fourier representation are written as

$$\omega\rho\delta\tilde{\mathbf{V}}_\perp = -k_\parallel B_0\delta\mathbf{B}_\perp + \mathbf{k}_\perp\left(\delta P + B_0\delta B_\parallel\right), \tag{A.22}$$

and

$$\omega\delta\mathbf{B}_\perp = -k_\parallel B_0\left(1+k_\perp^2\rho_i^2\right)\delta\tilde{\mathbf{V}}_\perp - \mathbf{b}\times\mathbf{k}_\perp E_\parallel. \tag{A.23}$$

Equation (A.21) in the Fourier representation is written as

$$\left(1+k_\perp^2\lambda_e^2\right)E_\parallel = k_\parallel B_0\left(\rho_s^2-\lambda_e^2\left(1+k_\perp^2\rho_i^2\right)\right)\mathbf{b}\times\mathbf{k}_\perp\cdot\delta\tilde{\mathbf{V}}_\perp. \tag{A.24}$$

Combining equations (A.23) and (A.24), we obtain the relation between the perturbed magnetic field and velocity as

$$\omega\delta\mathbf{B}_\perp = -k_\parallel B_0\frac{1+(1+T_e/T_i)\,k_\perp^2\rho_i^2}{1+k_\perp^2\lambda_e^2}\delta\tilde{\mathbf{V}}_\perp. \tag{A.25}$$

The projection in the $\mathbf{b}\times\mathbf{k}_\perp$ direction of equations (A.22) and (A.24) gives the KAW/SAW dispersion relation:

$$\omega^2 = k_\parallel^2 V_A^2\frac{1+(1+T_e/T_i)\,k_\perp^2\rho_i^2}{1+k_\perp^2\lambda_e^2}. \tag{A.26}$$

Combing equations (A.11), (A.13), (A.25) and (A.26) and considering $\delta\mathbf{V}\approx\delta\mathbf{V}_i$, the Walén relation for KAWs is given by

$$\delta\mathbf{V}_i \approx \pm\delta\mathbf{V}_A\left(\frac{1+k_\perp^2\lambda_e^2}{1+\left(1+\frac{T_e}{T_i}\right)k_\perp^2\rho_i^2}\right)^{1/2}\left(\frac{1}{1+1.25k_\perp^2\rho_i^2}\right), \tag{A.27}$$

where the coefficient $\frac{1}{1+1.25k_\perp^2\rho_i^2}$ comes from the gyroviscosity in the pressure tensor.